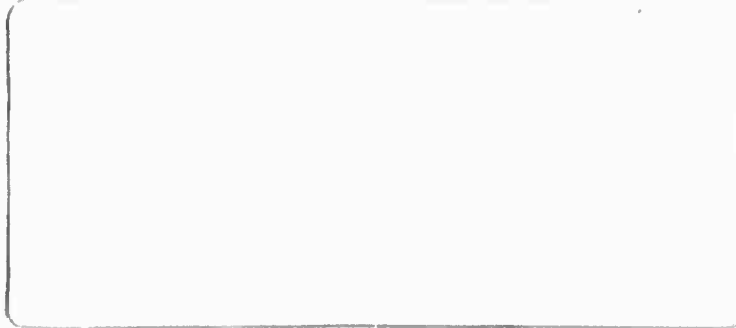


AD716541



Reproduced by  
NATIONAL TECHNICAL  
INFORMATION SERVICE  
Springfield, Va. 22151

 **TELEDYNE  
ISOTOPIES**

1. This document has been approved for public release and sale; its distribution is unlimited.



# DISCLAIMER NOTICE

THIS DOCUMENT IS THE BEST  
QUALITY AVAILABLE.

COPY FURNISHED CONTAINED  
A SIGNIFICANT NUMBER OF  
PAGES WHICH DO NOT  
REPRODUCE LEGIBLY.



SUMMARY REPORT  
ATMOSPHERIC PROPAGATION STUDIES  
UP TO 30 SEPTEMBER 1969

Hernan A. Montes  
Chester E. Grosch  
Melvin J. Minich  
Eric S. Posmentier

Prepared for  
Advanced Research Projects Agency  
Department of Defense

ARPA Order No. 1316  
Program Code N9F 20

Monitored by  
Air Force Office of Scientific Research

Contract No. F 44620-69-C-0038

July 1970

TELEDYNE ISOTOPES  
50 Van Buren Avenue  
Westwood, New Jersey 07675

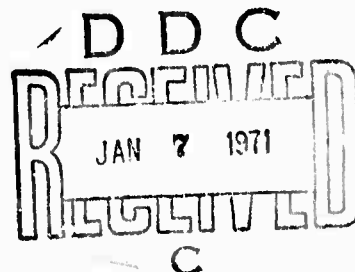




## TABLE OF CONTENTS

### Abstract

1.	INTRODUCTION . . . . .	1-1
2.	EXPERIMENTAL ATMOSPHERIC PHYSICS . . . . .	2-1
2.1	Teledyne Isotopes' Array . . . . .	2-1
2.1.1	Array Geography . . . . .	2-1
2.1.2	Array Logistics & Instrumentation . . . . .	2-4
2.1.3	Array Response Calculations . . . . .	2-10
2.2	Event-Related Phenomena . . . . .	2-26
2.2.1	Atmospheric Nuclear Tests . . . . .	2-26
2.2.2	Saturn-Apollo IX Associated Signals . . . . .	2-38
2.2.3	Correlation of Atmospheric Pressure Waves with Ionospheric Phase-Path Sounder Signals . . . . .	2-41
2.3	Background Field . . . . .	2-42
2.3.1	Ionospheric Background Motions . . . . .	2-42
2.3.2	Microbarograph Signal and Noise Fields . . . . .	2-84
3.	THEORETICAL ATMOSPHERIC PHYSICS . . . . .	3-1
3.1	Wave Propagation . . . . .	3-1
4.	THEORETICAL SIGNAL PROCESSING . . . . .	4-1
4.1	Estimation and Detection of an Unknown Dispersive Signal Using a Two-Dimensional Array . . . . .	4-1
4.1.1	Introduction . . . . .	4-1
4.1.2	Plane Wave Signal and Noise . . . . .	4-3
4.1.3	Signal Processing . . . . .	4-7
4.1.4	Estimation of Direction and Dispersion . . . . .	4-16
4.1.5	Signal Detection . . . . .	4-19
4.2	Cophase: An Ad-Hoc Array Processor . . . . .	4-20
4.2.1	Introduction . . . . .	4-20
4.2.2	Distribution in the Null Hypothesis . . . . .	4-21
4.2.3	Distribution in the Alternative Hypothesis . . . . .	4-23
4.2.4	Evaluation of Cophase Techniques . . . . .	4-25
4.2.5	Conclusions . . . . .	4-35
5.	SUMMARY AND CONCLUSIONS	
	REFERENCES	
	DISTRIBUTION LIST	



ABSTRACT

A summary is given of significant results obtained during the research effort corresponding to the period 1 September 1968 - 30 September 1969. Particular emphasis was given to the construction of a phase-path doppler sounder array. Signals detected by the microbarograph array on the occasion of the Chinese nuclear test of 29 September 1969 are compared with signals from previous tests. There appears to be a seasonal effect on the propagation and/or bandwidth of these signals. Preliminary work on ionospheric motion background using phase-path sounder data indicates that the background activity can be broadly separated into two period ranges: periods longer and shorter than 5 minutes. The shorter periods appear to have a hydromagnetic origin while the longer periods are probably due to internal gravity wave activity. A study of the spatial coherency of the signal and noise field for the array of microbarographs indicated that acoustic signals have coherencies well above the background noise at separations greater than 3 or 4 km. The signal coherency remains high up to separations of 50 km and transverse signal coherencies are larger than parallel signal coherencies as would be expected from long-crested waves. A theoretical investigation of the interaction between instability waves and internal gravity waves in the atmosphere showed that internal gravity waves are trapped within a layer where the shear flow velocity is greater than the speed of sound and that the phase velocity of the internal gravity waves is approximately equal to the maximum velocity of the shear flow. As part of the theoretical aspect of signal processing two array processing techniques have been developed.



## 1. INTRODUCTION

In the course of this year's research effort, the authors have had occasion to make a critical review of the course of the project, its history, previous results, and what they felt to be its future direction. This appraisal has led them in some cases to redirect or shift the orientation and emphasis of the research in the light of previous and new results.

It is pertinent to review the prior history of the infrasonics program since most of its initial principals have departed the scene. The project started in late 1965 at the Hudson Laboratories of Columbia University, being funded by ARPA and administered by the Office of Naval Research. It is our understanding that the underlying purpose of the project was to look for the existence of long period (greater than 10 minutes) gravity waves in the atmosphere and to study their possible usefulness in the detection and diagnosis of atmospheric nuclear detonations. The initial phases were devoted to the design and construction of suitable sensors which were installed in remote locations about the middle of 1966. A paper-tape digital data acquisition system was installed initially and computer programs for data processing were written. The Chinese atmospheric test of June 1967 gave some encouragement to the validity of the concept by a definitive recording. The data acquisition system was later improved so that the output could be written on magnetic tape in a form compatible with the subsequent data processing. Prior to the French series of atmospheric tests in the summer of 1968, the microbarograph array had grown to some 12 instruments and had an aperture of about 250 kilometers. Later a single phase-path doppler ionosonde and a three-component magnetometer



## Teledyne Isotopes

array were installed. The magnitude of the arrays brought with it concomitant financial outlays in maintenance, personnel, equipment and telephone rental. Also at this time the project used an IBM-1800 computer, having had an 1130 computer with limited capacity.

In April 1968 Columbia University announced the impending closure of Hudson Laboratories. At that time arrangements were made to transfer the project to Teledyne Isotopes as of September 1968. After a period of shutdown during the transfer, extended because of the prolonged AT&T strike of 1968, the system again became operational at its new location in Westwood. An IBM 360/30 modified by software to operate in the 360/44 mode for scientific work was installed at Westwood to replace the IBM-1800 computer. Both the hardware and software have proved entirely satisfactory for all requirements of the project, and no modification in either is being sought. The Hudson Laboratories computer programs were translated to the IBM-360 language and some new programs have been added to the project's computer library.

During the period from mid-1966 to the present, theoretical studies and data analyses have been carried on concurrently with the data gathering. The results of these analyses and supporting data have been presented in various technical and quarterly progress reports and may be summarized as follows.

Definite observations of long period gravity waves have been made in conjunction with atmospheric nuclear detonations.

The pressure signals themselves are rather weak. The signal-to-noise ratio at any particular station is generally less than one. It follows, therefore, that the signals can only be extracted from the noise by judicious filtering. The data from any station where the noise power is considerably in excess of the



## Teledyne Isotopes

mean noise power, must be eliminated. The data must also be filtered with a fairly narrow band-pass filter. Further, the array must be beam steered, i.e. by velocity and directional filtering, and a knowledge of  $T_0$  is essential to identification.

Theoretical studies have shown that a large part of the energy of the long period gravity waves, generated by nuclear explosions, will be trapped near the "top" of the atmosphere. Particle motion should therefore be large at ionospheric heights and the corresponding pressure fluctuations should be small at ground level. Such behavior appears to be verified by the observation of a signal using a phase-path doppler sounder which we believe to be a gravity wave generated by the French nuclear detonation of 24 August 1968. The signal-to-noise ratio for the observed event-related signal is about 2. Since only one ionosonde was in operation, no information could be obtained concerning the phase velocity and direction of travel of this wave.

On the basis of such results we were forced to conclude that microbarographs do not appear to be the best sensors with which to detect long period gravity waves for the program's expressed purpose of detection and diagnosis. Furthermore, a comparison of the theoretical response of the Teledyne-Isotopes array with that of a number of other arrays such as 10, 15, and 21-element isometric arrays and the LAMA array, showed that not much improvement could be expected by adding new instruments or changing the geometry of the present array. It would appear rather that the phase-path doppler ionosonde is perhaps a more effective sensor. On this premise we considered concentrating further effort on the phase-path sounder.



## Teledyne Isotopes

The phase-path doppler sounder array is only in its initial experimental phase, and much remains to be explored in relation to optimum transmission frequencies, noise and signal levels, and coherence over the array. Placing greater emphasis on the doppler array has introduced a new class of ionospheric phenomena not relevant to ground level pressure measurements. These include, for instance, noise associated with solar flares, geomagnetic storms, hydro-magnetic modulation of the ionospheric plasma, interaction between neutral and ionized components of the upper atmosphere.

On the occasion of the Chinese nuclear test of 29 September 1969, signals coming from the direction of the test site were recorded in the micro-barograph array. The analyses of these recordings were carried out in a similar way as the signals from previous tests were analyzed at Hudson Laboratories, so a direct comparison between previous results and results from this test can be made.

As part of the phase-path variation studies, preliminary work has been done on ionospheric background phenomena. This work has been directed mainly to the determination of the type of driving mechanism characterizing various period ranges.

Experimental results at Hudson Laboratories indicated that internal gravity waves are associated with the jet stream. It has been suggested that these internal waves are generated by a non-linear interaction of instability waves. It was therefore desirable to carry out a theoretical study of the interaction of instability waves and internal gravity waves. A model which neglects compressibility was used to find solutions for this problem.



## Teledyne Isotopes

Finally the important task concerned with the recognition of signals from the noise has been pursued by Dr. M. Hinich of the Carnegie Mellon Institute and Dr. E. Posmentier of New York University, resulting in two array processing techniques.



Teledyne Isotopes

## 2. EXPERIMENTAL ATMOSPHERIC PHYSICS

### 2.1 Teledyne Isotopes Array

#### 2.1.1 Array Geography

Data for atmospheric-wave propagation studies is collected by an array of sensors, consisting of phase-path doppler sounders, microbarographs and magnetometers, located at the various stations shown in Figure 2.1 . The geographic coordinates of these stations are listed in Table 2.1.

#### Phase-path doppler sounder array

A continuous wave 4-element doppler sounder array has been in operation during the last months of the contract year. The transmitter is situated at Sterling Forest. It should be noted that this is the only location for which it has been possible thus far to obtain a transmission license from the F.C.C. The array is licensed to operate at frequencies of 2.4, 4.8, 6.0 MHz, although the 4.8 MHz is used for normal routine operation. Initially there was only a single receiver at Westwood, but now four receiving stations (Westwood, Catskill, Thornhurst and Lebanon) are in full operation. With the equipment now available, multiple-frequency measurements at a single station are workable as shown in a later section.

#### Microbarograph array

The microbarograph array at present in operation consists of ten long period microbarographs in a roughly rectangular configuration. The average spacing of the instruments is approximately 60 kilometers and the array aperture is about 240 kilometers. The data is transmitted in analog form over telephone lines and recorded digitally. The initial operation of



Teledyne Isotopes

TABLE 2.1

FIELD STATION COORDINATES

Station	Latitude N	Longitude W
Sterling Forest, N.Y.	41° 11' 50"	74° 14' 40"
Thornhurst, Pa.	41° 12' 30"	75° 36' 30"
Catskill, N.Y.	42° 10' 59"	73° 55' 56"
Lebanon, N.J.	39° 55' 05"	74° 31' 18"
Stony Brook, L.I.	40° 54' 30"	73° 07' 32"
Lamont (Palisades), N.Y.	41° 00' 19"	73° 54' 28"
Naurausaun, N.Y.	41° 03' 26"	73° 59' 35"
Pawling, N.Y.	41° 33' 45"	73° 36' 04"
Monticello, N.Y.	41° 39' 24"	74° 40' 55"
Hackettstown, N.J.	40° 51' 07.5"	74° 49' 44"
Wagner College, S.I.	40° 36' 55"	74° 05' 46"
Westwood, N.J.	40° 59' 00"	74° 02' 00"



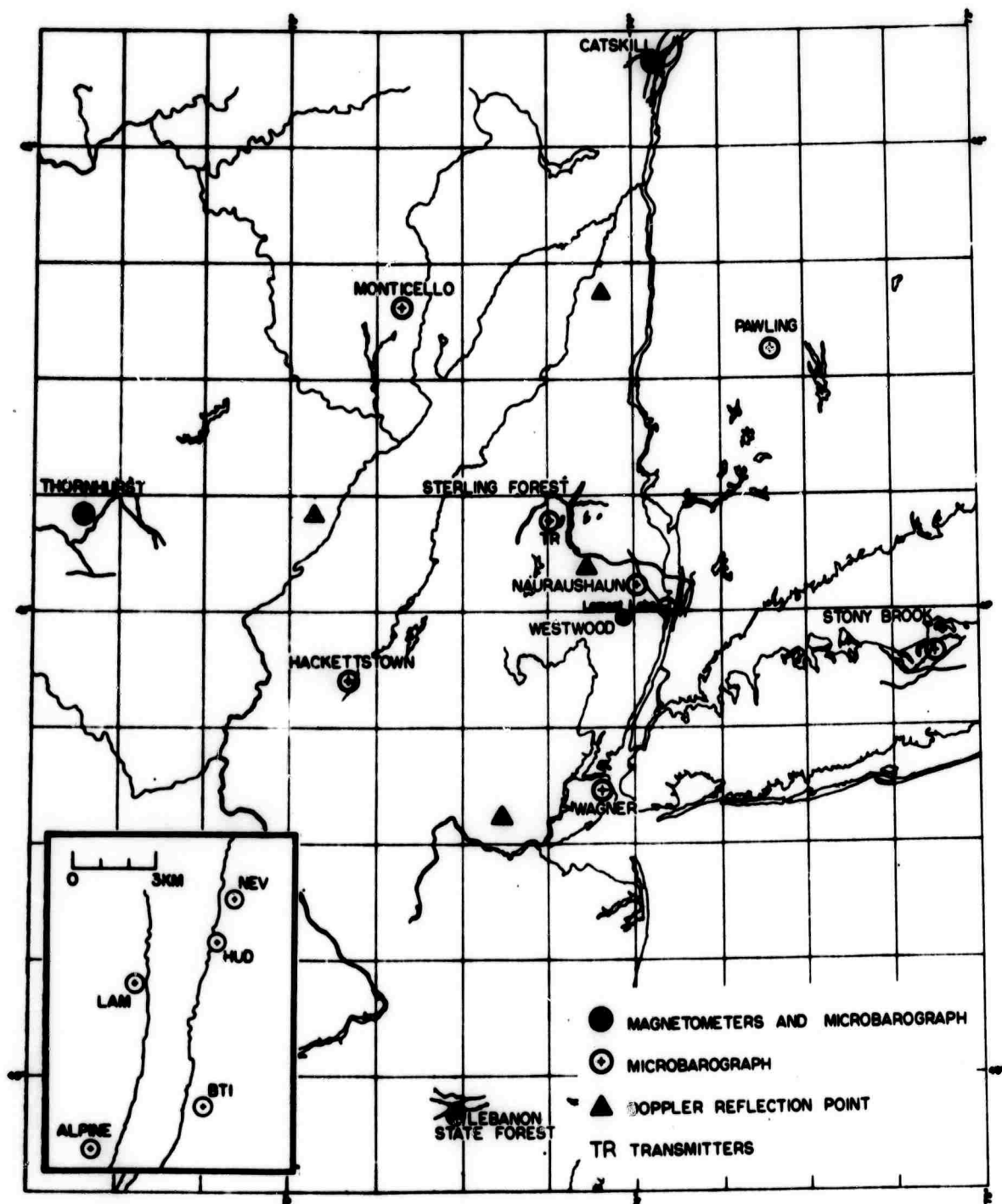


Fig. 2.1. Map showing the geographic distribution of the stations of the Teledyne Isotopes array.



## Teledyne Isotopes

the array, after its transfer to Westwood, was delayed for several months due to the lengthy AT&T strike, but data has been gathered continuously since January of this year. The instruments have given relatively trouble free performance, and apart from routine maintenance no repairs have been necessary. This aspect has been particularly gratifying since it encourages the belief that the microbarographs could continue operating with minimum maintenance in the coming year.

### Magnetometer Array

Three 3-component magnetometers, located at Catskill, Thornhurst and Lebanon, have also been in operation. The equipment has proved very reliable, requiring almost no maintenance. No development of any kind has been made on this equipment in the past year, and the data collected has proved very useful in the study of ionospheric background motions.

### 2.1.2 Array Logistics and Instrumentation

#### Logistics

The three major field stations are located in isolated areas, free of electrical interference, on state owned lands in New York, Pennsylvania and New Jersey. Trailers house the phase-path doppler sounders, microbarographs, magnetometers and the required digitizing electronics. These three field stations are linked by telephone line to the master control station at Westwood, N. J., where the incoming data is processed and stored on incremental digital magnetic tape. A fourth station identical to the ones mentioned above, except for the telephone link, is hard wired to the master station at Westwood, N. J.



## Teledyne Isotopes

In addition to the four major field stations, seven auxiliary sensor stations consisting of a single microbarograph and telemetering electronics are housed in municipal buildings such as fire houses, schools, etc. These seven auxiliary stations transmit their data in FM analog form by telephone lines to the nearest field station for digitization.

### Instrumentation

#### Phase-path doppler sounder

The high frequency continuous wave doppler array consists of a transmitter and four receiver stations. The doppler systems have been built after Davies (1962) with some modifications to meet our specifications.

The transmitter is simple and reliable. It is a Heathkit DX-60B transmitter modified for continuous operation and increased tuning range. Frequency stability is controlled by a precise crystal oscillator stable to 1 part in  $10^8$  per 24 hours. A single dipole antenna, an automatic keyer and a telephone line control link complete the transmitter system. Figure 2.2 shows the simplified block diagram of the doppler system.

A doppler receiving system consists of two receivers: a signal receiver and a reference receiver. The signal receiver is a Hammarlund SP600 which receives the transmitted signal after reflection from the ionosphere. The reference receiver is an in-house design. A brief description of the principle of operation of the receiving system follows.

The received ionospheric signal is converted to an intermediate frequency which becomes the I.F. signal ( $455 \text{ KHz} \pm \Delta f$ ) in the signal receiver. The reference signal, which comes from a precision crystal oscillator identical to the one used at the transmitter, is converted to an intermediate



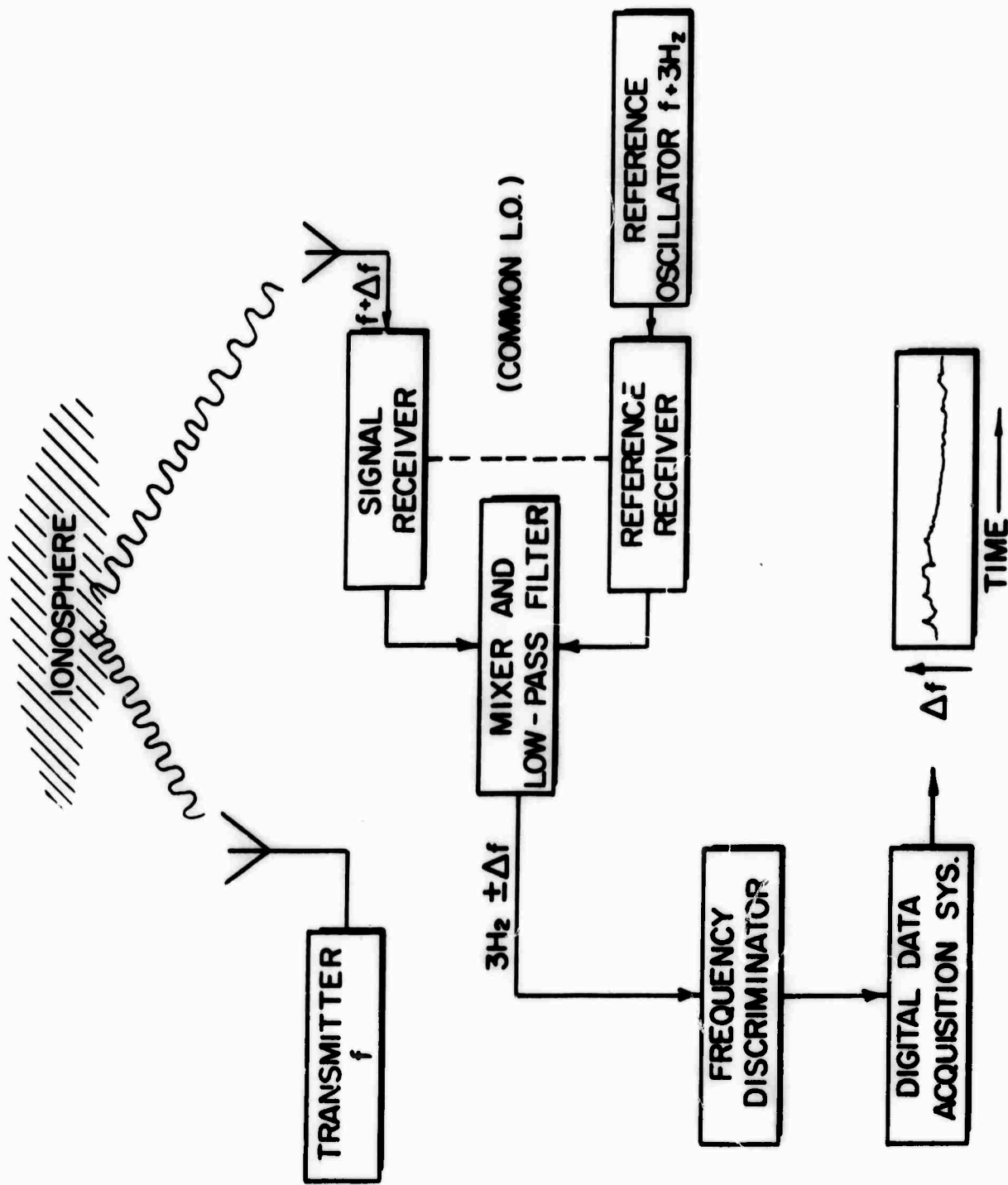


FIG. 2.2 Block diagram of the phase-path sounder system.



## Teledyne Isotopes

frequency (I.F. reference 455 KHz) in the BM7 mixer, which is slaved to the HFO (Local Oscillator) of the signal receiver. The difference between the I.F. signal and I.F. reference is equal to the doppler frequency. This difference is obtained in the BM9 mixer. In practice the reference frequency of the transmitter and of the reference receiver are offset by 2 or 3 Hz to allow for a decrease in the doppler frequency. The difference frequency, which is in the order of a few Hz, is amplified and converted into a DC voltage in the vidar 323 frequency to voltage converter. The output of the f/V converter is then passed through a low pass RC filter with a time constant  $T = RC$ , prior to digitization. That is, each digitized point represents the time average

$$E_o(t) = \frac{1}{\tau} \int_t^{t+\tau} E_i(t) dt . \quad (2.1)$$

The time constant  $\tau$  has been selected, according to the sampling rate, to minimize aliasing effects. During routine operations a sampling rate of 10 seconds is used.

The general specifications of the phase-path doppler system are given below.

### Signal Receiver - Hammarlund SP 600

Frequency band of interest	1.35 to 7.4 MHz
Selectivity	
I.F. crystal fitter	200 Hz
Sensitivity	1 $\mu$ V



## Teledyne Isotopes

### Reference Receiver - in house design

Input frequency range	0.05 MHz to 12 MHz
Output frequency range	1 KHz to 1 MHz
Maximum input level	1 V RMS

Stability is referenced to precision crystal oscillator 1 part in  $10^8$ /day

### Mixer - Spectran Balanced Ring Modulator S5-BM9

Input frequency range	5 KHz to 500 KHz
Output frequency range	0 to 495 KHz
Input levels	1 V RMS

### System Noise Level and Stability

The system noise level is taken to be 0.1 Hz. The results of a test to measure system noise are shown in Figure 2.3. To perform this test the input was shorted and the output was recorded for several days. It can be seen that over any 1-hour interval the signal deviates from its mean by an amount less than or equal to 0.02 Hz and that the signal drift over any 24-hour interval is approximately 0.08 Hz. The stability of the system is given by the stability of the precision oscillator which is 1 part in  $10^8$  per 24 hours plus the internal noise or about 1 part in  $10^7$ .

### Microbarographs

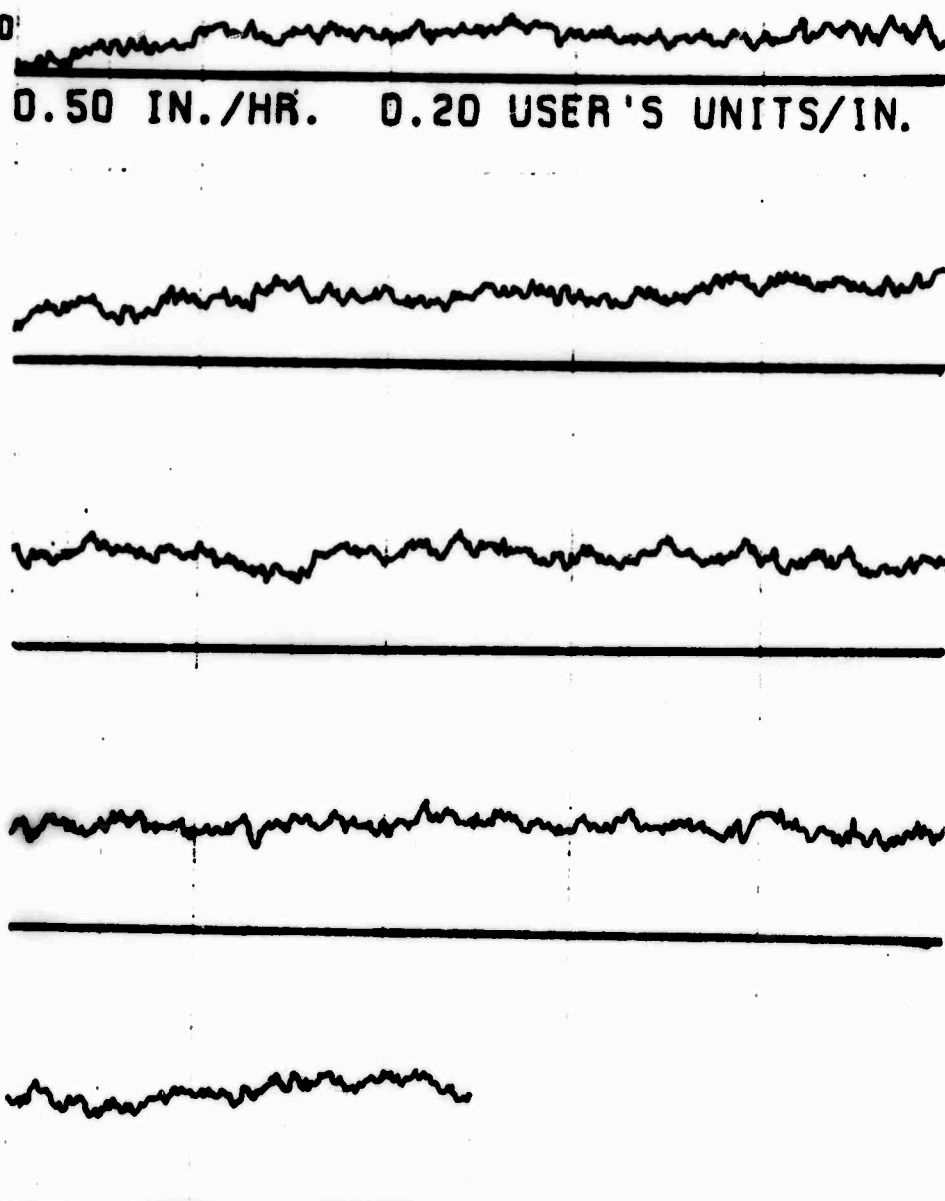
Initially the gain and bandwidth of each microbarograph were adjusted to meet selected values for a given input pressure change. Then two or more microbarographs were set to measure simultaneously an atmospheric signal at the same location for a 24-hour period and their outputs were recorded in different channels of the tape. Cross-spectrum analysis was applied to the digital records of the different pairs tested. In this way the coherence and phase response of each instrument were obtained.



DOPPLER

2 7 233050

0.50 IN./HR. 0.20 USER'S UNITS/IN.



The figure displays five horizontal traces of Doppler system noise test data. Each trace consists of a noisy signal line above a solid horizontal baseline. The traces are arranged vertically, with the top trace being the longest and the bottom trace being the shortest. The noise level appears relatively consistent across all traces.

FIG. 2.3 Doppler system noise test. Vertical scale 0.2 Hz/inch.  
Horizontal scale 2 hours/inch.



## Teledyne Isotopes

The microbarographs were developed and built at Hudson Laboratories of Columbia University, and they have been described by Clay and Kraft (1967). Brief specifications are listed below.

Frequency response	Flat from 1 cph to 180 cph
Sensitivity	3 $\mu$ bar
Range	2500 $\mu$ bar

### Magnetometers

Two kinds of magnetometers are used, rubidium vapor Varian model 4938 and Fluxgate Honeywell model YK 10BI.

#### Rubidium magnetometer

Frequency response	d.c. to 20 Hz
Sensitivity	$\pm$ 0.01 gammas

#### Fluxgate magnetometer

Frequency response	d.c. to 10 Hz
Sensitivity	$\pm$ 0.1 gammas

### 2.1.3 Array Response Calculations

A number of calculations were undertaken to compare the theoretical response of the Isotopes array with that of a number of other arrays; a 10-element isometric array, a 15-element isometric array, a 21-element isometric array and the LAMA (Large Aperture Microbarograph Array) array. The isometric arrays have been discussed by Haubrich (1968) and would appear to have a good theoretical response. The spatial arrangement of the sensors in the isometric arrays is given by Haubrich and the aperture was chosen to be 225 km so that it would be comparable with the Isotopes and LAMA arrays.



# ISOTOPES ARRAY

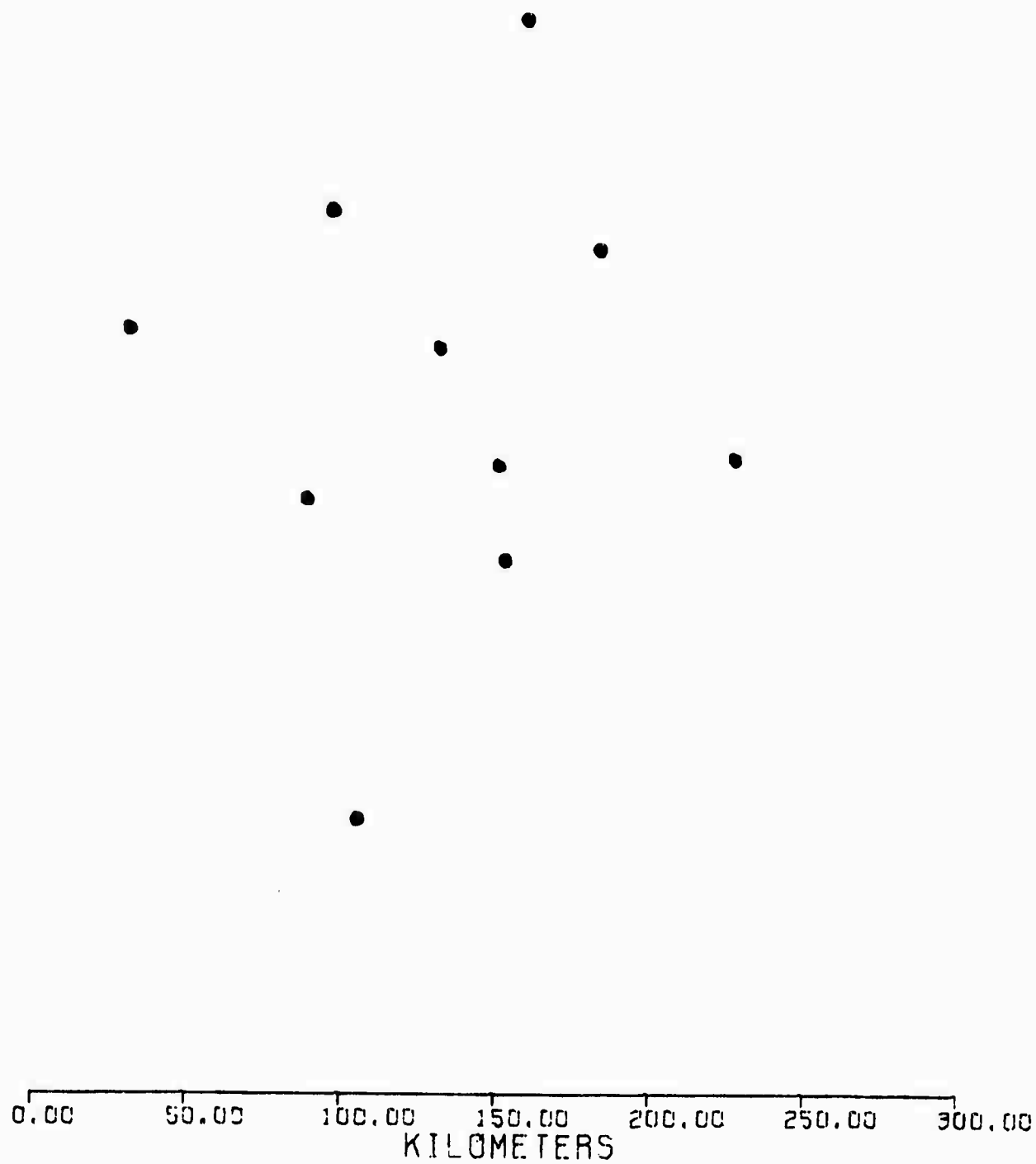


FIGURE 2.4



# LAMA ARRAY

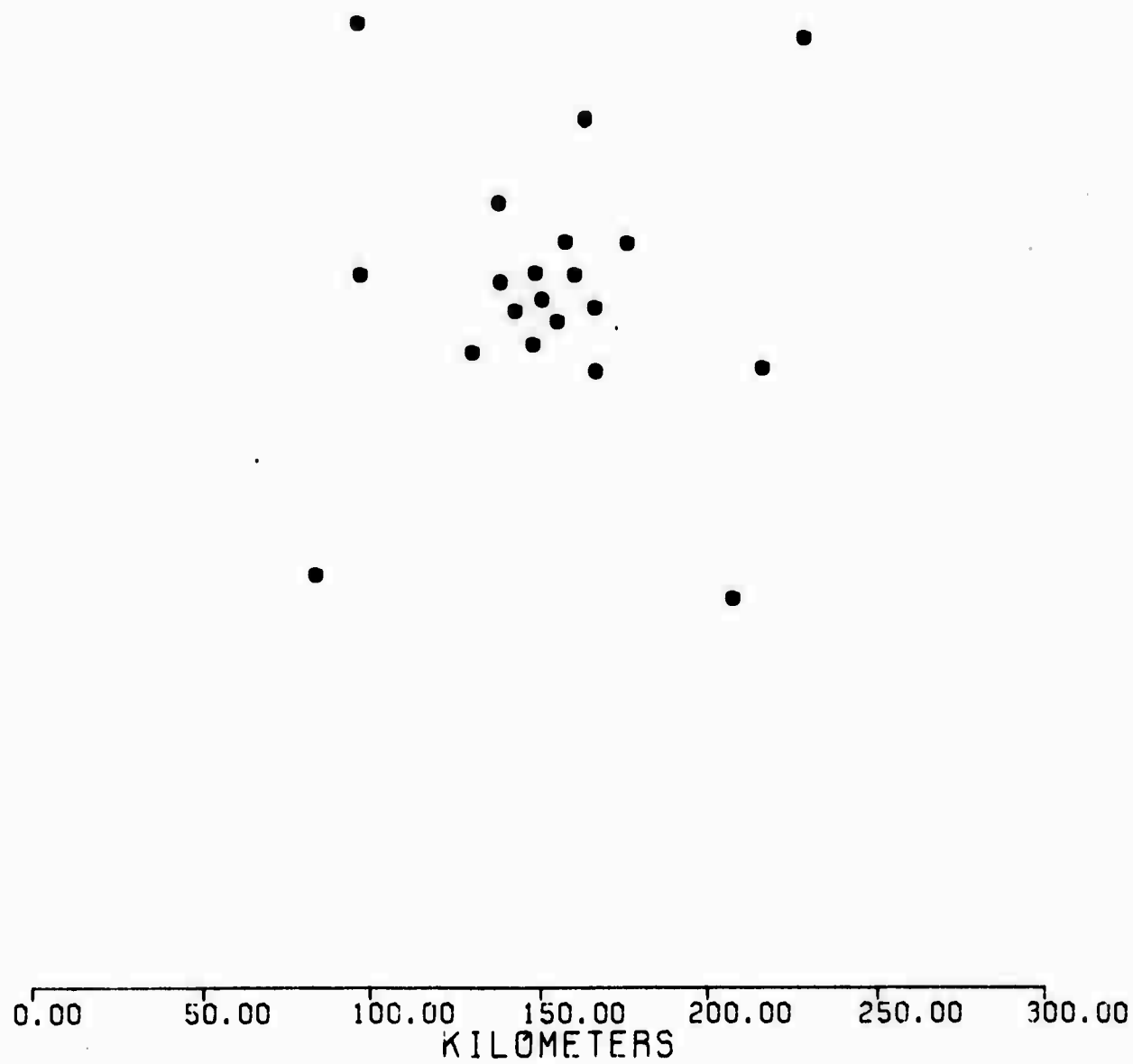


FIGURE 2,5



# 10 ELEMENT ISOMETRIC ARRAY

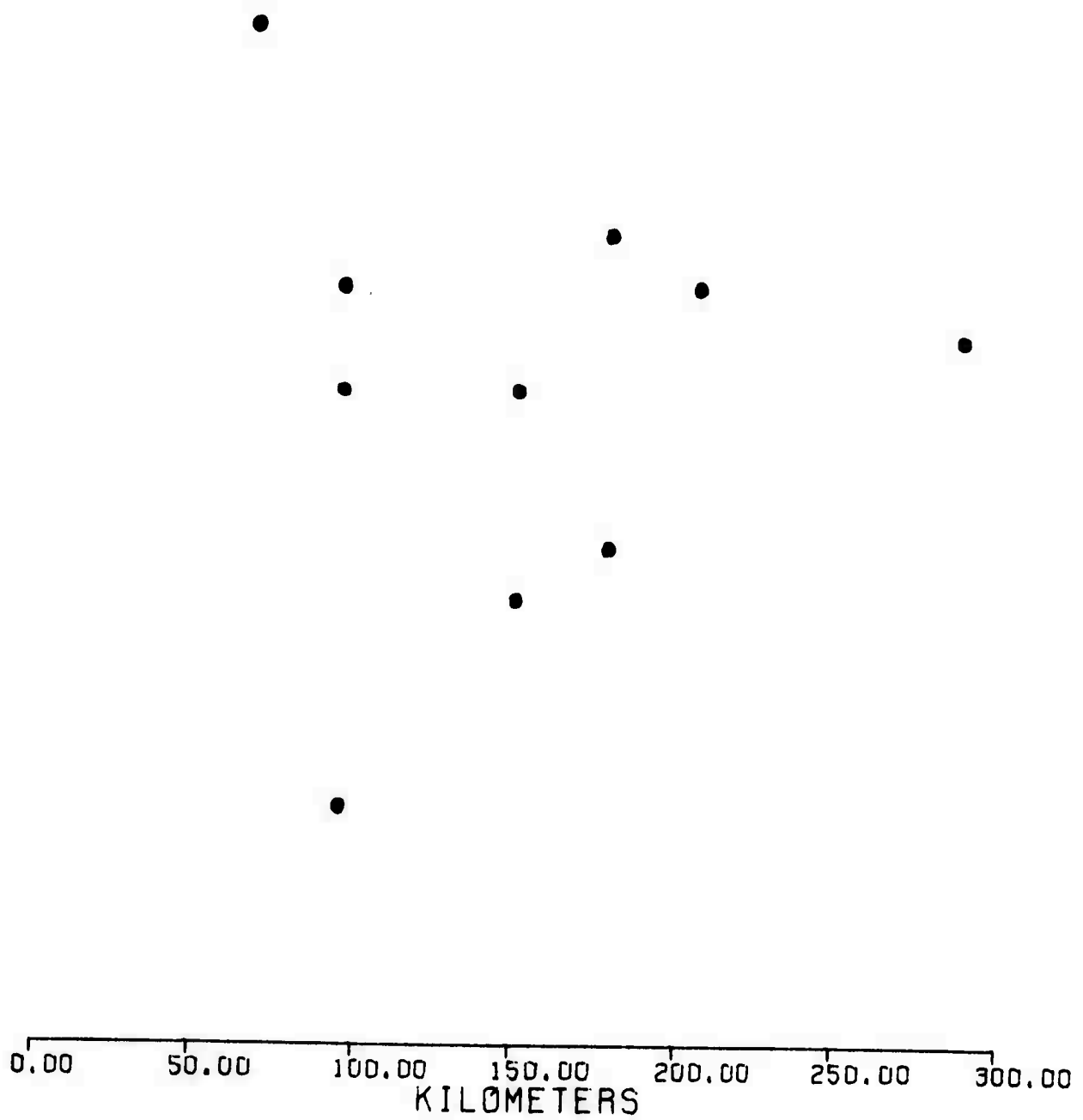


FIGURE 2.6



# 15 ELEMENT ISOMETRIC ARRAY

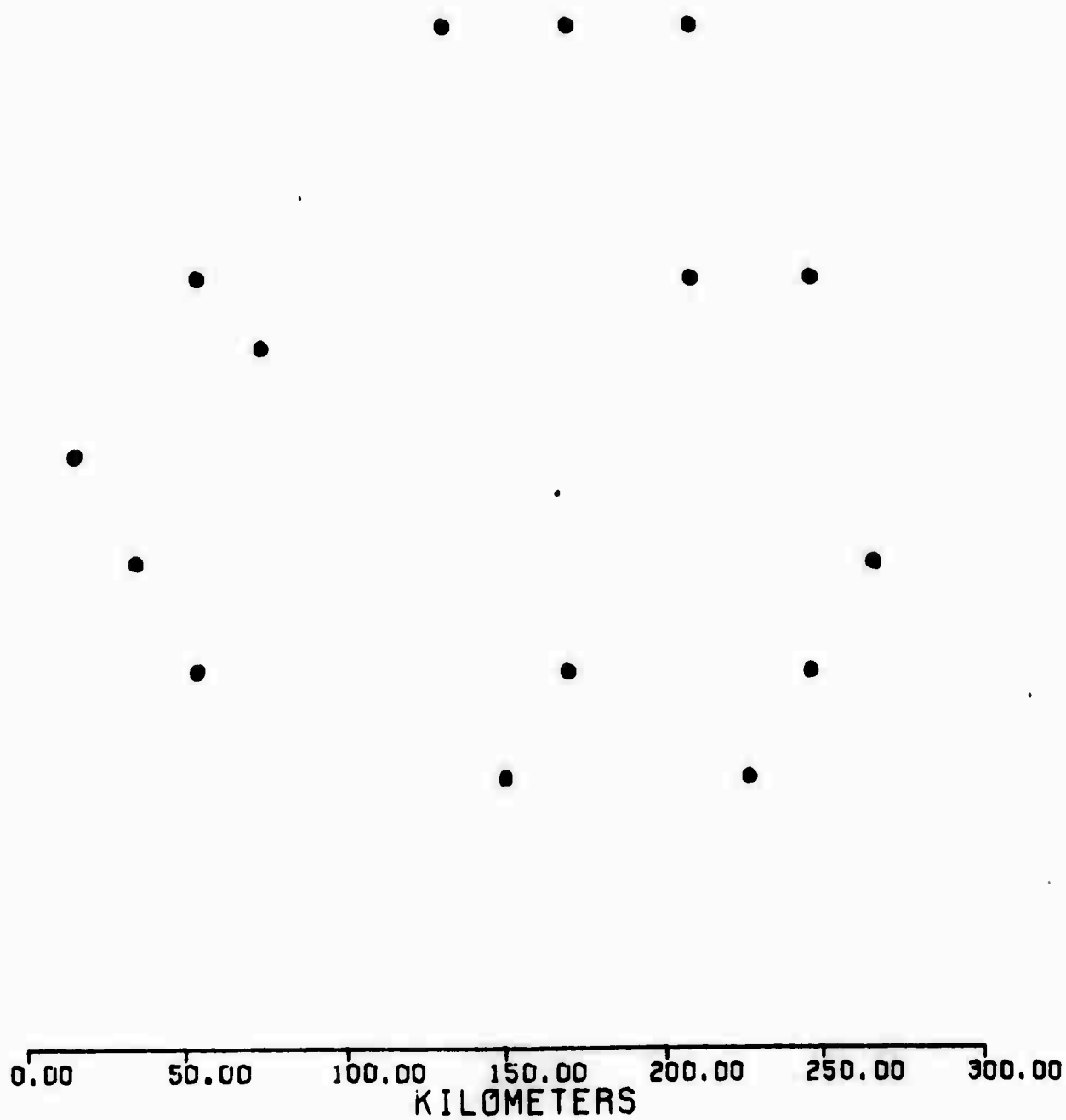


FIGURE 2.7



# 21 ELEMENT ISOMETRIC ARRAY

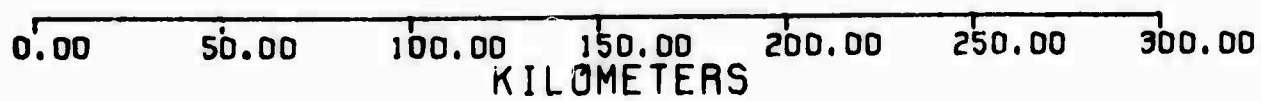


FIGURE 2.8



## Teledyne Isotopes

The response function is, of course, just the Fourier transform of the array, which is represented by a set of delta functions, one at each instrument position. Thus if  $\vec{r}_n$ ,  $n = 1, 2, \dots, N$  are the positions of the instruments, then,

$$K(k) = \iint \sum_{n=1}^N \sum_{m=1}^N \delta(\vec{r} - \vec{r}_n) \delta(\vec{r}' - \vec{r}_m) e^{-i\vec{k} \cdot \vec{r}} e^{-i\vec{k} \cdot \vec{r}'} d\vec{r} d\vec{r}' \quad (2.2)$$

$$K(\vec{k}) = \sum_{n=1}^N \sum_{m=1}^N e^{i\vec{k} \cdot (\vec{r}_n - \vec{r}_m)} \quad (2.3)$$

is the response function of the array. This is just the response to a wave of infinite wavelength. Since one is interested in the response to a wave of finite length incident from a given direction, i.e., to a wave of wave number  $\vec{k}_0$ , the function calculated was

$$K(\vec{k} - \vec{k}_0) = \sum_{n=1}^N \sum_{m=1}^N e^{i(\vec{k} - \vec{k}_0) \cdot (\vec{r}_n - \vec{r}_m)} \quad (2.4)$$

In all the calculation the response function was normalized by  $K(0)$  which can be shown to be

$$K(0) = N^2, \text{ if } N \text{ is odd,} \quad (2.5)$$

$$K(0) = N(N+1), \text{ if } N \text{ is even.}$$

Therefore the function plotted in the figures is

$$H(k - k_0) \equiv K(k - k_0) / K(0) \quad (2.6)$$

Figures 2.4 through 2.8 show the spatial arrangement of the Isotopes, IAMA, and three isometric arrays. For purposes of illustration the array



## Teledyne Isotopes

response function has been calculated for an incoming wave coming from 225° (southwest). There is nothing special about this direction. The results are representative of other directions of wave incidence as well.

In all the calculations reported below

$$|\vec{k}| = |\vec{k}_0| \quad .$$

The azimuth is direction in which the array was steered, i.e., the direction of  $\vec{k}$ .

Figures 2.9 through 2.12 show the response of the three isometric arrays for wavelengths of 60, 100, 200 and 300 kilometers. These show, as could be expected, that the main lobe widens as the wavelength is increased; that there are a number of side lobes, the largest about 0.25 and 0.30, and that the 21-element isometric array has the lowest side lobes for a given wavelength.

Figures 2.13 through 2.16 show the response of the 21-element isometric array, the LAMA array (20 elements) and the Isotopes array (10 elements) for wavelengths of 60, 100, 200, and 300 kilometers. These show that all of these arrays have main lobes of comparable width and comparable side lobes.

From an examination of the results of these calculations one can conclude that, at least for wavelengths between 60 and 300 km, the response of the Isotopes array (10 instruments) is very similar to that of the LAMA array (20 instruments) and that of a 21-instrument isometric array. It therefore follows that not much improvement in array response could be expected by adding new instruments or changing the spatial arrangement of the present array. It was therefore decided to leave the Isotopes array unchanged.



# ARRAY RESPONSE FUNCTION

WAVELENGTH= 60.0 KM., THETA=225.0 DEG.

△ ISOMETRIC ARRAY, N=21  
○ ISOMETRIC ARRAY N=15  
□ ISOMETRIC ARRAY N=10

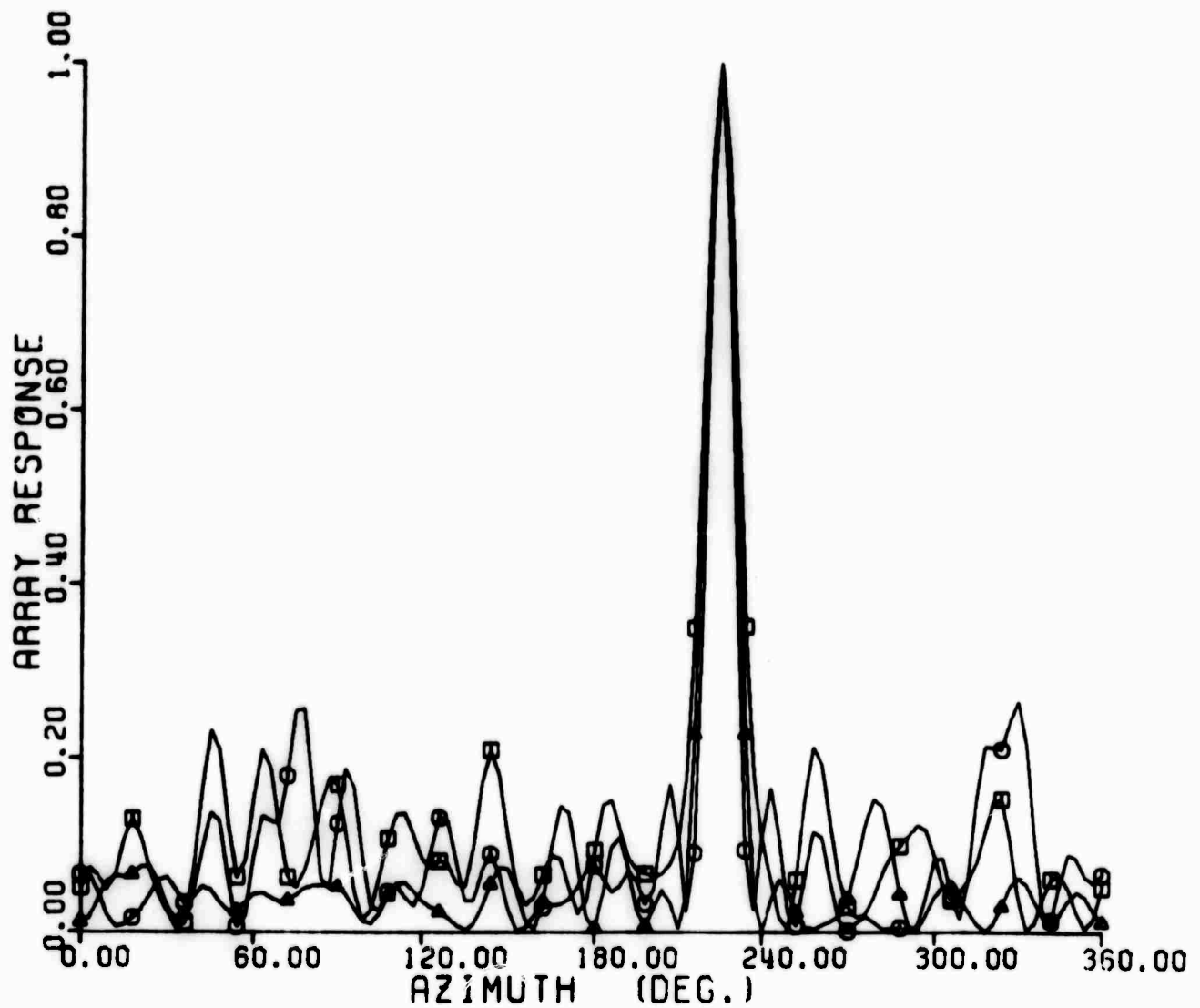


FIGURE 2.9



# ARRAY RESPONSE FUNCTION

WAVELENGTH= 100.0 KM., THETA=225.0 DEG.

△ ISOMETRIC ARRAY, N=21  
○ ISOMETRIC ARRAY N=15  
□ ISOMETRIC ARRAY N=10

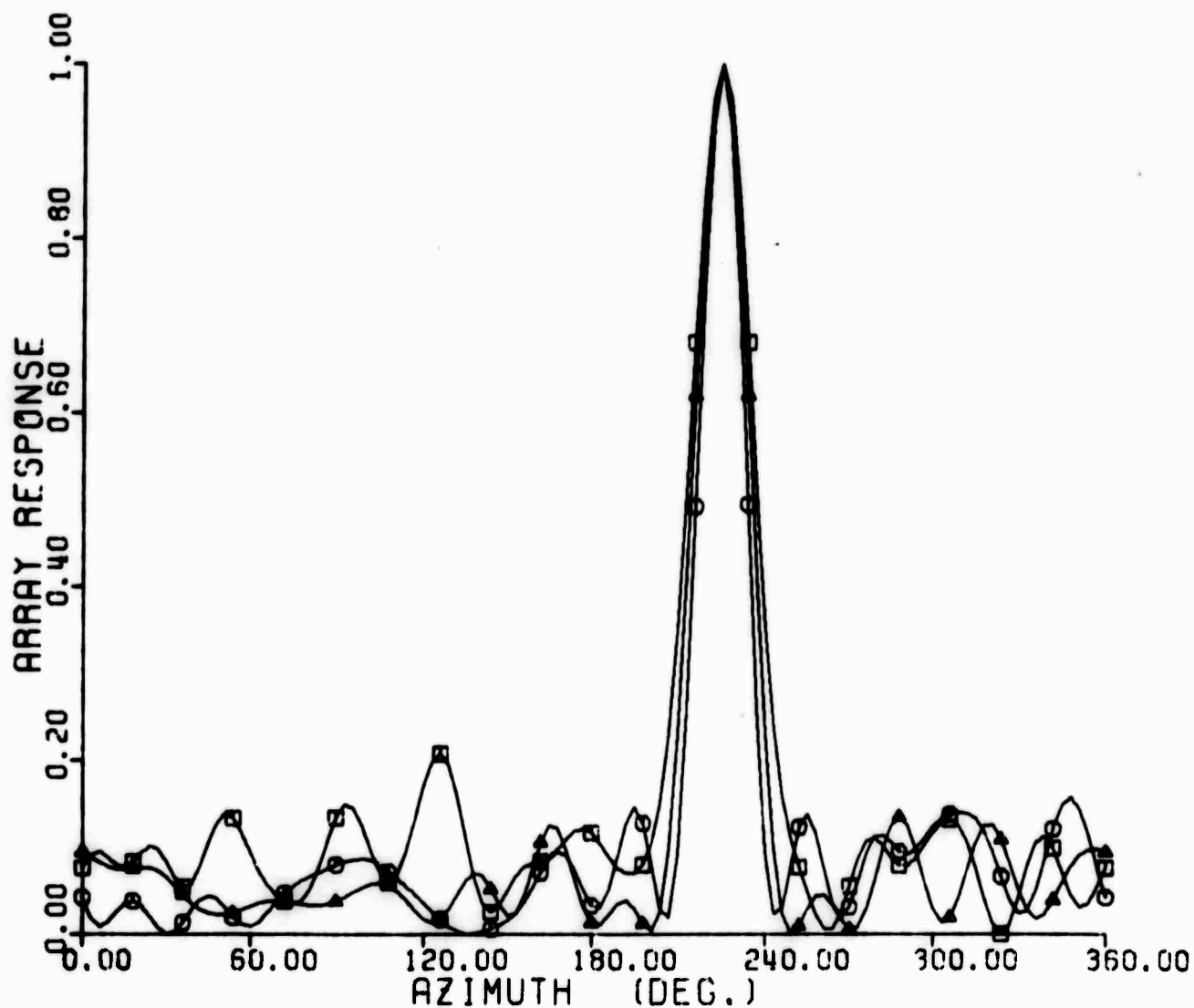


FIGURE 2:10



# ARRAY RESPONSE FUNCTION

WAVELENGTH= 200.0 KM., THETA=225.0 DEG.

△ ISOMETRIC ARRAY, N=21  
○ ISOMETRIC ARRAY N=15  
□ ISOMETRIC ARRAY N=10

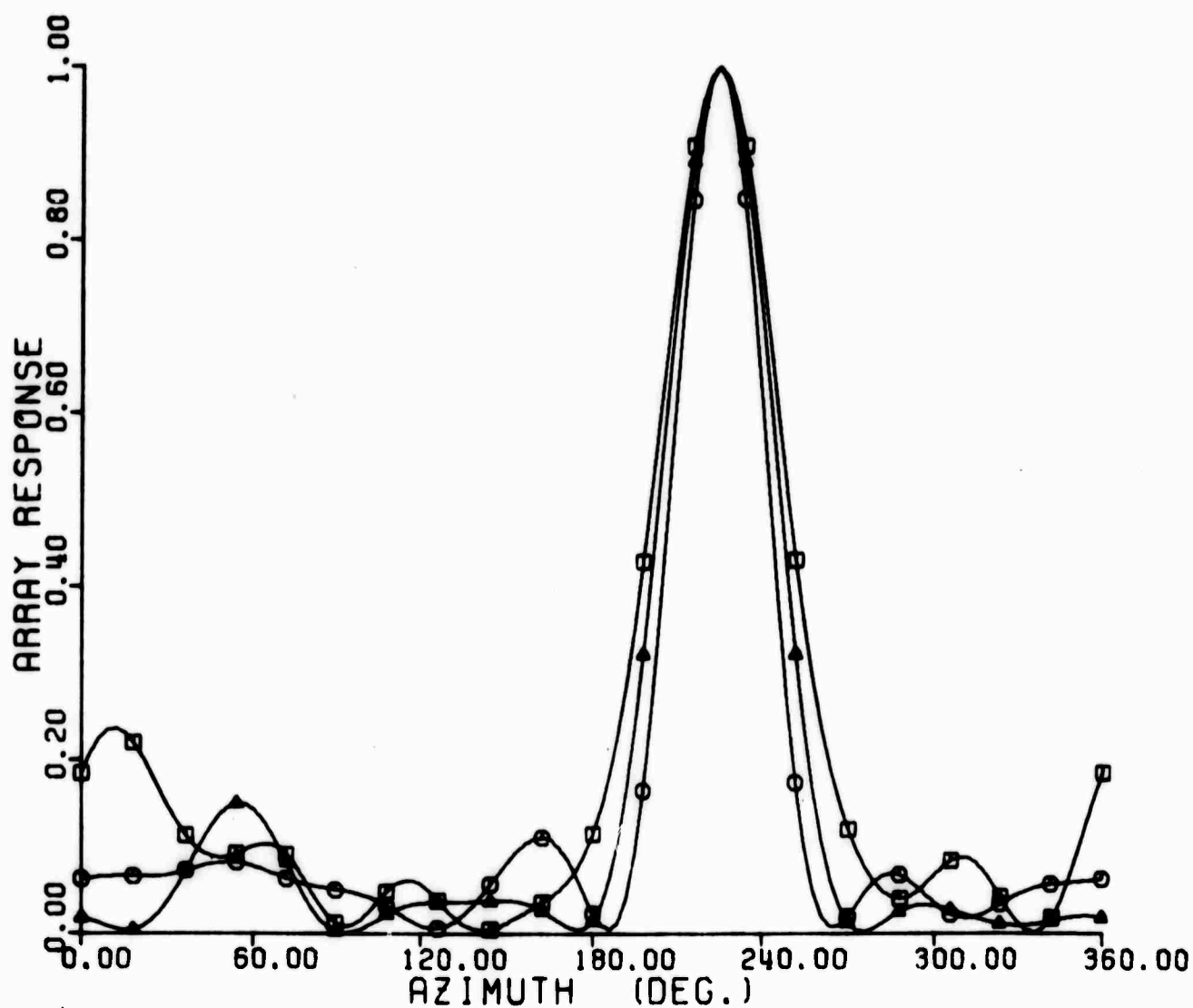


FIGURE 2.11



# ARRAY RESPONSE FUNCTION

WAVELENGTH= 300.0 KM., THETA=225.0 DEG.

△ ISOMETRIC ARRAY, N=21  
○ ISOMETRIC ARRAY N=15  
□ ISOMETRIC ARRAY N=10

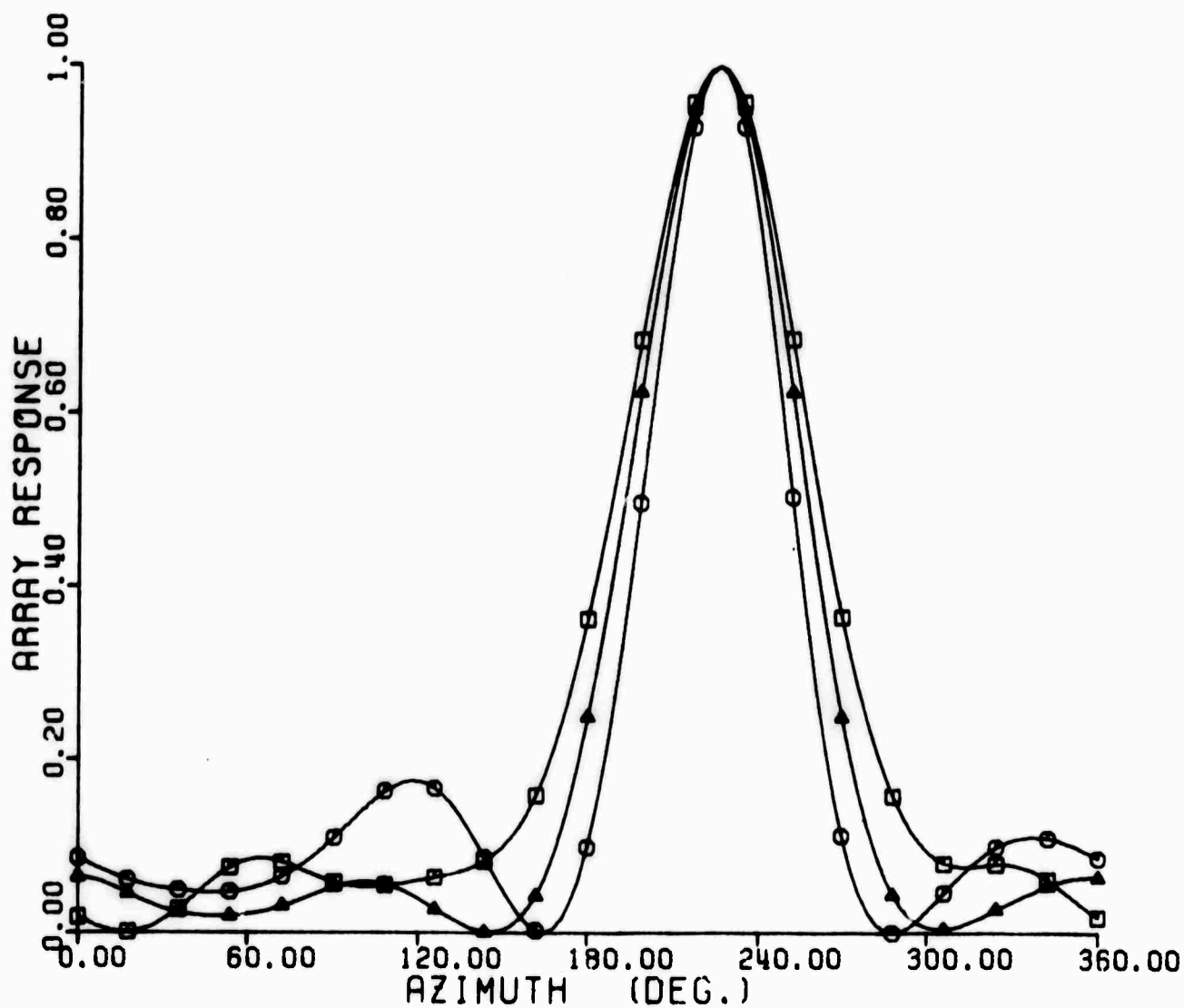


FIGURE 2.12



# ARRAY RESPONSE FUNCTION

WAVELENGTH= 60.0 KM., THETA=225.0 DEG.

△ ISOTOPES ARRAY 10/28/68  
○ LAMA ARRAY 10/28/68  
□ ISOMETRIC ARRAY, N=21

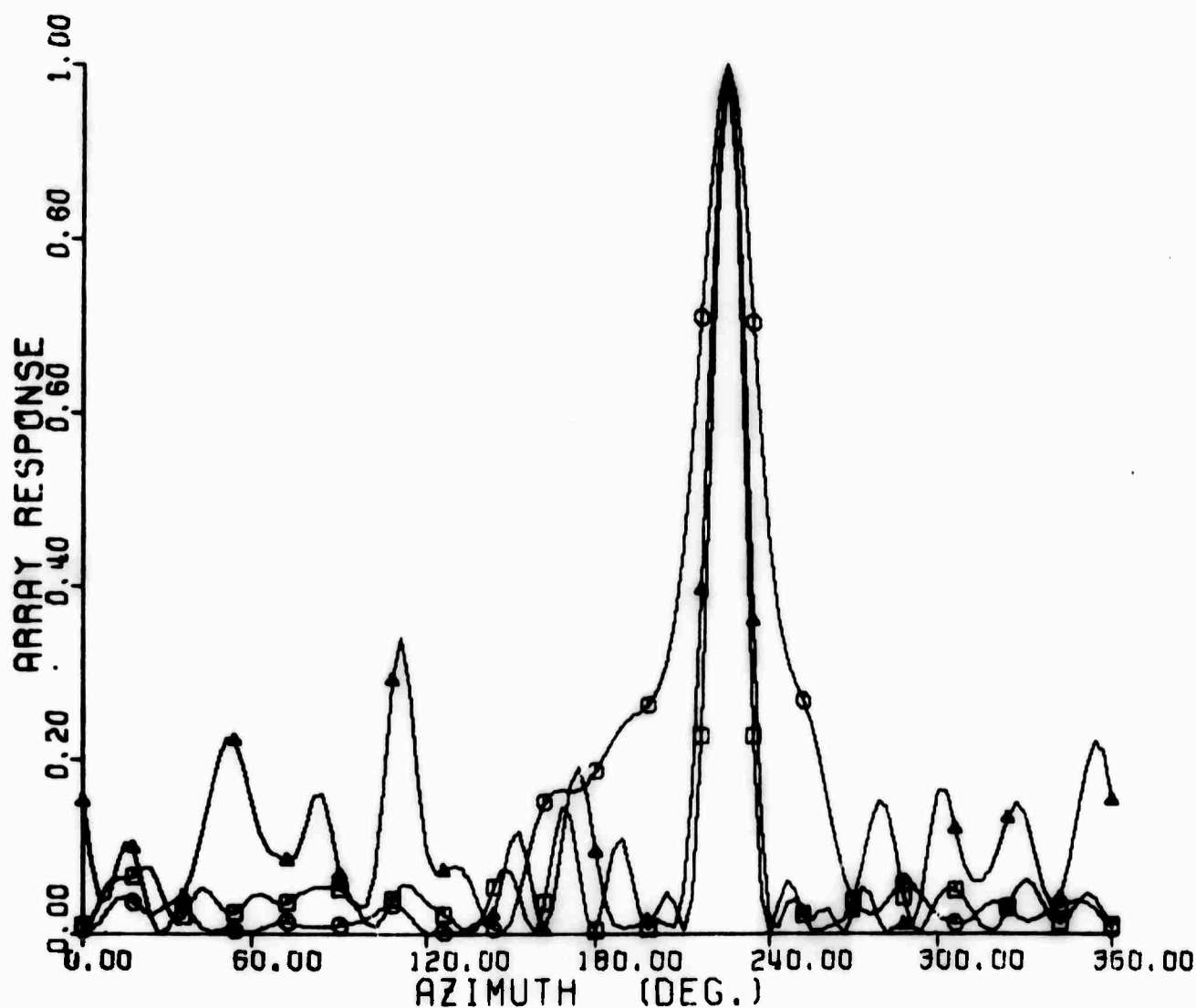


FIGURE 2.13



# ARRAY RESPONSE FUNCTION

WAVELENGTH= 100.0 KM., THETA=225.0 DEG.

△ ISOTOPES ARRAY 10/28/68  
○ LAMA ARRAY 10/28/68  
□ ISOMETRIC ARRAY, N=21

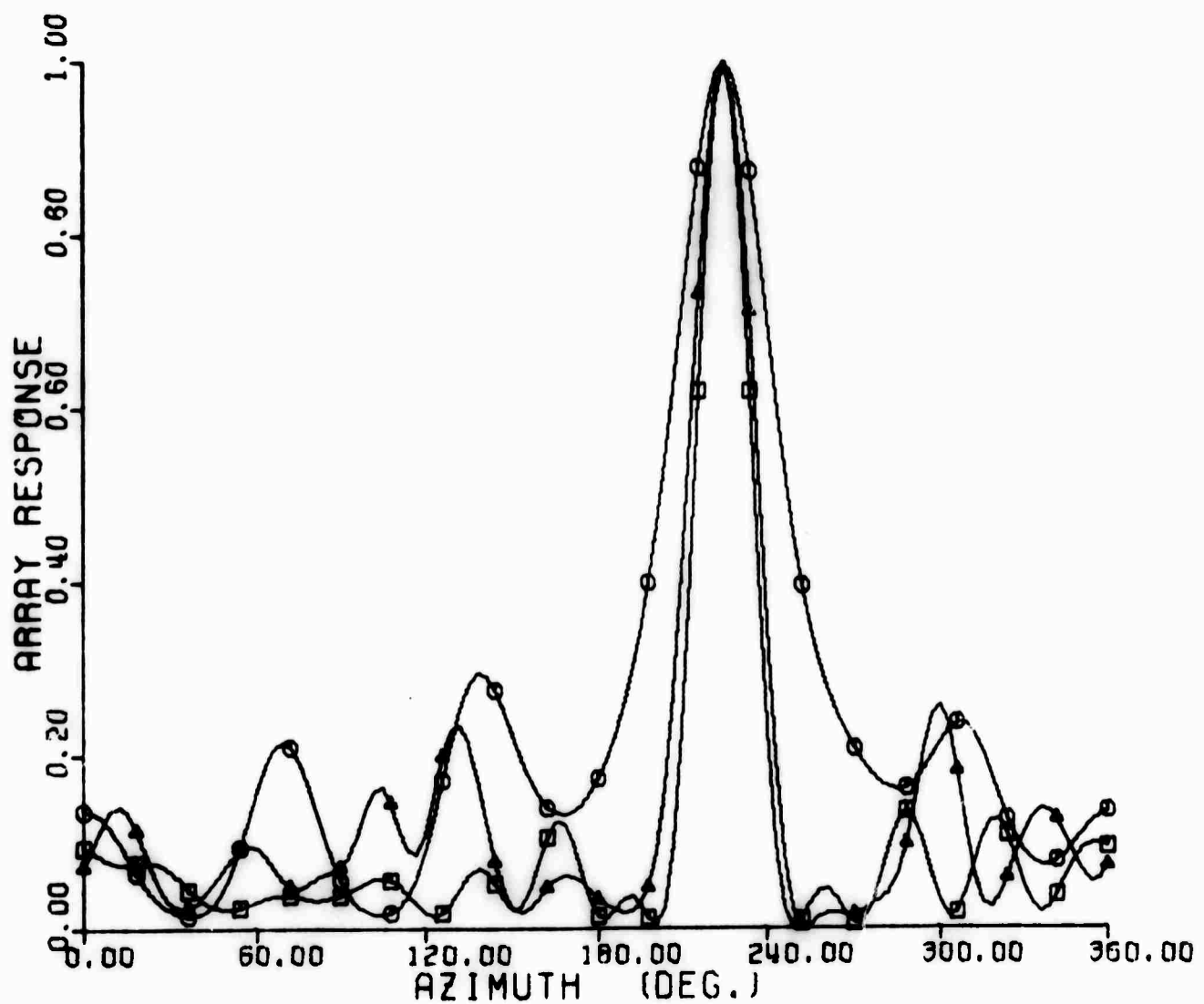


FIGURE 2.14



# ARRAY RESPONSE FUNCTION

WAVELENGTH= 200.0 KM., THETA=225.0 DEG.

△ ISOTOPES ARRAY 10/28/68  
○ LAMA ARRAY 10/28/68  
□ ISOMETRIC ARRAY, N=21

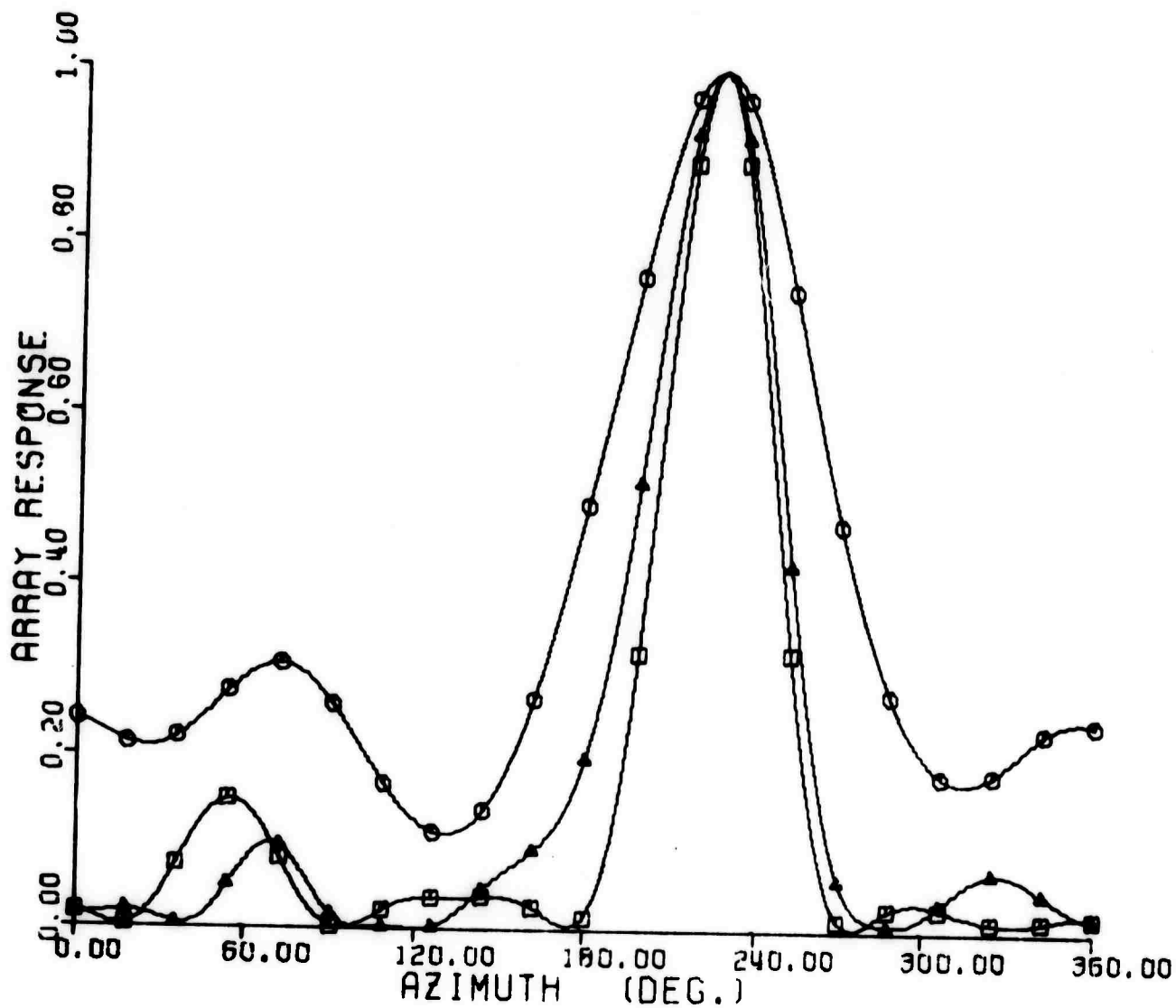


FIGURE 2.15



# ARRAY RESPONSE FUNCTION

WAVELENGTH= 300.0 KM., THETA=225.0 DEG.

△ ISOTOPES ARRAY 10/28/68  
○ LAMA ARRAY 10/28/68  
□ ISOMETRIC ARRAY, N=21

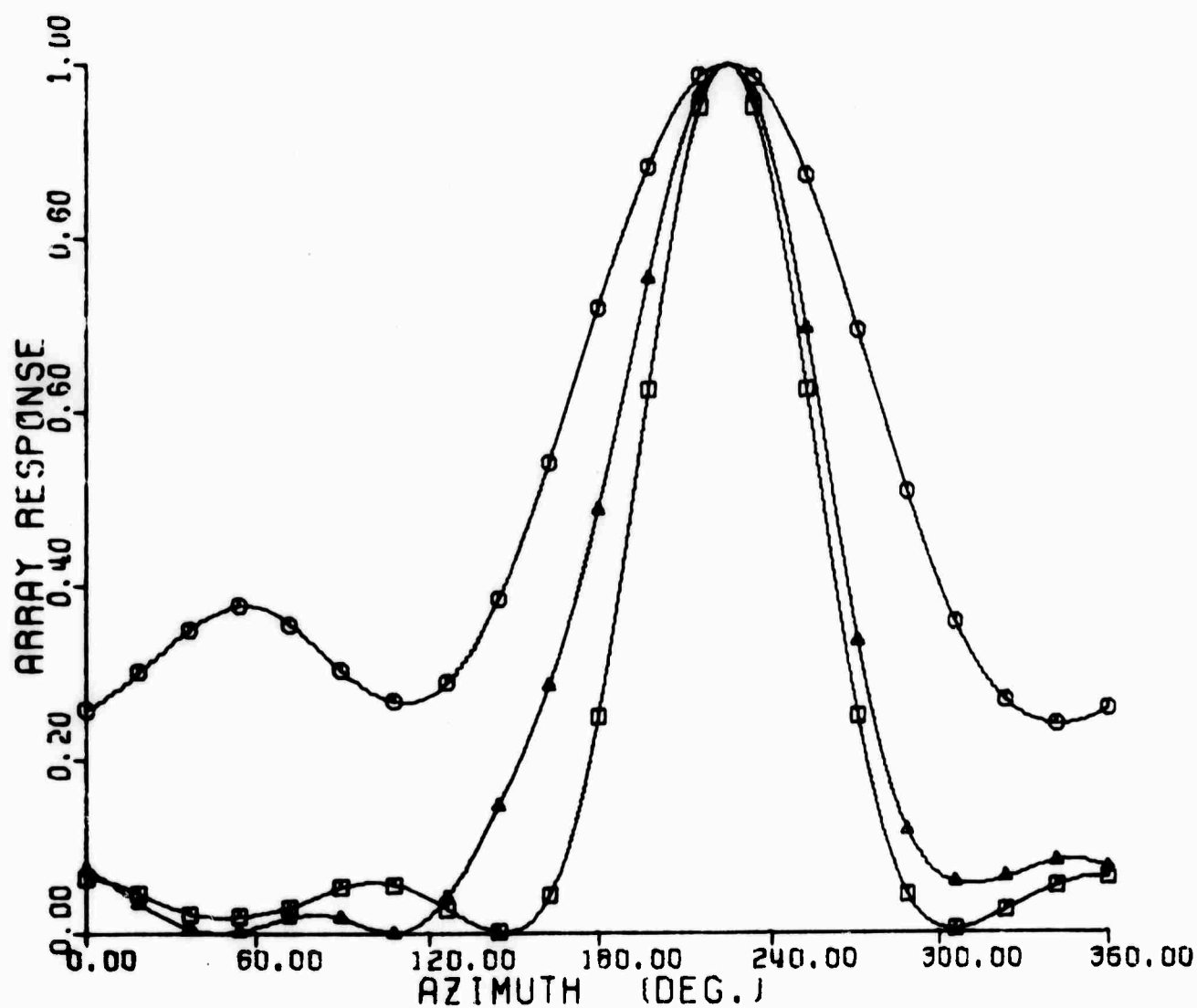


FIGURE 2.16



## Teledyne Isotopes

### 2.2 Event-Related Phenomena

#### 2.2.1 Atmospheric Nuclear Tests

During the operation of the Teledyne Isotopes array, atmospheric effects due to the Chinese thermonuclear explosion of 29 September 1969 were detected.

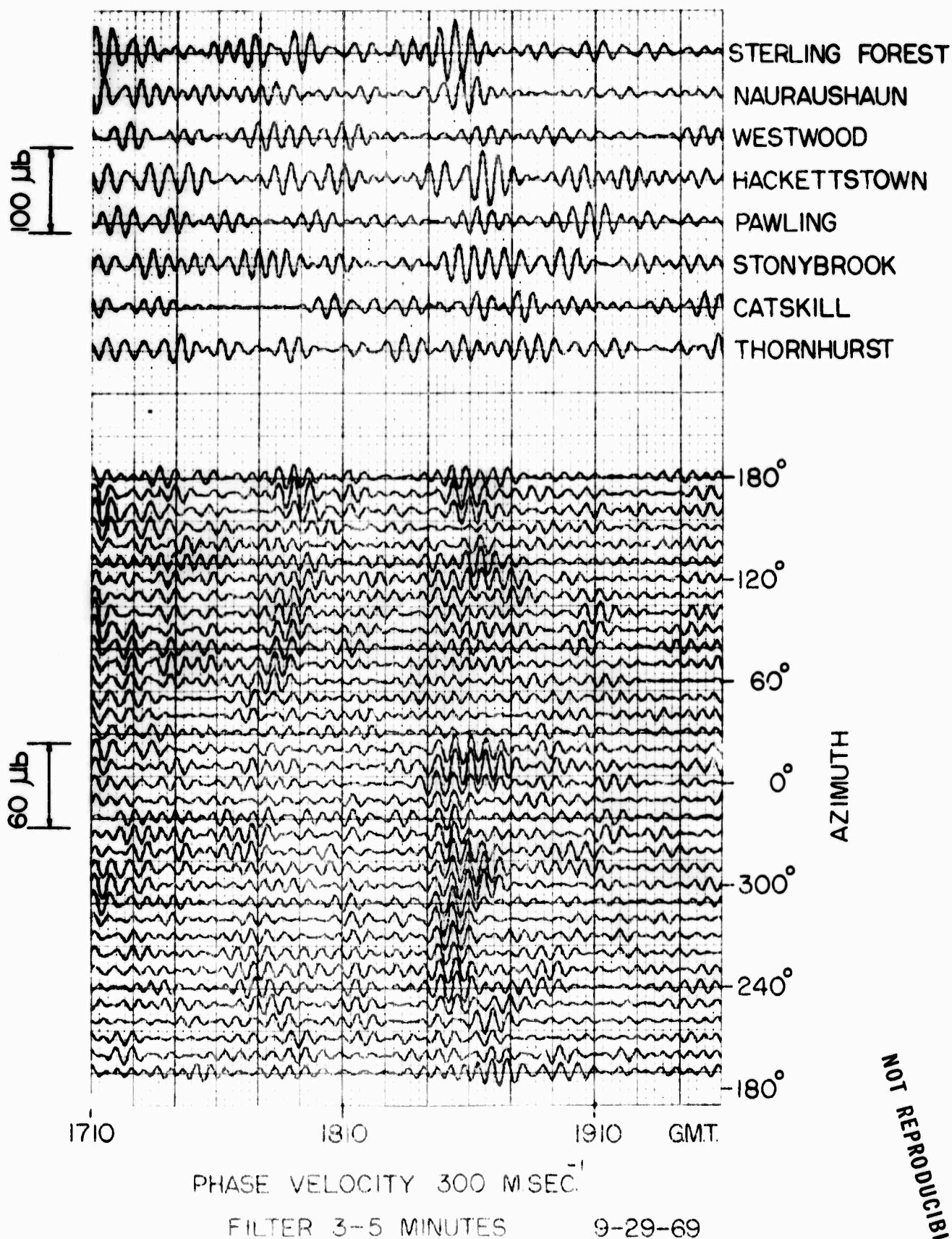
- a) A signal with periods between 2 and 5 minutes arrived at about 1830 G.M.T. Beamforming analyses gave a phase velocity of  $320 \pm 20$  m/sec and an azimuth of arrival of  $10^\circ$ , that is, travelling along the short great circle path from the Lop Nor test site to the array.
- b) At about 0018 G.M.T. on 30 September 1969, a wave train having periods between 12 and 18 minutes was observed. The direction of arrival resulting from the beamforming analyses was about  $180^\circ$ , that is, coming from the south by the long great circle path, with a phase velocity of  $580 \pm 20$  m/sec.

The zero time computed from the short period (2 - 5 min) arrival was 08:50 G.M.G.  $\pm 20$  minutes. The group velocity for the long period (12 - 18 min) computed from the arrival time was  $540 \pm 20$  m/sec.

The signal to noise ratio is low in both ranges as has been reported earlier by Tolstoy (1967, 1968). Thus, filtering and beamforming were necessary to extract the signal from the background. Filtering of the time series was carried out by transforming them into the frequency domain with a fast Fourier transform; the coefficients of the unwanted frequencies were set equal to zero, and the remaining Fourier terms were transformed back to the time domain.

Prior to beamforming the data were passed through a 3 - 5 minute filter in the case of the short period arrival and a 12 - 18 minute filter for the long period arrival. These filters gave the sharpest beamforming results (Figures 2.17 and 2.18)





NOT REPRODUCIBLE

FIG. 2.17 Beamforming applied to 8 microbarograph stations. The assumed phase-velocity was 300 m. sec<sup>-1</sup>. The data was filtered with a 3-5 minute bandpass Fourier filter.



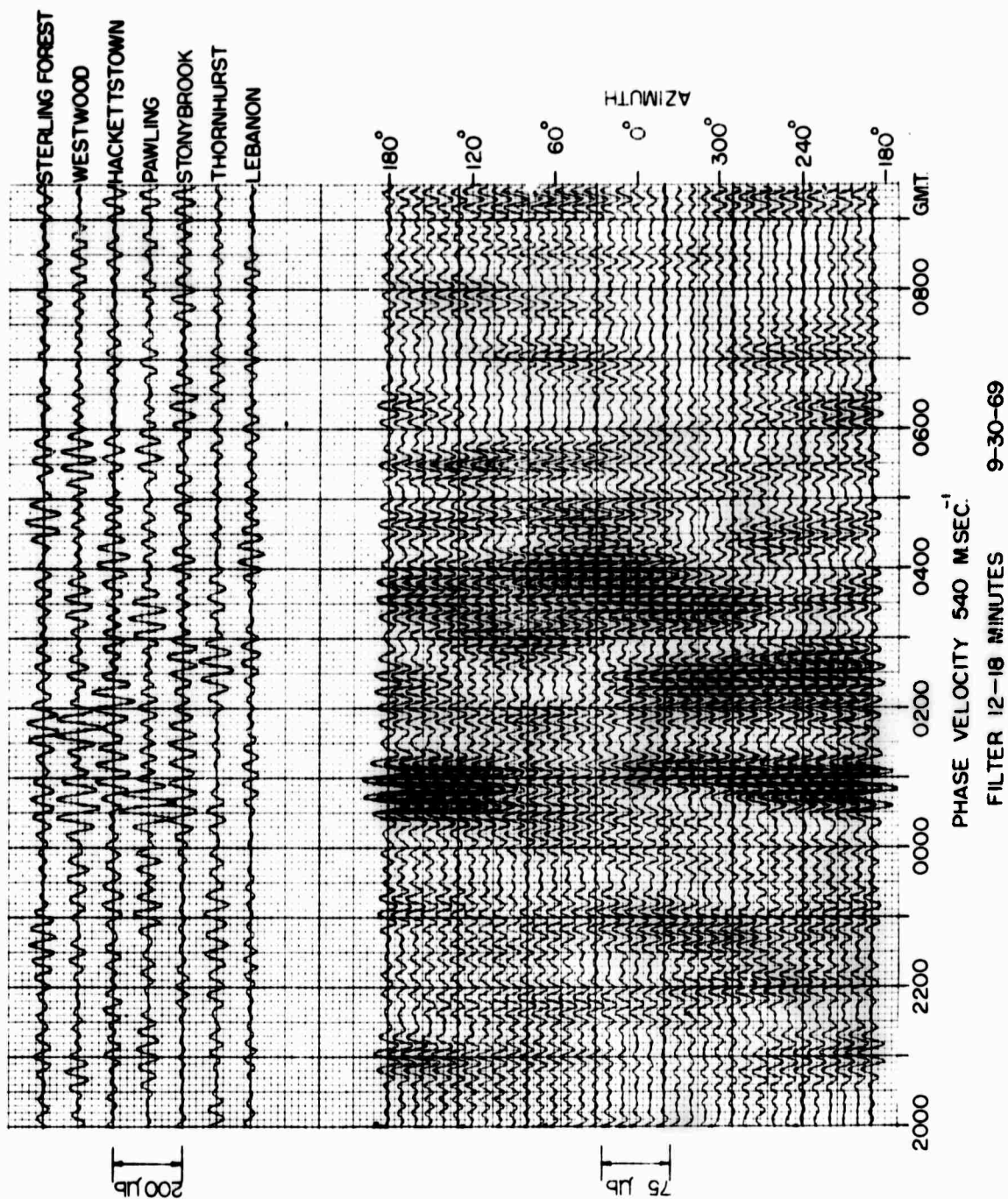


FIG. 2.18 Beamforming of 7 microbarograph stations, assuming a phase-velocity of 540 m. sec<sup>-1</sup>. The data was filtered with a 12-18 minute filter.

NOT REPRODUCIBLE



The beamforming for the short period show a large side lobe. This side lobe appears to be a characteristic of the array as suggested by Figure 2.19 which is the theoretical array response function for a wavelength equal to 72 km corresponding to a period of 4 minutes and a phase velocity of 300 m/sec.

The longer period beamforming shows a broad response but there are no side lobes. The theoretical response for the long period shows the same characteristics,

A more quantitative picture can be obtained by calculating for each direction a quantity which is proportional to the average power

$$P = \int_{t_1}^{t_2} [P(t)]^2 dt \quad (2.7)$$

where  $p$  is the sum of the amplitudes of the signals delayed according to an assumed phase velocity, and divided by the number of elements of the array. Figure 2.20 shows the result of applying this technique to the time interval 1830 - 1850 Z for an assumed phase velocity of 300 m/sec. If one lets the phase velocity vary in the range  $V_1 \leq V \leq V_2$  one obtains Figure 2.21 which is the perspective view of a three-dimensional surface. The value of  $P$  in this figure is along the  $z$  axis; the phase velocity along the  $y$  axis, and the direction of arrival along the  $x$  axis.

Application of this method to the time intervals 1810 - 1830 G.M.T. (prior to the arrival), 1830 - 1850 G.M.T. (containing the signal); and 1850 - 1910 G.M.T. (after the arrival) permits a comparison between the background and the signal for the short period arrival (Figure 2.22). If we now pick up the phase velocity for which  $P$  shows the maximum, and the procedure is applied to overlapping time intervals, a time history of the average power as it crosses



72 KM.

□ MICROBAROGRAPH ARRAY

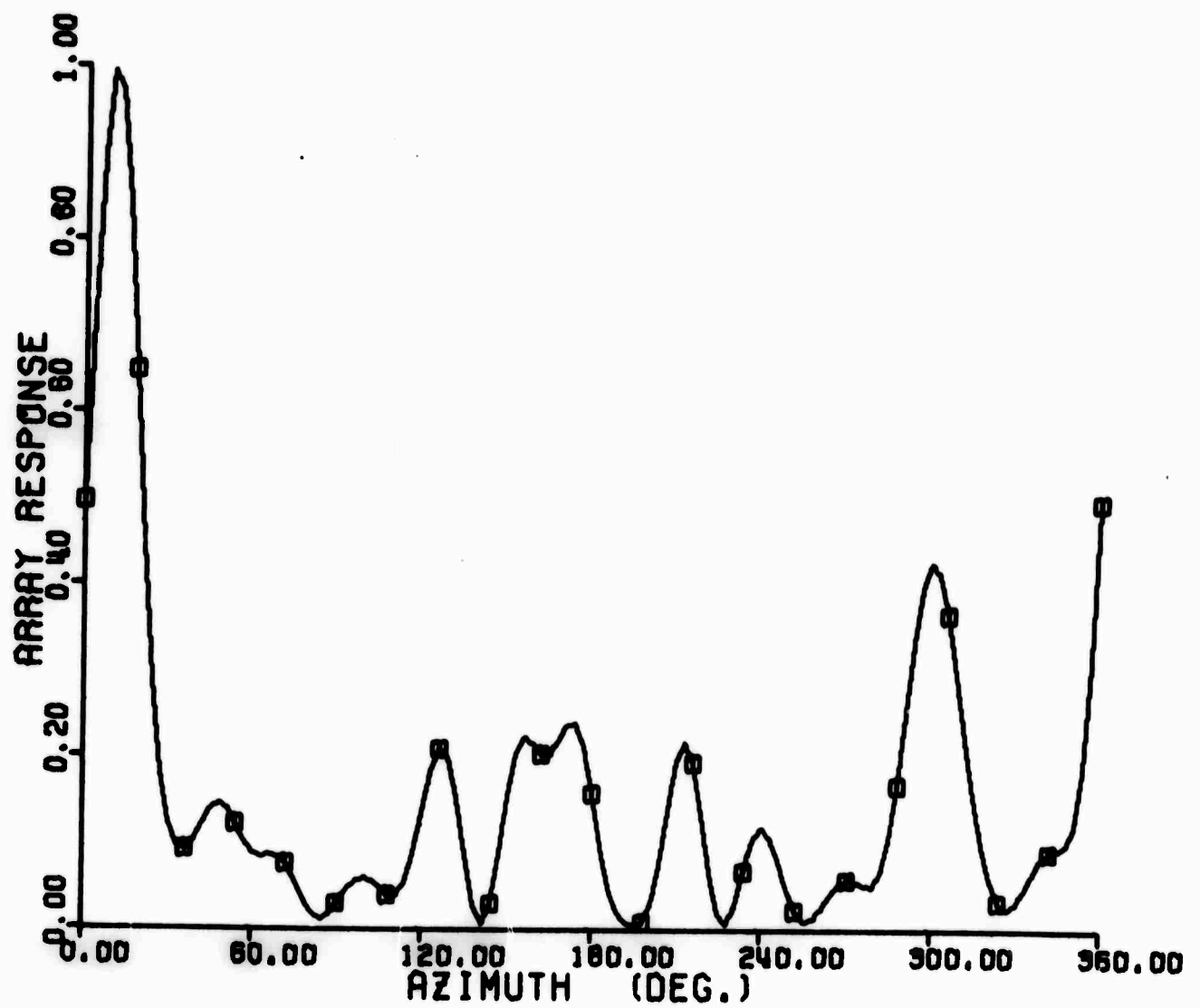


FIG. 2.19 Theoretical array response using the stations of Fig. 2.17.



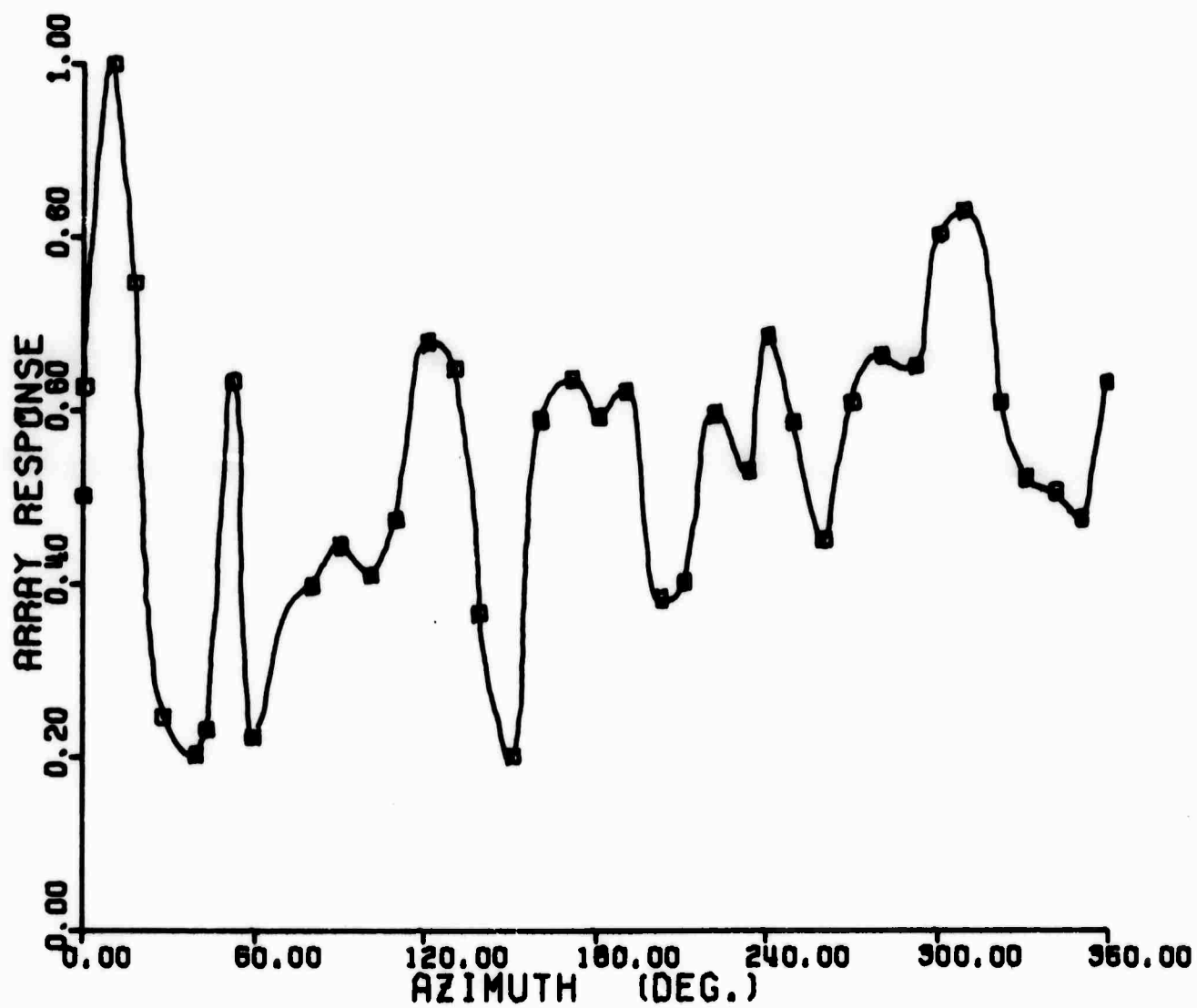


FIG. 2.20 Normalized result of the square and integration technique applied to the time interval 1830-1850 G.M.T. on September 29, 1969 for a phase velocity  $V = 300 \text{ m. sec}^{-1}$ .



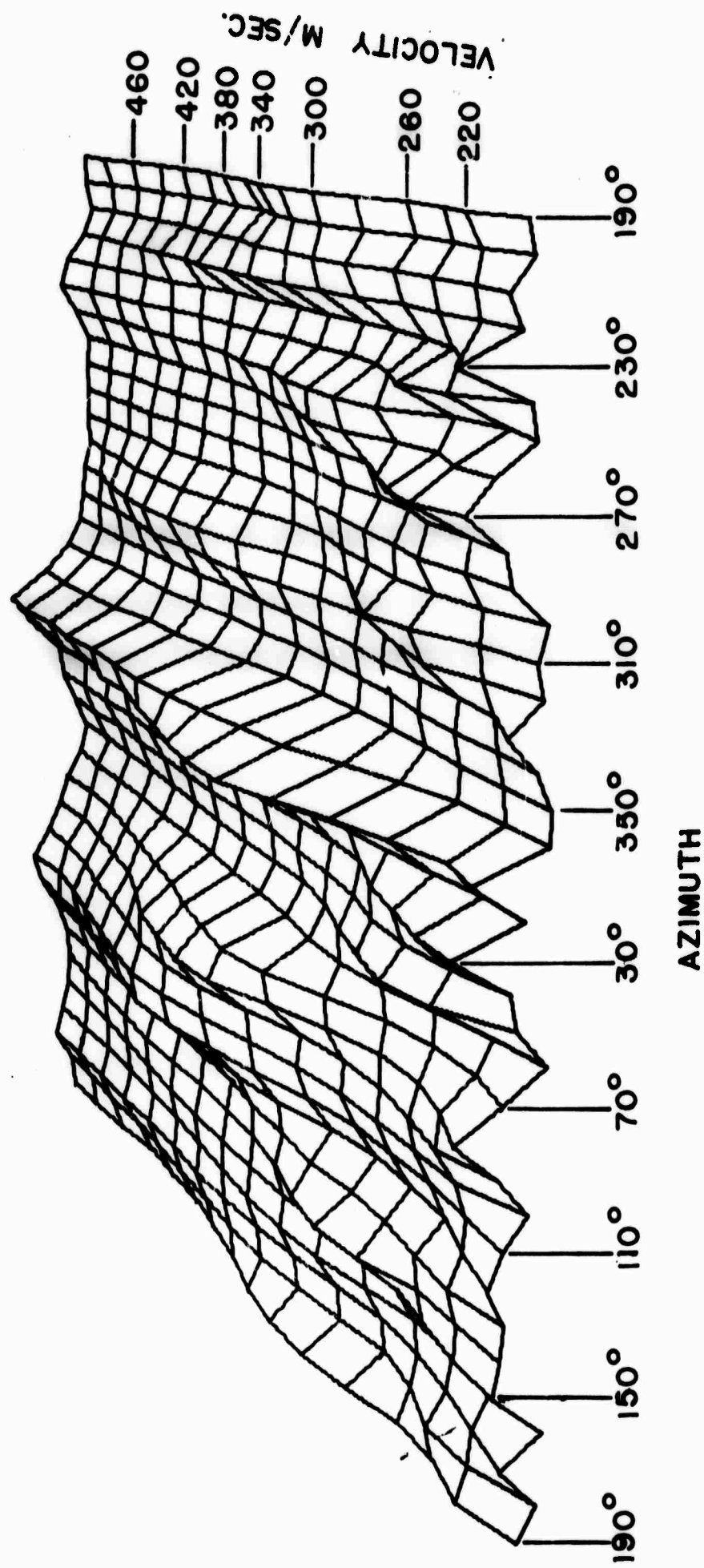
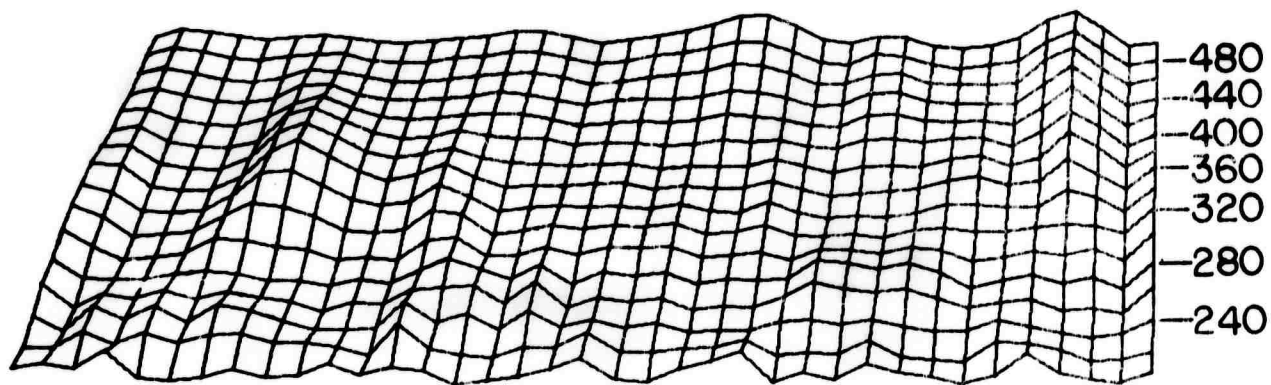
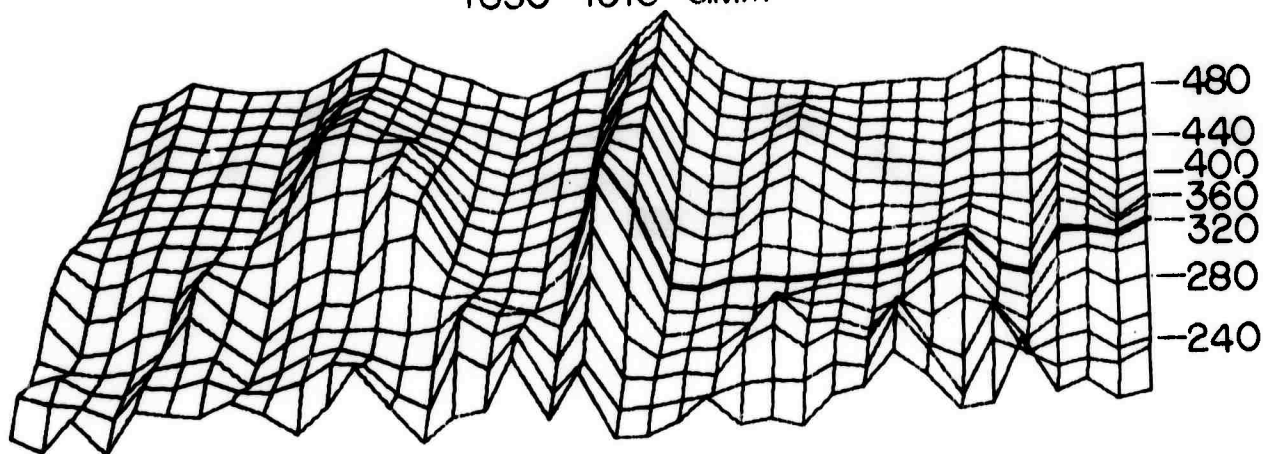


FIG. 2.21 Perspective view of P for the time interval 1830 - 1850 G.M.T. on September 29, 1969 showing the variation of P with phase-velocity V and azimuth  $\theta$ .

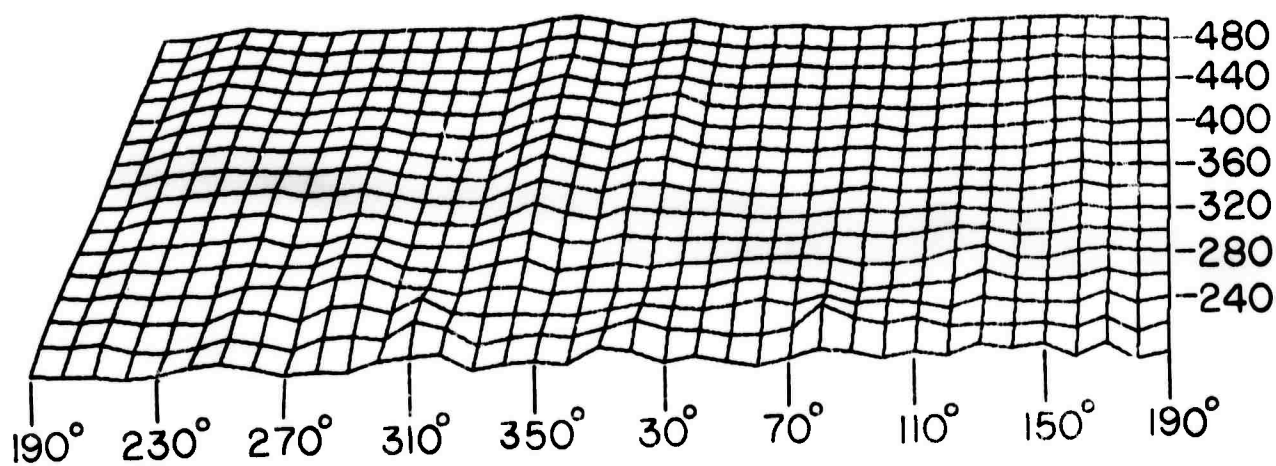




1850-1910 G.M.T.



1830-1850 G.M.T.



AZIMUTH

1810-1830 G.M.T.

VELOCITY METERS SEC.<sup>-1</sup>

FIG. 2.22 Same as Fig. 2.21 but for three different time intervals.



the array is obtained. Figure 2.23 displays the perspective view of the surface  $P(\theta, t)$  for a phase velocity of 300 m/sec and a bandpass filter of 3 - 5 minutes, that is, for wavelengths between 54 and 90 km and covering the time interval 1750 - 1910 G.M.T. The integration window was 20 minutes long and the overlapping was 18 minutes.

Figure 2.24 shows the result of applying the above procedure to the long period arrival for a phase velocity of 540 m/sec and a bandpass filter of 12 - 18 minutes. The integration window in this case was 60 minutes and the overlapping was 54 minutes.

The amplitude of the pressure fluctuation of the long period wave was 52  $\mu$ bars (peak to trough). The short period wave had an amplitude of 24  $\mu$ bars (peak to trough).

A comparison between these observations and the observations of Tolstoy of the nuclear events of Lop Nor on 17 June 1967 and the French test in the South Pacific on 24 August 1968 (Table 2.2) permits us to draw some conclusions:

i) Short period waves. These waves arrive with group velocities of the order of 300 m/sec. The center frequency of the three events listed in the table takes different values in each case. These values range from 0.002 Hz (8 minutes) to 0.0067 Hz (2.5 minutes); that is, the bandwidth of these arrivals is 0.00167 Hz - 0.0167 Hz or 1 minute - 10 minutes. The average phase velocities are  $300 \pm 10$  m/sec and the wavelengths range from 18 km to 180 km. The arrival corresponding to the long great circle path cannot be recognized.

ii) Long period waves. The group velocities of these waves are of the order of 550 m/sec and the phase velocities of the order of  $570 \pm 30$  m/sec. The center frequencies also vary from event to event as in the short period case. For



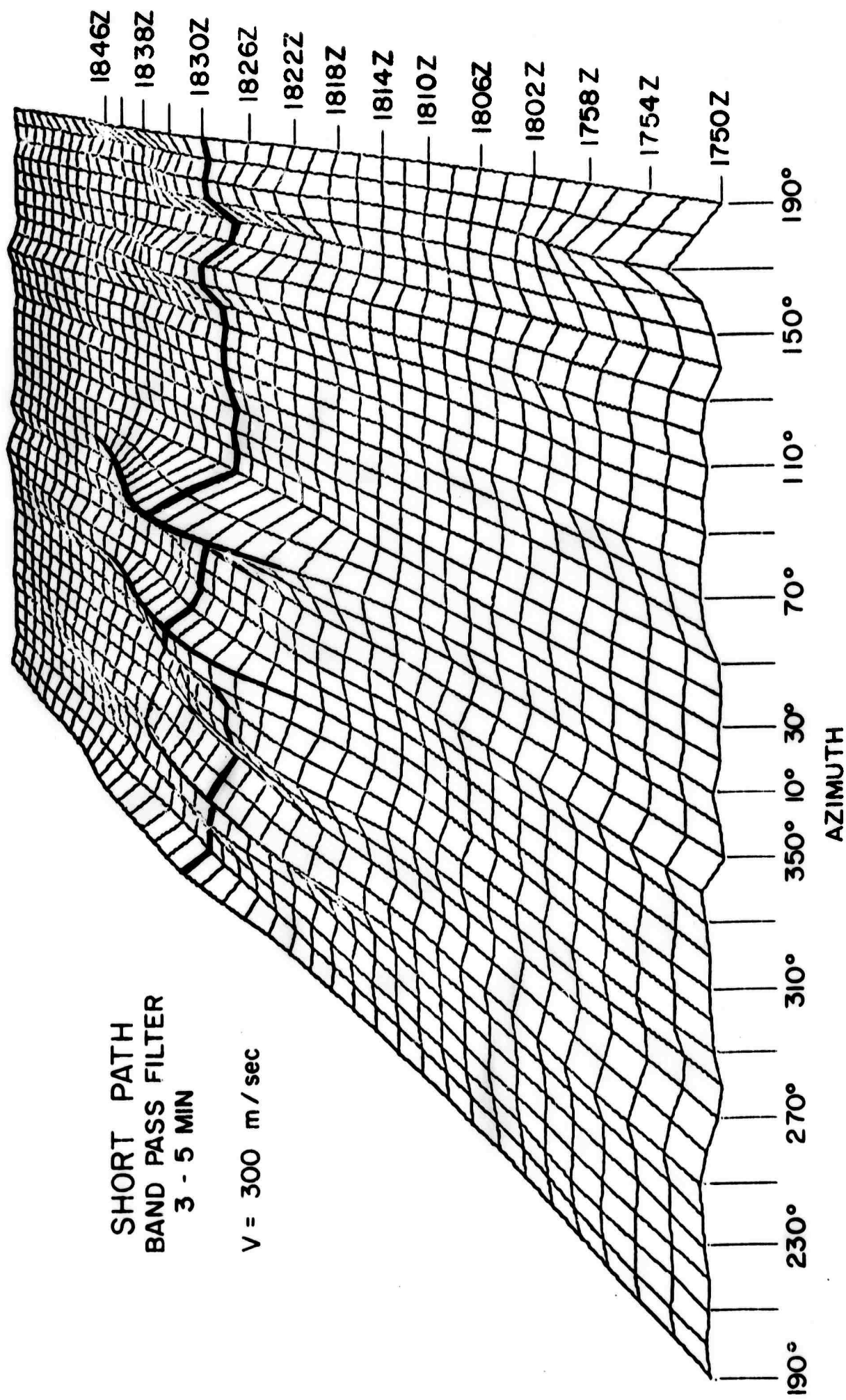


FIG. 2.23 Result of square and integration for a fixed phase velocity  
 $V = 300 \text{ m. sec}^{-1}$  using overlapping time windows. The data  
 corresponds to the short period arrival.



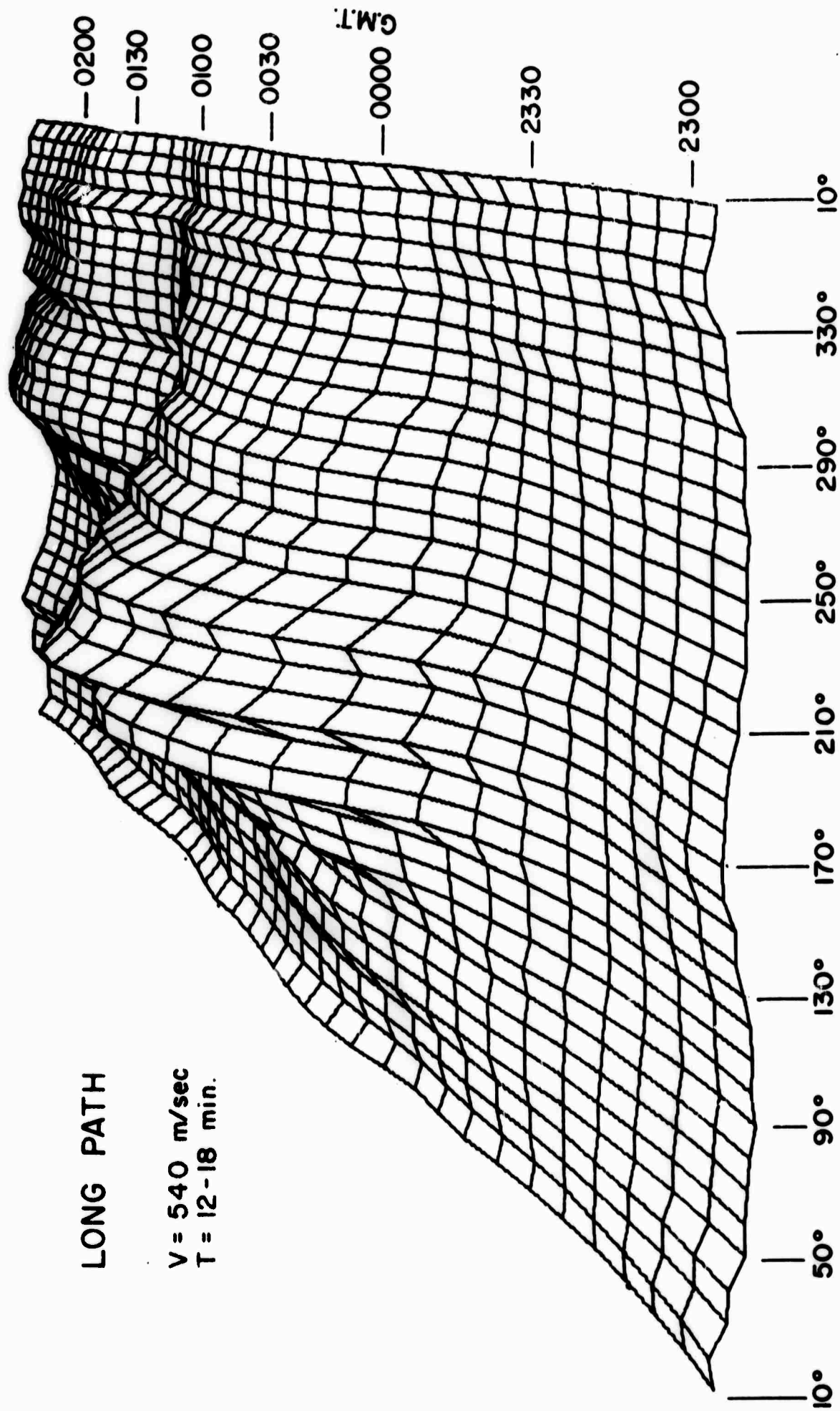


FIG. 2.24 Result of square and integration for a fixed phase velocity  $V = 540 \text{ m. sec}^{-1}$ .  
 The data corresponds to the long-path long period arrival.



## Teledyne Isotopes

the three events compared the center frequencies are: 3.64 CPM (16.5 minutes), 4.62 CPM (13 minutes), and 4.0 CPM (15 minutes) respectively. The bandwidths go from 0.000925 Hz to 0.00138 Hz (18 minutes - 12 minutes). Normally both the short and the long great circle path arrivals can be identified. However, the short great circle path arrival corresponding to the 29 September 1969 explosion could not be extracted from the background while the long-path arrival required very little filtering before it could be identified.

iii) It is interesting to know that the energy of the explosion can be propagated in such a wide range of periods. It is also important to notice that the events compared may be telling us something about the variation of the structure due to seasonal change. In other words, the events occurred during late spring, mid-summer and early fall respectively.

iv) The lack of short-path arrival for the event of 29 September 1969 could probably be explained by the interaction of a wind structure with the travelling wave as it propagated through the polar regions in the northern hemisphere.

TABLE 2.2

	<u>17 June 1967</u>		<u>24 August 1968</u>		<u>29 Sept 1969</u>	
	Short Period Range	Long Period Range	Short Period Range	Long Period Range	Short Period Range	Long Period Range
Period T (min)	5-10	15-18	2-3	12-14	2-5	12-18
Phase Velocity V (m/sec)	300 $\pm$ 10	600 $\pm$ 20	300	550 $\pm$ 20	300 $\pm$ 10	540 $\pm$ 20
Group Velocity U (m/sec)	300	550	300	550	300	540



Teledyne Isotopes

### 2.2.2 SATURN-APOLLO IX Associated Signals

During February a 6.03 MHz doppler transmitter was installed at Sterling Forest. This signal is reflected at a higher altitude than the 4.8 MHz signal. Both the 6.03 MHz and 4.8 MHz doppler ionosounders recorded an interesting phenomenon at the time of the APOLLO IX launch on March 3. The raw data from the 4.8 MHz and 6.03 MHz doppler are shown on Figure 2.25. The vertical scale is 1.0 Hz/inch and the horizontal scale is 10 min/inch. The sample rate was 10 points/minute. The starting time for the data shown in Figure 2.25 is 16:13:30 GMT on 3 March 1969. It would appear that between 17:00 and 17:10 there is definite change in the character of the signal on both channels.

The raw data was passed through a bandpass (0.2 to 2.0 cycles/min) digital filter. The filtered data for the 4.8 MHz and 6.03 MHz dopplers are plotted in Figure 2.26. The change in the character of the signals is even more apparent on these plots. This change takes place between 17:05 and 17:15. The amplitude of the oscillations increases and the average period decreases to about 1 to 2 minutes. This change lasts for about 40 minutes.

Cape Kennedy is approximately 1500 kilometers from Westwood. For a signal travelling at a speed of 500 m/sec, the travel time is about 50 minutes. It is therefore possible that this signal is an acoustic-gravity wave which was generated at the SATURN-APOLLO IX launch and is now propagating in the atmosphere. Since the planned doppler array is not yet functioning it is impossible to determine the direction from which the signal came.

Signals with the same characteristics as described above were recorded during the SATURN-APOLLO XII launch on 14 November 1969. At that



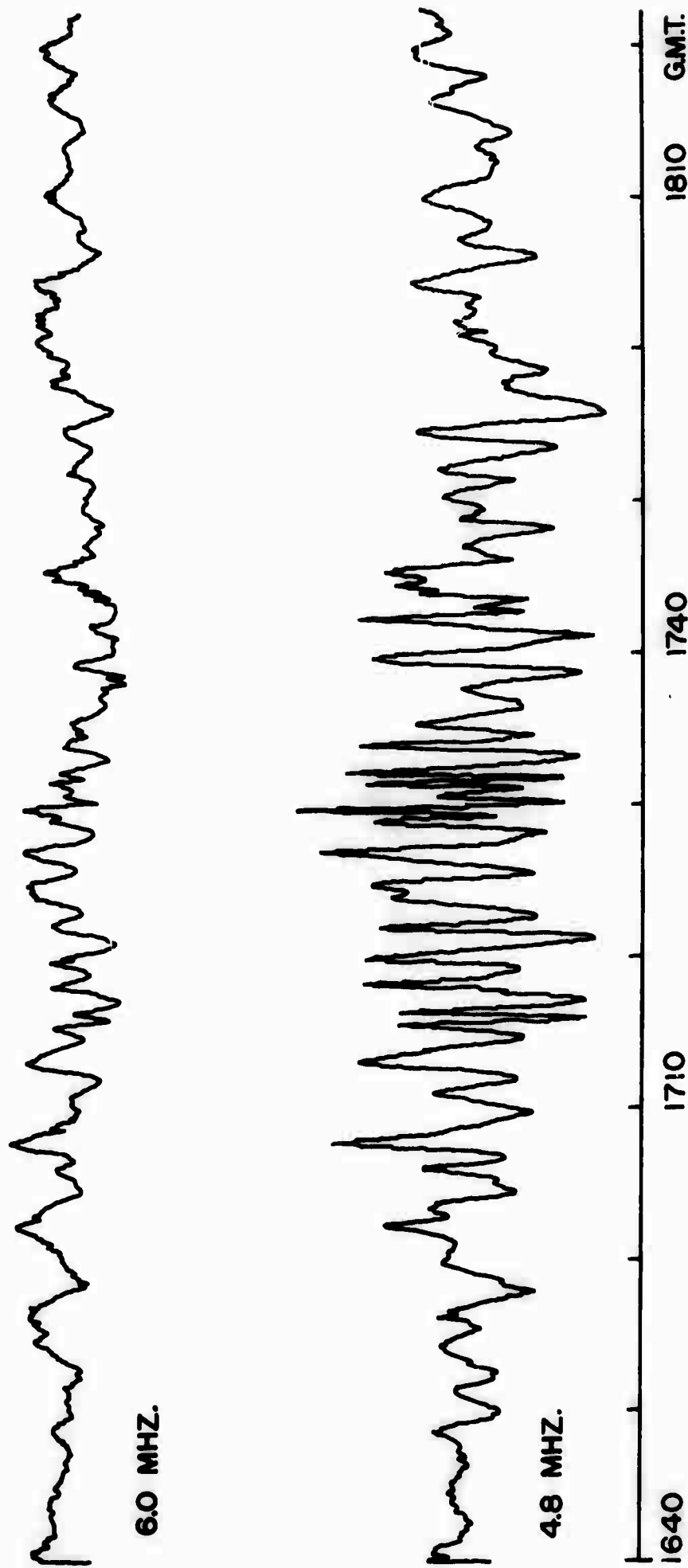


FIG. 2-25 Unfiltered doppler records showing acoustic signals generated by Saturn Apollo IX on March 3, 1969.



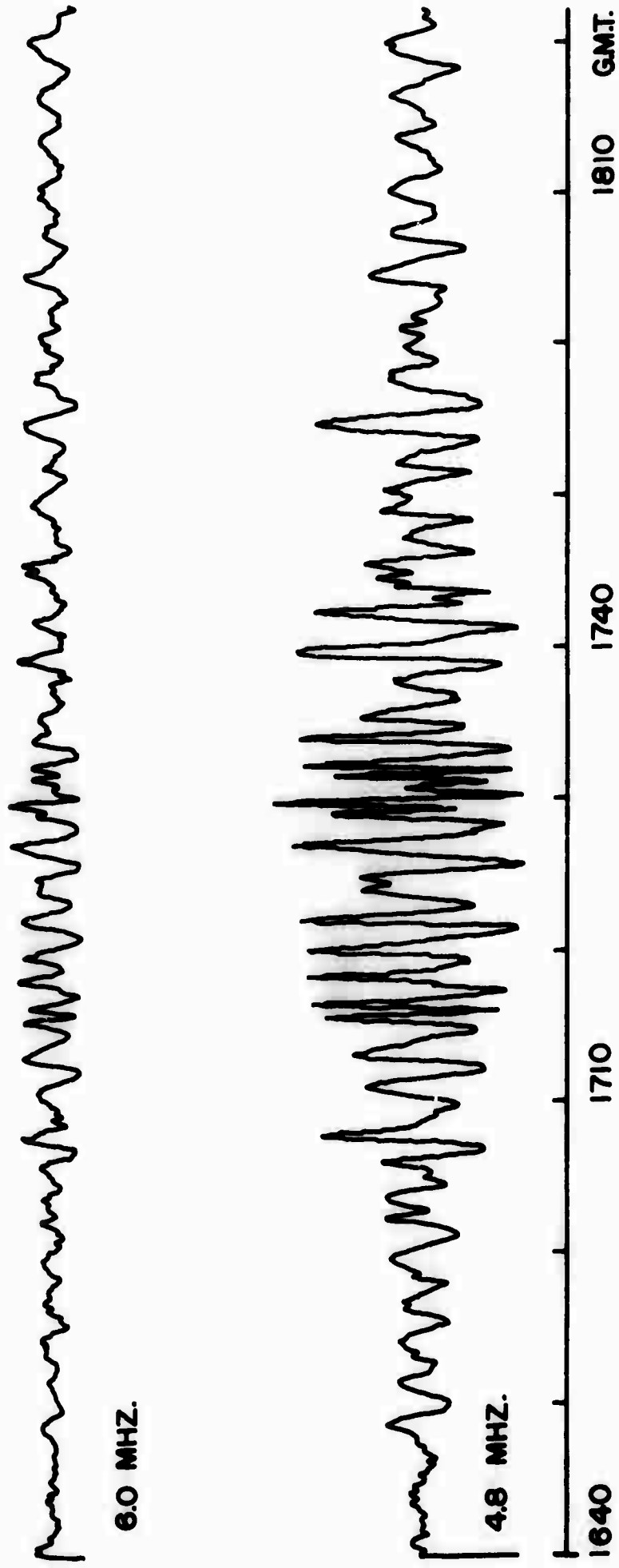


FIG. 2.26 Filtered doppler records corresponding to Saturn Apollo IX generated signals. Band pass filter was 0.5 - 5 min.



## Teledyne Isotopes

time the phase-path sounder array consisted of four elements at 4.8 MHz and one element at 6.03 MHz. The direction of arrival obtained from the array analyses was about  $170^\circ$  measured CW from geographic north. This confirms our early hypothesis about the origin of the signals on 3 March 1969.

### 2.2.3 Correlation of Atmospheric Pressure Waves with Ionospheric Phase-path Sounder Signals

During the summer of 1968, Hudson Laboratories of Columbia University was operating, north of New York City, a large aperture (several hundred kilometer) microbarograph array for the study of long-period atmospheric pressure waves. The array (described by Herron et al., 1969) was recording data throughout the interval during which there were five high energy disturbances in the South Pacific. In the latter part of the summer, a vertical incidence ionospheric doppler sounder was installed at the center of the array and was recording during the event of 24 August 1968. The doppler sounder measured the rate of change of vertical motion of electrons in the ionosphere. A cw signal (4.8 MHz) was transmitted from the Sterling station and was received at Hudson Laboratories, 36 km distant, after having been reflected from the lower F region of the ionosphere at nearly vertical incidence.

After the project was transferred to Teledyne Isotopes the analysis of the data was continued and the principal findings are described below.

#### Pressure signals

Tolstoy and Herron (1970) have reported the existence of long-period (10-25 min), high-velocity ( $600 \text{ m sec}^{-1}$ ) atmospheric pressure signals identified as surface gravity waves. Generated by high energy events and detectable, thus far, only through the signal-to-noise enhancement of array



## Teledyne Isotopes

processing techniques, the waves have been observed travelling the short and long great-circle paths away from the sites of the events. The pressure signal arrived from an azimuth of  $230^\circ$  at about 2300Z on 24 August 1968.

### Phase-path sounder signals

At the time at which the pressure signal was identified, the phase-path records showed a group of sinusoidal oscillations with periods between 10-15 minutes.

Figure 2.27 shows the delayed and summed pressure trace for  $230^\circ$  azimuth above the filtered phase-path doppler signal.

Several days of phase-path sounder records before and after the arrival were bandpass-filtered (Figure 2.28). It must be noted that the signal at 2300Z on 24 August 1968 has the largest amplitude.

It is suggested here that the observed phase-path variation is the result of vertical changes, in the reflecting region of the ionosphere, due to the passage of the atmospheric gravity wave generated by the nuclear event at the South Pacific test site. The estimated displacement of the ionization was of the order of 5 km peak to trough.

## 2.3 Background Field

### 2.3.1 Ionospheric Background Motions - Relevance to Noise Field Phenomena

This section is directed to the study of ionospheric motions with time scales of the order of minutes. The observations have been made with phase-path doppler sounders which respond to vertical motions of ionization.

The importance of this study rests on the information that can be obtained about the background of ionospheric motions with respect to the driving mechanism and to the variations of the structure. From the theoretical point of view it is interesting because it provides the orders of magnitude of



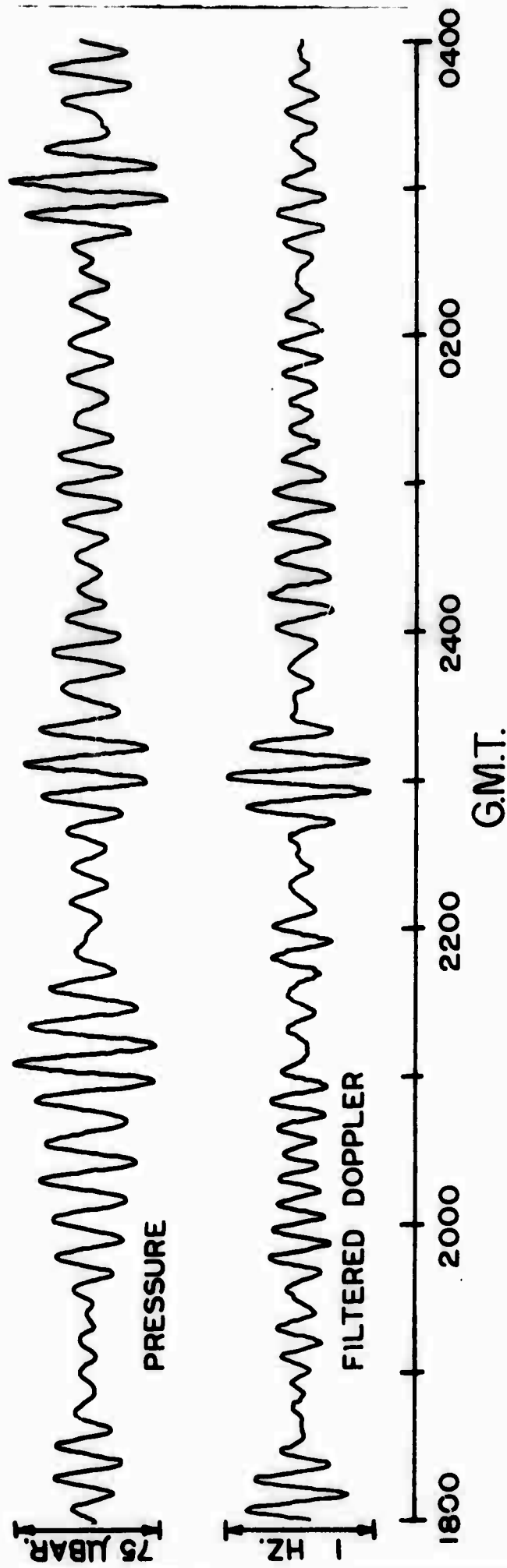


FIG. 2.27 Beamformed pressure trace for 230° azimuth is plotted above filtered doppler record. The data corresponds to the French test on August 24, 1968.



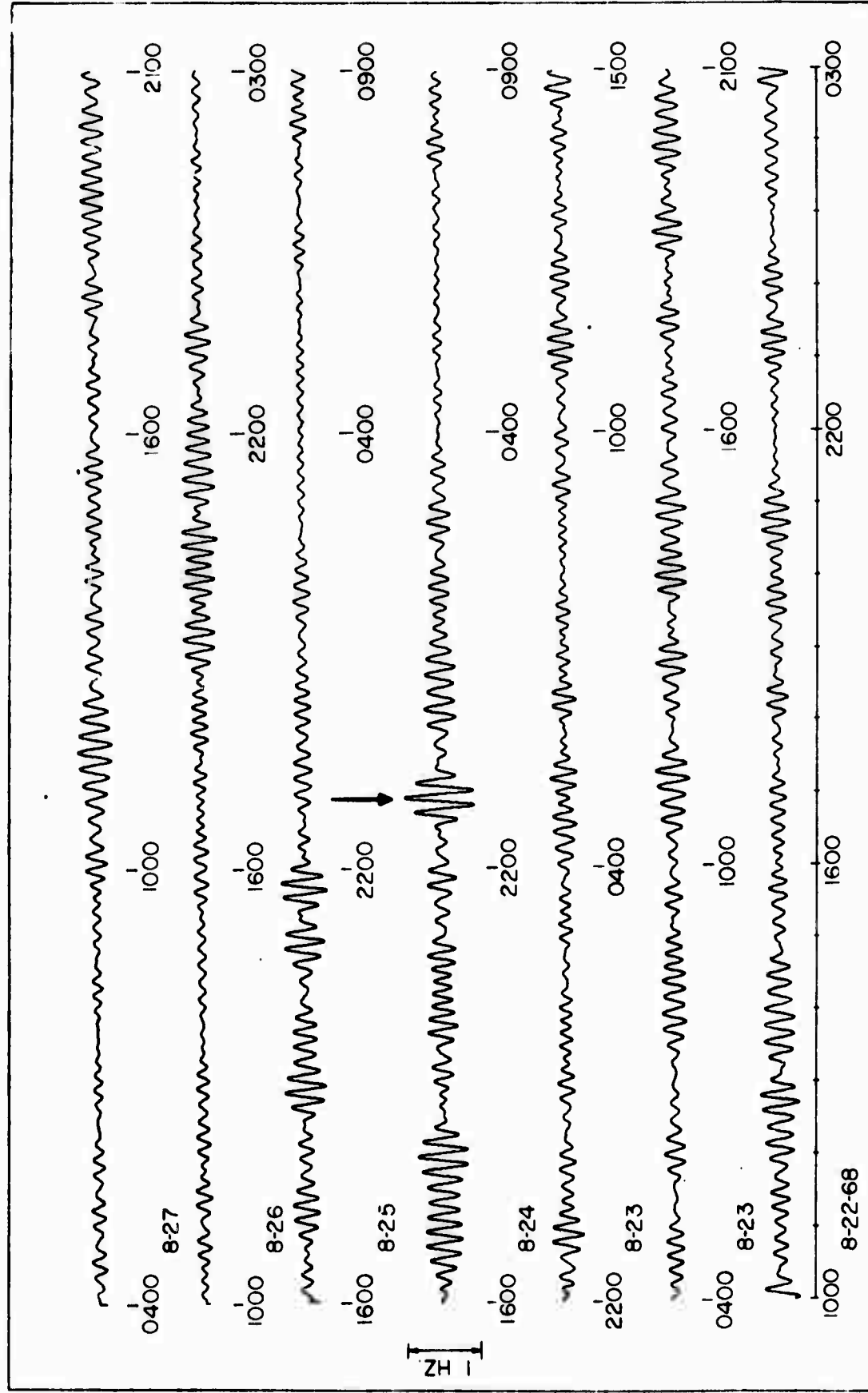


FIG. 2.28 Plot showing several days of doppler records. The central record contains the arrival from the 8/24/68 (arrow). Note that this signal is the largest signal occurring during the 4 days shown in the figure.



## Teledyne Isotopes

the motions characterizing the background. The variation of the structure is an important clue to the arrival of atmospheric waves originating in nuclear detonations. From the point of view of communications this knowledge is necessary in applications such as over-the-horizon radars which depend on reflections from the ionosphere for the detection of missiles and aircraft.

Although several mechanisms may contribute to the motion of electrons in the ionosphere, two broad categories can be distinguished. a) Those caused by electrodynamic forces such as hydromagnetic waves, plasma instabilities, and electric fields. b) Those caused by motion of the neutral (un-ionized) component of the atmosphere (winds, turbulence, gravity waves), and coupled to electron density perturbations.

Two types of observations are discussed in this section. One type requires a hydromagnetic wave interpretation and thus belongs to the first category. The other type can be explained as interaction of atmospheric gravity waves with ionization and therefore it belongs to the second category.

### Mid-latitude ionospheric characteristics

The ionosphere extends upwards from 60 to 500 km. The levels below 90 km constitute the ionospheric D region. Between 90 km and 130 km is the E region where a well-defined layer of ionization is formed during normal daytime conditions. Above 130 km two layers, F1 and F2, are formed during daytime hours; this region is called the F region. The ionization density normally reaches a peak in the F region, at heights of 250 to 500 km. These heights are of course average heights since they vary with solar time and geomagnetic location. The ionization of the D, E and F layers is produced mainly by the UV radiation from the sun and disappears at sunset due to rapid



## Teledyne Isotopes

recombination rates. The F2 layer is produced partly by photoionization and partly by collision of neutral particles with energetic particles. The recombination rates are slow and consequently this layer is present through the night.

The composition of the ionosphere varies from layer to layer. Thus the D region is characterized by dominant ions of  $N_2$  and  $O_2$ . At E region heights  $O_2^+$  ions appear to be dominant; although the abundance of  $N_2$  is about the same as  $O_2$  the high recombination rate of  $N_2^+$  removes the  $N_2^+$  ions as rapidly as they are produced. The dominant ion at F region levels below 600 km is  $O^+$ , although a very small fraction of the ions present are  $O_2^+$  and  $N_2^+$  ions.

In the D and E regions collisions of electrons with neutral particles predominate. This is not necessarily the case in the F region, where for most purposes, the important collisions are between ions and neutral particles.

### Mid-latitude geomagnetic fluctuations

Rapid magnetic variations, with time scales varying from a few tenths of a second to many hours, and amplitude scales varying from a few hundredths to a few tens of gammas, are observed. The larger amplitudes correspond to the longer period fluctuations. Geomagnetic micropulsations are classified according to their character and frequency content (Jacobs et al., 1964). From experimental observations two main classes are recognized: those with a regular and continuous character, and those with an irregular and impulsive pattern. They are divided in sub-groups according to their periods. The regular class was divided into five period ranges and designated Pc1 through Pc5. The irregular class was divided into two period ranges and given the designation Pi1 and Pi2.



## Teledyne Isotopes

<u>Notation</u>	<u>Period Range, seconds</u>
Pc1	0.2 to 5
Pc2	5 to 10
Pc3	10 to 45
Pc4	45 to 150
Pc5	150 to 600
Pi1	1 to 40
Pi2	40 to 150

It must be pointed out that this classification is a guide rather than a clear-cut distinction.

Geomagnetic micropulsations are measured with a variety of instruments: nuclear resonance magnetometers, fluxgate magnetometers, induction coils, earth-current meters.

Each type of micropulsation shows different diurnal and seasonal variations, thus Pc activity shows a maximum near noontime and a minimum during winter months. Pi activity has a maximum at midnight hours but does not show a definite seasonal variation, although some suggestions of an equinox maxima have been made.

### Previous observations of ionospheric motions

In order to put the studies carried out under this contract in proper perspective, it is necessary to review briefly the previous observations of ionospheric disturbances.

As early as 1950, Munro in Australia considered that travelling disturbances in the ionosphere were associated with disturbances in the neutral atmosphere. Martyn (1950) interpreted the wave-like motions observed by Munro (1950) as produced by internal atmospheric gravity waves that provided continuously rotating cells, of neutral gas, in the F region: the cells were



## Teledyne Isotopes

moved horizontally by a wind motion. This idea was however abandoned because of the direction of motion required by the model. In the following years other mechanisms involving the effects of dominant electric fields or hydromagnetic waves were proposed (Martyn, 1955; Dungey, 1955).

By the end of the 1950's several causes of ionospheric irregularities were suggested. Some of the principal ones were: variability in ionization rates, mixing by air currents, recombination and diffusion by winds, hydromagnetic waves, turbulence, gravity waves. Although it was recognized that fluid motions in the atmosphere played an important role, the detailed nature of this role was a matter of considerable controversy.

In 1957 at the URSI General Assembly it was decided that a joint study by a group of ionospheric physicists and fluid dynamists would prove worthwhile. A symposium was then organized in which several driving mechanisms were discussed. Some of the conclusions of the symposium were (Bolgiano, 1959):

- 1) Turbulence is a common occurrence in the ionosphere, at least to an altitude of 100 km. This was established from the rate of diffusion of visible meteor trails, which is several orders of magnitude higher than that attributable to molecular diffusion alone.
- 2) The large-scale anisotropic motions are not adequately described by the theory of turbulence. The bulk of the energy probably resides in motions more properly classed as semi-coherent winds: random gravity waves, thermal winds. The intensity of fully developed turbulence may be no more than 1 percent of the total energy.
- 3) The earth's magnetic field has negligible direct effect on turbulence but may affect it indirectly via the dynamo action.
- 4) Hydromagnetic effects probably account for a number of ionospheric phenomena.



## Teledyne Isotopes

In 1960 Hines published a paper in which he explained the wind structures revealed by the meteor trail observations of Liller and Whipple (1954) and Greenhow and Neufeld (1959) in terms of internal atmospheric gravity waves; he further suggested that observations of drift of radio diffraction patterns produced by moving irregularities, and travelling ionospheric disturbances could also be explained by these waves. Dieminger and Kohl (1962) suggested that the 500 m/sec velocity found in their observations were sound waves travelling in the ionosphere, where the speed of sound is higher. Hines (1964) pointed out that internal gravity waves can account for a wide variety of mid-latitude irregularities, suggesting that the observed propagation to long distances without attenuation was probably due to ducting. Wickersham (1965) interpreted the natural travelling ionospheric disturbances, observed by Munro (1958) and others, as ducted acoustic-gravity waves. The ionospheric effects associated with the Alaskan earthquake in 1964, observed by Davies and Baker (1965), were explained by Row (1967) as gravity waves. Georges (1967) examined single-frequency vertical incidence CW phase-path doppler data from Boulder with regard to spectral characteristics; he suggests that the longer-period frequency fluctuations may be due to the interaction of superimposed gravity waves with the ionosphere and that the diurnal variation of the dominant period is an observational selection due to the change in radio reflection height. Titheridge (1968) interpreted his observations in terms of gravity waves, pointing out that the periods of the disturbances were near the period of thermobaric resonance. Klostermeyer (1969) suggested, from observations of atmospheric gravity waves in ionosonde records, that the source of the waves was in the troposphere. Herren and Montes (1970) have



## Teledyne Isotopes

explained their observation of a doppler signal connected with the high energy event of 24 August 1968 as a surface gravity wave mode. Thome and Rao (1969) concluded from their observations of TIDs over Puerto Rico, that the principal effect of the gravity wave motion of the neutral gas is to impart its motion, parallel to the earth's magnetic field, to the ions through collisional interaction, and that as a result of the interplay of a number of factors, certain Fourier components of the permitted gravity wave spectrum are more effective than others in producing the disturbances.

### Previous observations of phase-path variations associated with geomagnetic activity

Rishbeth and Garriot (1964) discussed two possible mechanisms for the association of phase-path fluctuations and geomagnetic micropulsations found by Chan et al. (1962). The first mechanism consists of a hydromagnetic wave travelling along the geomagnetic field lines, which are distorted into a sinusoidal form; the wavelengths of the displacements are greater than the vertical extent of the ionosphere. The second mechanism considers that the micropulsations are due to alternating electromotive forces generated by the dynamo action of the oscillations of the neutral gas. Unfortunately the ionospheric data of Chan was taken at oblique incidence including several hops of the HF propagation paths; also the distance between reflection points and magnetometers was greater than 1000 km and they could not distinguish between the two effects. Jacobs and Watanabe (1966) made a more detailed treatment of the alternating current model. They concluded that, on those occasions where doppler shifts of about 1 Hz corresponding to geomagnetic micropulsations with periods of 50 to 90 sec and magnitudes of 5 to 10 gammas, the micropulsations could not be generated by alternating ionospheric currents. Boyd and Duffus



## Teledyne Isotopes

(1969) designed an extensive experiment to observe ionospheric motions associated with geomagnetic micropulsations; unfortunately they failed to do any cross-spectral analyses of the records, thus phase and coherence information were not obtained by these workers, and their conclusion was that the two most likely mechanisms for the association of micropulsations and phase-path fluctuations were: (i) hydromagnetic waves and (ii) neutral-gas waves modulating ionospheric electrojets.

### Simultaneous observations of phase-path and magnetic variations

During the month of August 1968, as part of the atmospheric wave propagation program of Hudson Laboratories of Columbia University, a three-station 3-component array of magnetometers was operated in conjunction with a vertical incidence phase-path doppler sounder, and an array of twelve microbarographs described by Herron et al. (1969). The distribution of the stations is shown in Figure 2.1. The operation of the array continued during the month of September after the project was transferred to Teledyne Isotopes.

The frequency used in the doppler sounder was 4.824 MHz. The average reflection height for this frequency is of the order of 150 km during daytime hours and 200 km during nighttime hours. The transmitter was located at Sterling Forest, and the receiver at Dobbs Ferry, New York. The separation between these two locations was about 36 km; for a reflection height of 200 km the angle of incidence would be in the order of 5 degrees. For all practical purposes we could assume that the operation was at vertical incidence. The ground wave was conveniently eliminated by the orientation of the antennas and the shielding effect of the Ramapo Mountains which are located between the transmitting and receiving sites. The sampling rate was 10 seconds; the analog



## Teledyne Isotopes

signal was passed through a 10-second low pass RC filter prior to digitization to avoid aliasing effects.

Boyd and Duffus (1969) reported previous observations of this sort. However there were some unanswered questions related to the mechanism causing the coupling between the magnetic micropulsations and the phase-path changes. Having microbarographic data available as well as an array of magnetometers, we thought that these questions could be answered.

### Data analysis

During the period of recording we found 16 events (see Table 2.3) in which an almost peak-to-peak correlation between magnetometer and doppler data exists. Note that the times of occurrence are before or near local midnight. The results of the analyses of a typical signal are described in this report. Typical amplitudes are 1 Hz for the doppler signal and 1 to 2 gammas for the magnetic signals.

Power and cross-spectrum analyses using the method of Blackman and Tuckey (1959) were applied to the doppler and magnetic signals. The estimates of the power and cross spectral densities are given by the Fourier transform of the auto and cross-correlation functions respectively.

$$P_{11}(\omega) = \frac{1}{2\pi} \int_{-\infty}^{\infty} \rho_{11}(\tau) e^{-i\omega\tau} d\tau \quad (2.8)$$

$$P_{12}(\omega) = \frac{1}{2\pi} \int_{-\infty}^{\infty} \rho_{12}(\tau) e^{-i\omega\tau} d\tau = Co(\omega) + o \text{ Quad}(\omega) \quad (2.9)$$

where



Teledyne Isotopes

TABLE 2.3

Events Recorded

<u>Date</u>	<u>Universal Time</u>
8/27/68	0300 - 0600
8/27/68	0930 - 1000
8/31/68	0315 - 0415
9/ 2/68	0557 - 0657
9/ 3/68	0143 - 0243
9/ 4/68	0245 - 0345
9/ 5/68	0130 - 0215
9/17/68	0105 - 0230
9/17/68	0400 - 0422
9/18/68	0415 - 0515
9/18/68	2348 - 0010
9/19/68	0345 - 0355
9/21/68	0420 - 0540
9/26/68	0835 - 1035
9/27/68	0350 - 0580
9/29/68	0100 - 0300



Teledyne Isotopes

$$\rho_{11}(\tau) = \lim_{T \rightarrow \infty} \frac{1}{T} \int_{-T/2}^{T/2} f_1(t) f_1(t+\tau) dt \quad (2.10)$$

$$\rho_{12}(\tau) = \lim_{T \rightarrow \infty} \frac{1}{T} \int_{-T/2}^{T/2} f_1(t) f_2(t+\tau) dt \quad (2.11)$$

and  $f_1(t)$  and  $f_2(t)$  are the two time series under analyses.

Prior to the power and cross-spectral analyses the data was passed through a pre-whitening filter which consisted of a simple derivative filter. The smoothed spectral estimates were obtained using a "hanning window" and 10% lags. All filters used in the process, including the electric filters of the data acquisition system, were restored.

The coherency estimates were found from

$$|\gamma(i\omega)| = \left\{ \frac{[\text{Co}(\omega)]^2 + [\text{Quad}(\omega)]^2}{P_{11}(\omega) \cdot P_{22}(\omega)} \right\}^{1/2} \quad (2.12)$$

where  $|\gamma(i\omega)|$  = magnitude of the complex coherency.

Another feature worthy of study is the phase relationship. The cross-spectral analyses give the phase information in the form

$$\Delta\theta(\omega) = \theta_2(\omega) - \theta_1(\omega) = \tan^{-1} \left\{ \frac{\text{Quad}(\omega)}{\text{Co}(\omega)} \right\} \quad (2.13)$$

where

$$\theta_1(\omega) = \text{phase of time series } f_1(t) \quad (2.14)$$

$$\theta_2(\omega) = \text{phase of time series } f_2(t) \quad (2.15)$$

In the cross-spectrum figures the names identifying the two time series under analysis are printed at the top of the figure. The starting and



## Teledyne Isotopes

ending times are written next. The coherence is plotted in a linear scale from 0 to 1. The phase is indicated by two square symbols joined by a vertical line; the length of the line is the 90% confidence limit for the phase angles. When no vertical line is drawn and only one square symbol appears the confidence limit has exceeded 180 degrees and the symbol is drawn at the value of the phase given by the analysis. The curves in the lower part of the figure represent the power spectrum of each time series. The power spectrum levels have been multiplied by the center frequency of the band in which the spectral estimate is calculated. The continuous curve corresponds to the time series whose identification name is listed first, and the curve with the crosses corresponds to the second time series. Each cross represents a frequency band.

A typical event is shown.

### Event of 21 September 1968

The records for the time interval 0320Z-0550Z, corresponding to the three magnetometers at Catskill and the phase-path doppler sounder, are shown in Figure 2.29. The records for Thornhurst and Lebanon are practically identical.

A group of pulsations starting at about 0420Z and lasting until 0540Z can be correlated in all the traces; this is better shown in Figure 2.30 which represents the same traces filtered with a Fourier band-pass filter (0.5 min - 3.5 min).

The power spectral results for three consecutive windows of three hours each indicated that at the time of the event, there is an increase in the energy density of the doppler fluctuations and of the geomagnetic micropulsations. This increase in the energy density is about an order of magnitude and



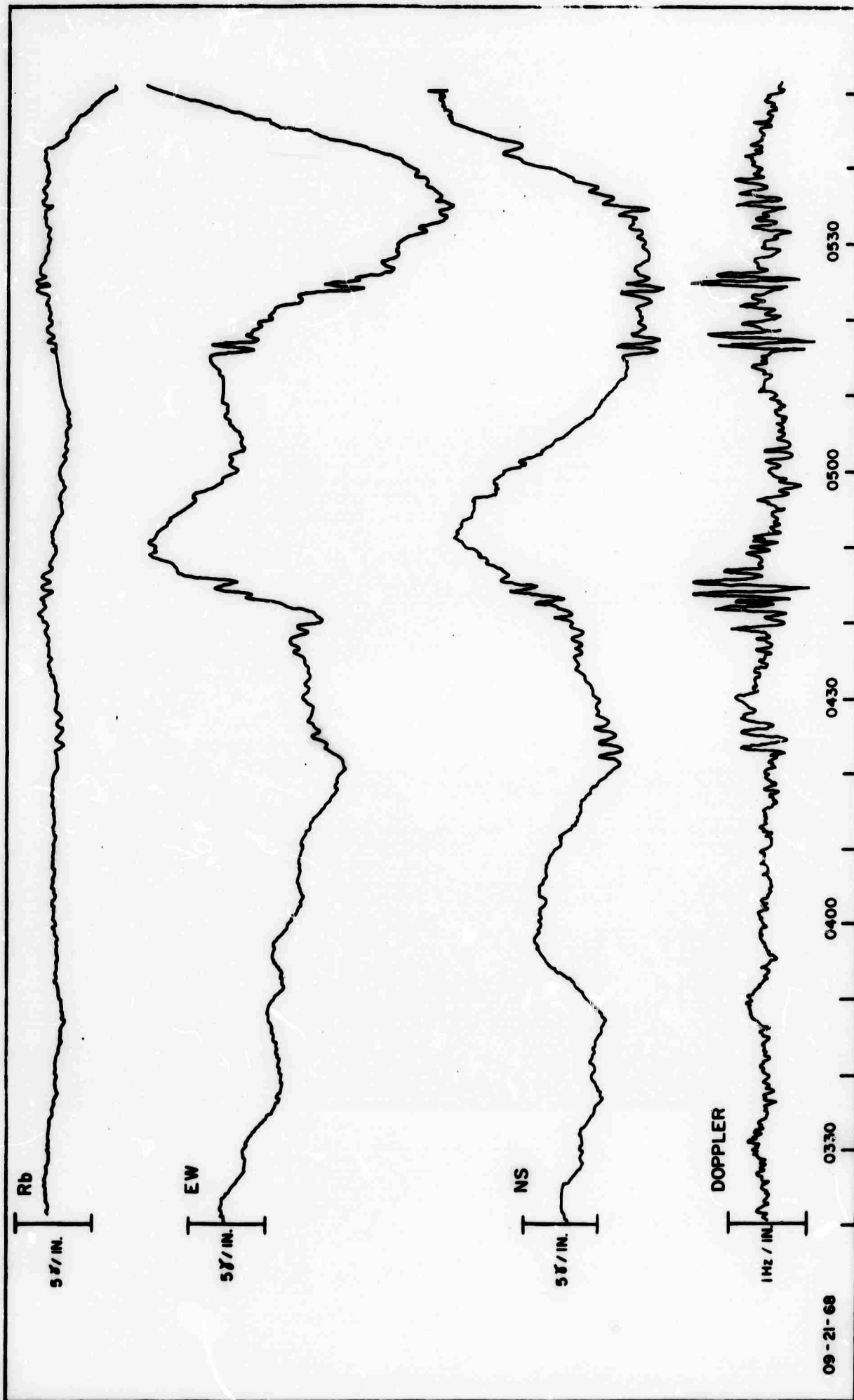


FIG. 2.29 Unfiltered traces corresponding to the magnetometers at Catskill and the phase-path sounder for the September 21, 1968 event.



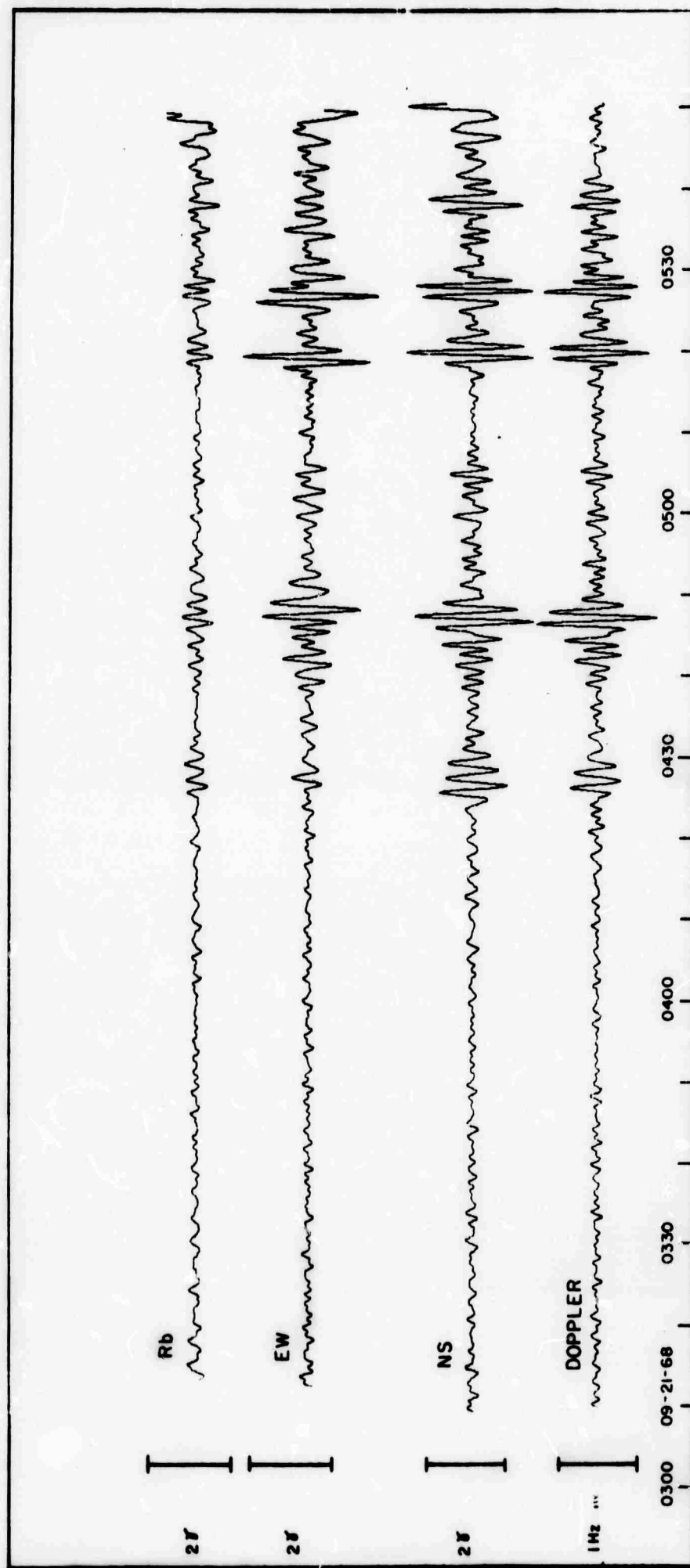


FIG. 2.30 Filtered traces corresponding to the magnetometers at Catskill and the phase-path sounder for the September 21, 1968 event. The filter band pass was 0.5 - 3.5 minutes.



## Teledyne Isotopes

it is mainly confined in the frequency band 0.008 Hz - 0.018 Hz and it drops after the event, Figure 2.31. Each trace has been shifted one unit in the vertical scale to avoid superposition.

Cross-spectral analyses have been applied to the pairs: NS Catskill - doppler; EW Catskill - doppler; EW Catskill - NS Catskill; Rb Catskill - doppler; NS Catskill - Rb Catskill; EW Catskill - EW Thornhurst; NS Catskill - NS Thornhurst; EW Catskill - Rb Catskill; EW Catskill - EW Lebanon; EW Lebanon - EW Thornhurst. The results are shown in Figures 2.32 through 2.41, and they will be discussed in terms of power, coherence, and phase separately.

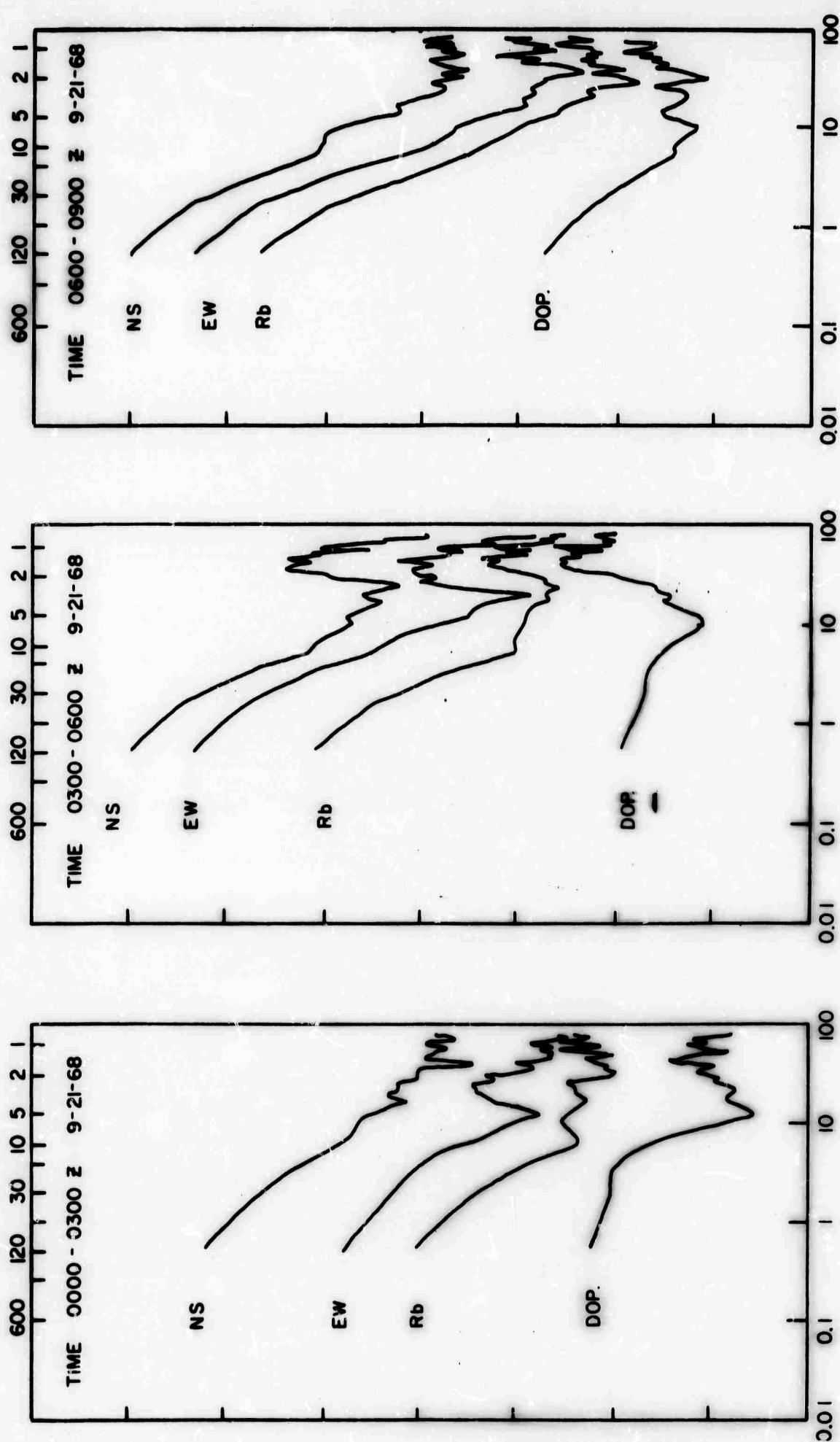
Coherence. The coherence between magnetic components, of the same polarization, at different stations is in general high throughout the frequency range covered by the cross-spectral analyses (Figures 2.37 and 2.40).

The pair NS Catskill - doppler showed high coherence ( $> 0.8$ ) in the frequency band corresponding to periods between 1 and 2 minutes (Figure 2.32). The coherence for the EW Catskill - doppler pair was rather low, except at the frequency corresponding to 1 minute period where it reaches a value of about 0.6 (Figure 2.33). The Rb Catskill - doppler pair followed closely the results for the NS Catskill - doppler pair (Figure 2.35). The same relationship holds between the magnetic components at the other two stations and the doppler. The EW-NS pairs at each station showed coherence values near 0.6 at periods of about 1 minute (Figure 2.34); this is the same type of relation that exists between the EW - doppler pairs. The coherence for the NS - Rb pair showed a peak between 1 and 2 minute period (Figure 2.36).

Phase. The phase relationships are as follows. The NS magnetic components lag the doppler signal in phase by about 140 degrees at a period



PERIOD (MIN.)



FREQUENCY (CYCLES / HOUR)

FIG. 2.31 Power spectra corresponding to three time windows on September 21, 1968. Each trace has been shifted one unit in the vertical axis to avoid superposition. Each vertical division is equal to 1 unit.



CH3 NS CATS X CH5 DOPPLER  
680921042000 TO 680921054000 GMT

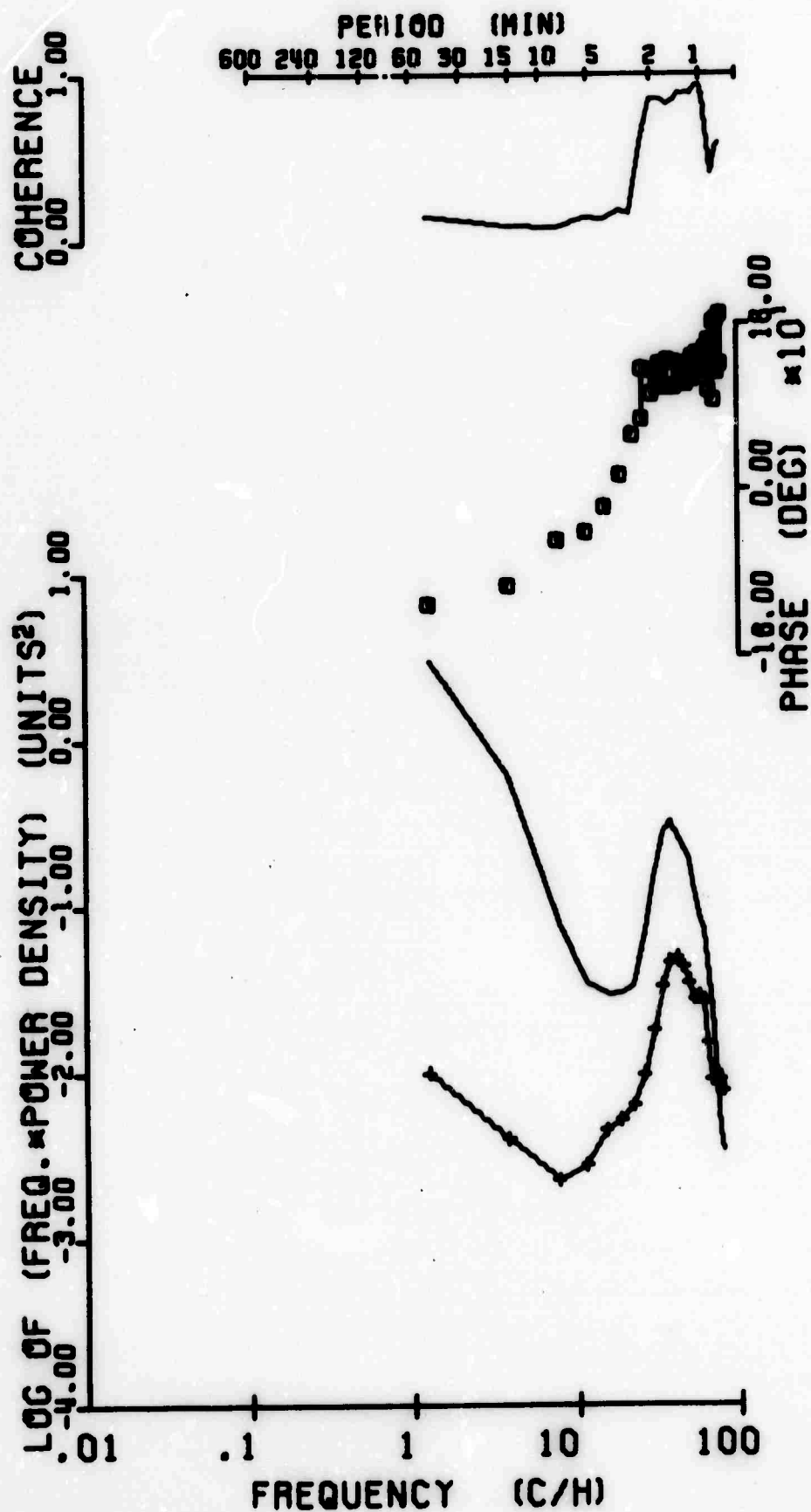


FIG. 2.32 Cross-spectrum between NS Catskill and phase-path doppler.



CH7 EW CATS X DOPPLER

680921042000 TO 680921054000 GMT

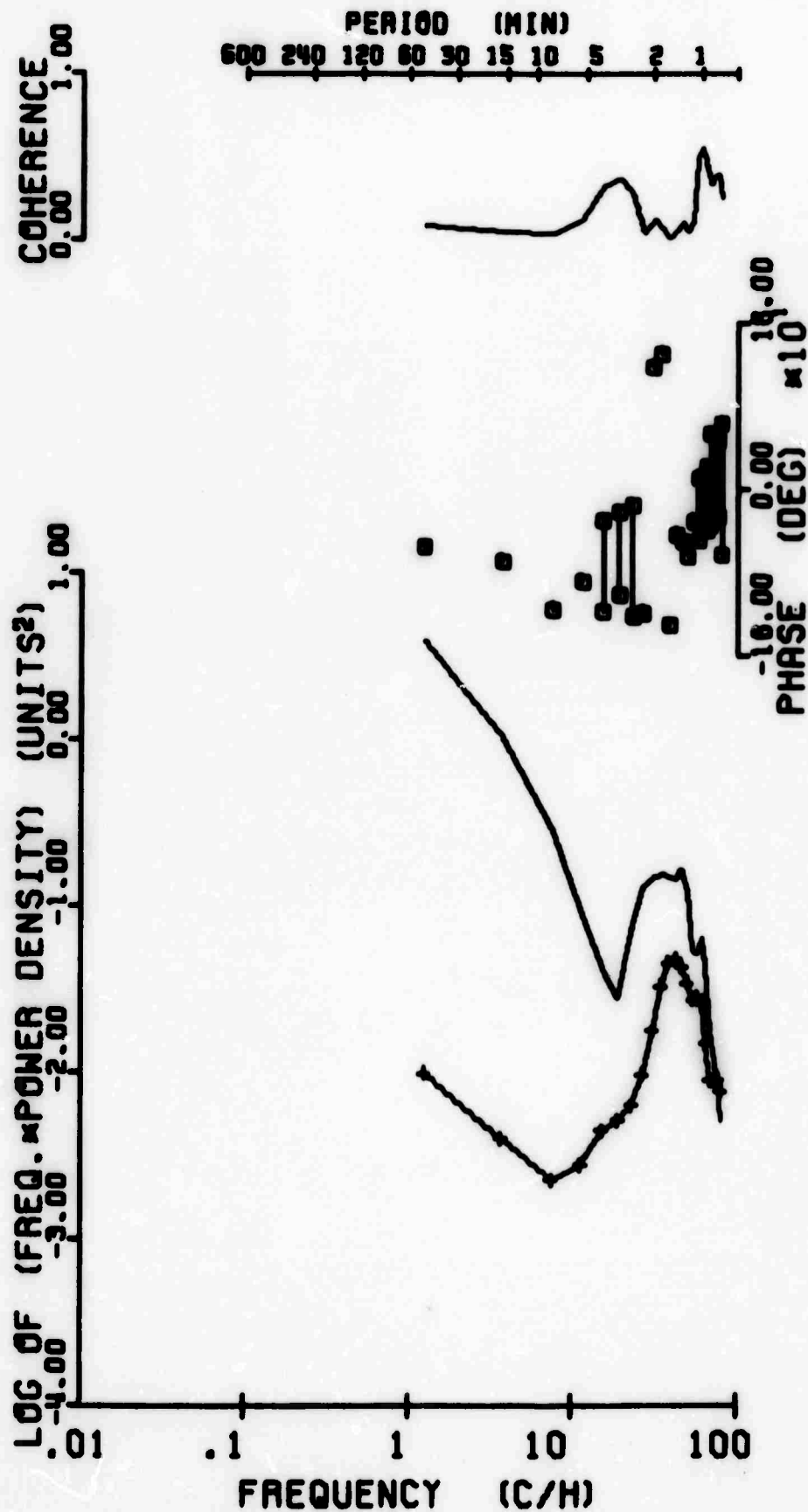


FIG. 2.33 Cross-spectrum between EW Catskill and phase-path doppler.



CH7 EW CATS X CH3 NS CATS  
680921042000 TO 690921054000 GMT

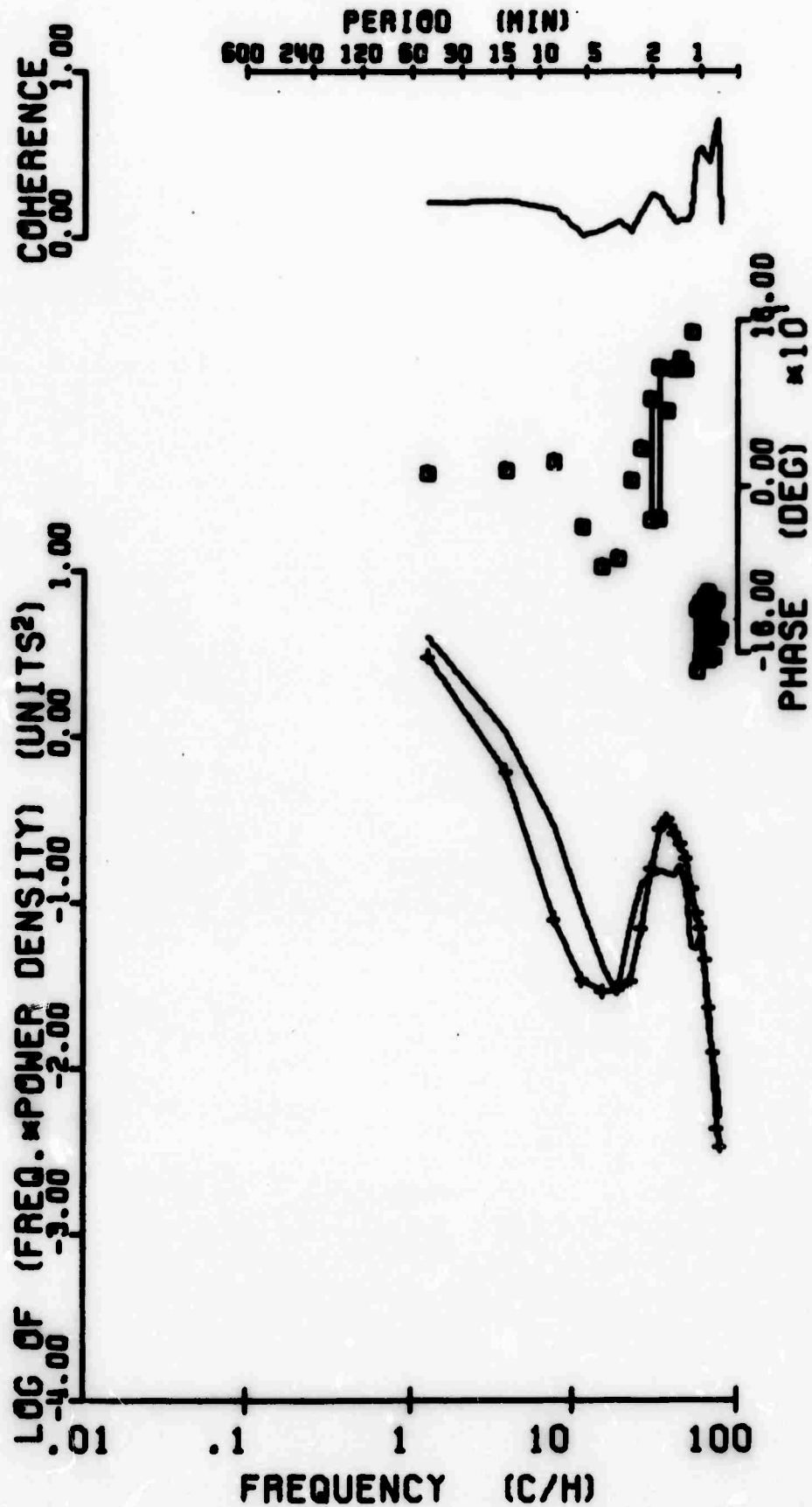


FIG. 2.34 Cross-spectrum between EW Catskill and NS Catskill.



CH11 RB CATS X CH5 DOPPLER  
680921042000 TO 680921054000 GMT

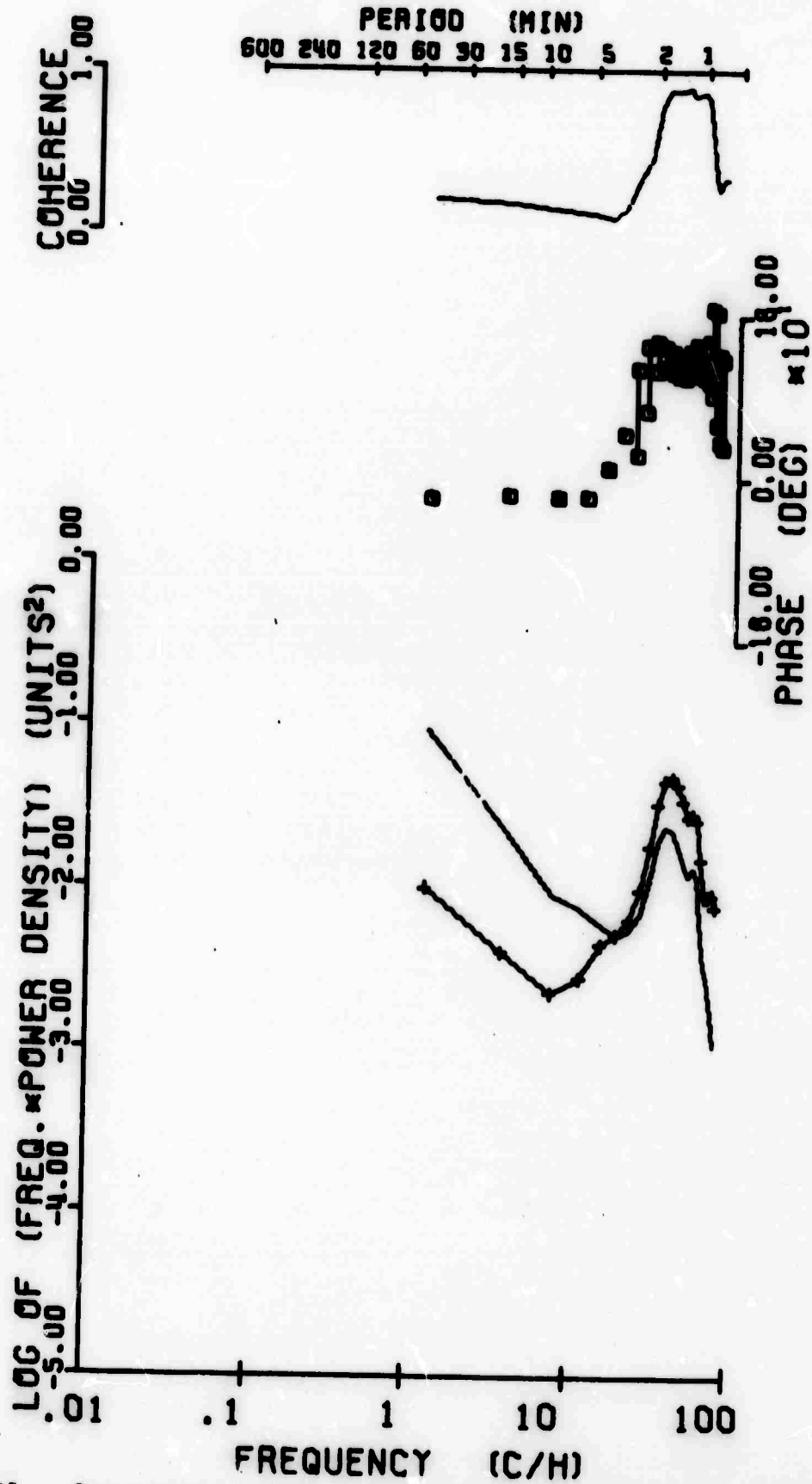


FIG. 2.35 Cross-spectrum between Rb Catskill and phase-path doppler.



CH3 NS CATS X CH11 RB CATS  
680921042000 TO 680921054000 GMT

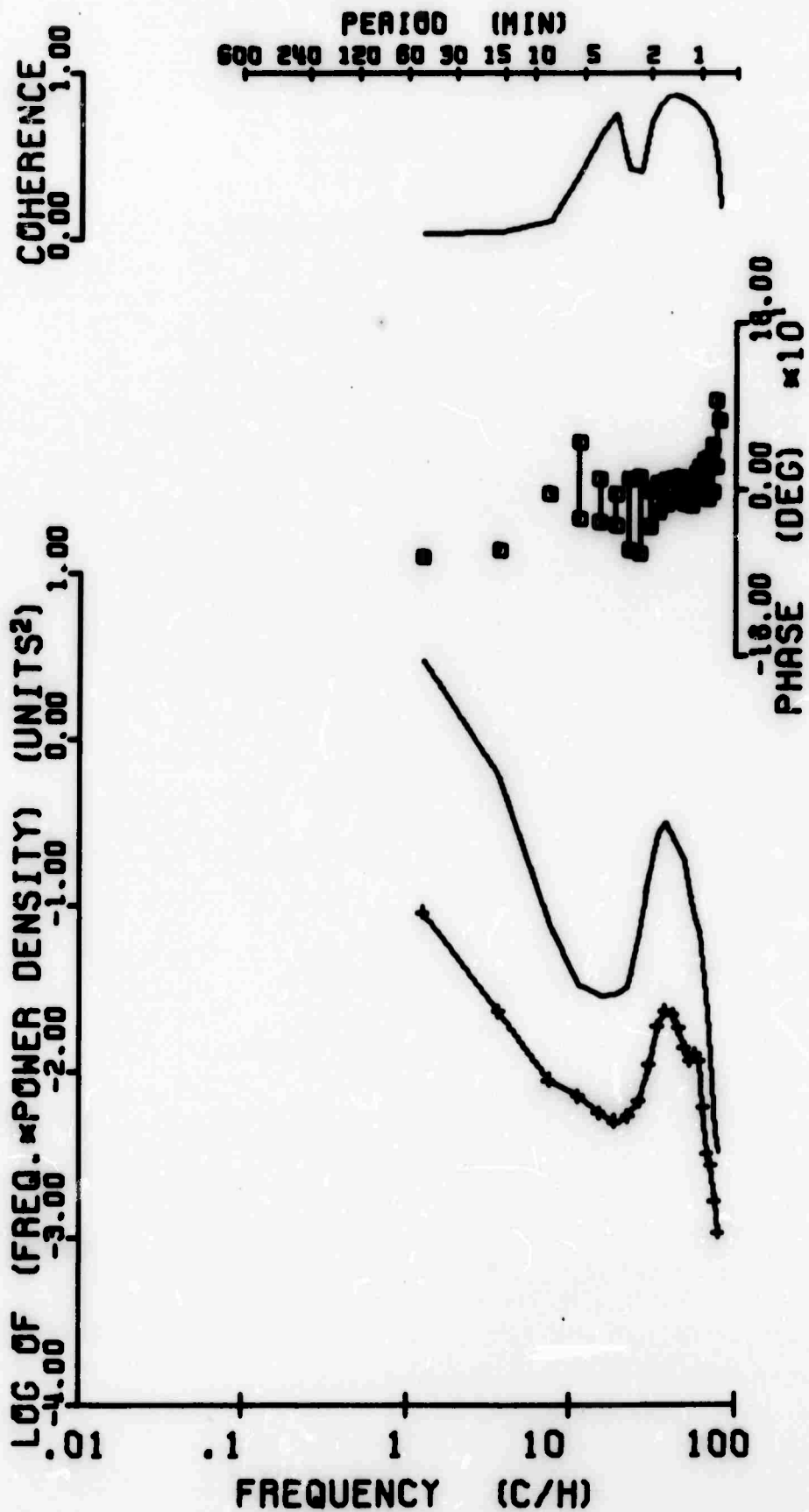


FIG. 2.36 Cross-spectrum between NS Catskill and Rb Catskill.



## Teledyne Isotopes

of one minute decreasing more or less uniformly to about 116 degrees at 2 minute period (Figure 2.32). Approximately the same relationship holds for the pair Rb - doppler (Figure 2.35). The phase between EW Catskill and doppler shows considerable scatter for periods at which the coherence is low, as one should expect in theoretical grounds, since coherence is a measure of the phase stability. However, for periods of about 1 minute the phase is relatively stable and its value is about -15 degrees, that is the EW components lead the doppler signal in phase by about 15 degrees at the 1 minute period band (Figure 2.33). Important phase relationships are those between magnetic components of different polarization at the same station; and between magnetic components of the same polarization at different stations. The first type of relation gives information about the orientation of the disturbance vector, in the plane containing the two components under analysis; and the second about time shift between stations and consequently can lead to the determination of apparent phase velocities. The EW components lead the NS and Rb components by 157 degrees and 140 degrees respectively at periods of 1 minute. The NS and Rb showed phase shifts of -20 degrees for 2 minute period and 11.7 degrees for 1 minute period indicating that in the first case the Rb lags the NS and in the second case the Rb leads the NS component. The phase velocities, estimated from the phase differences between magnetic components of the same polarization at different stations, are of the order of 100 km/sec  $\pm$  50 km/sec. The large uncertainty in the phase velocity is due to the small number of data points used in the computation of the cross-spectra (Goodman, 1957).



CH7 EW CATS X CH8 EW THO.

680921042000 TO 690921054000 GMT

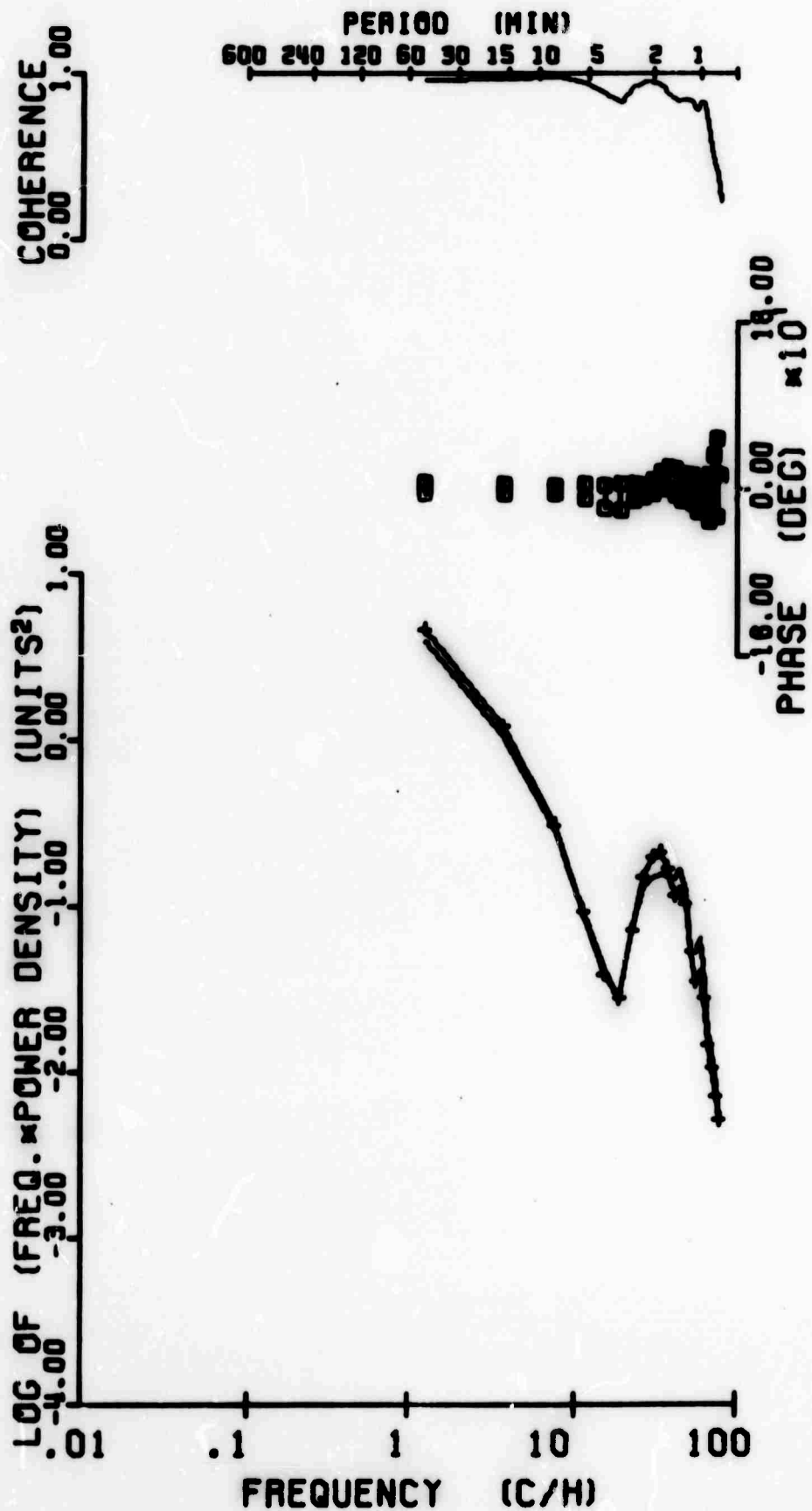


FIG. 2.37 Cross-spectrum between EW Catskill and EW Thornhurst.



CH3 NS CATS X CH4 NS TH0.  
680921042000 TO 680921054000 GMT

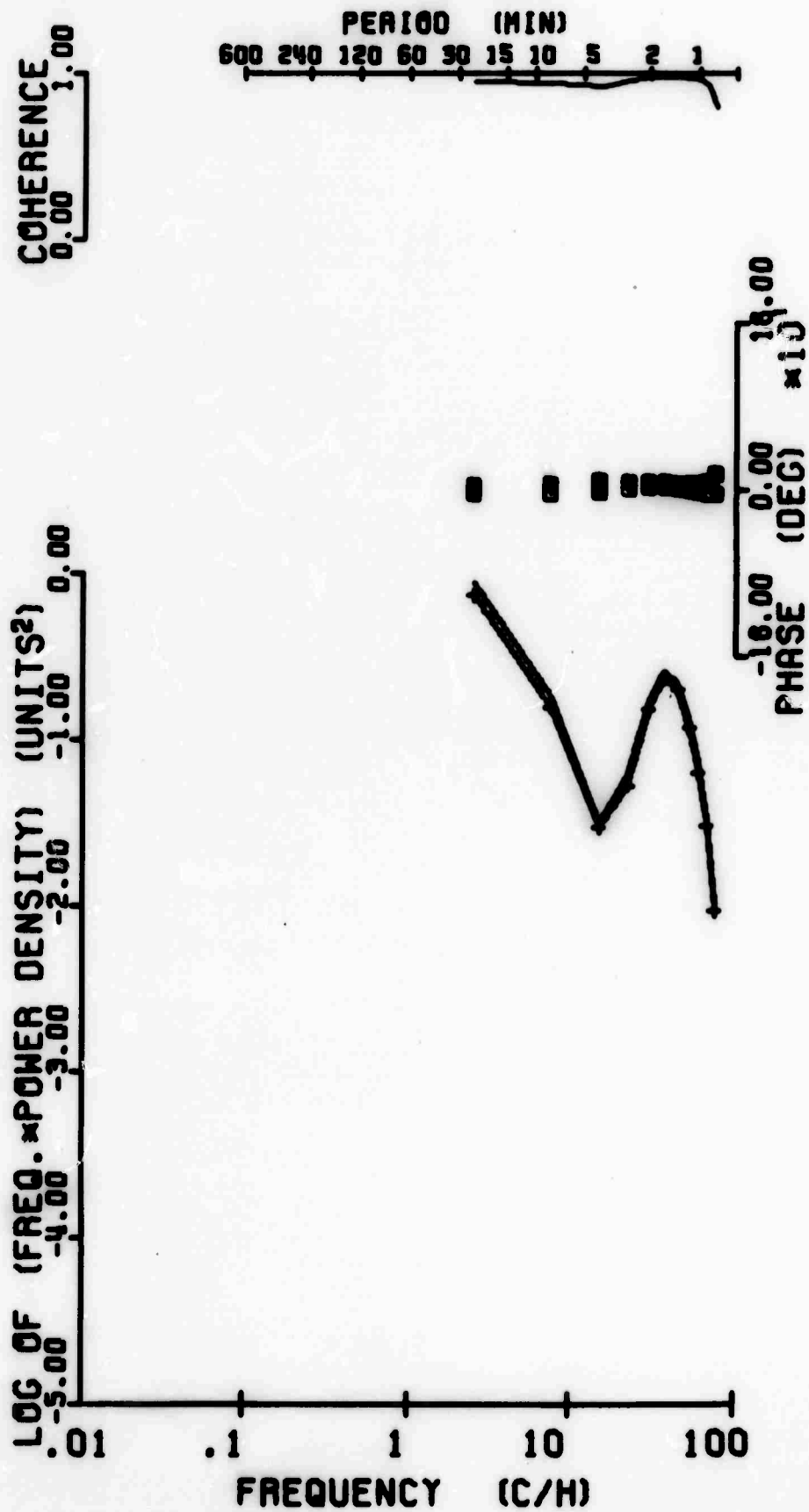


FIG. 2.38 Cross-spectrum between NS Catskill and NS Thornhurst.



CH7 EW CATS X CH11 RB CATS  
680921042000 TO 680921054000 GMT

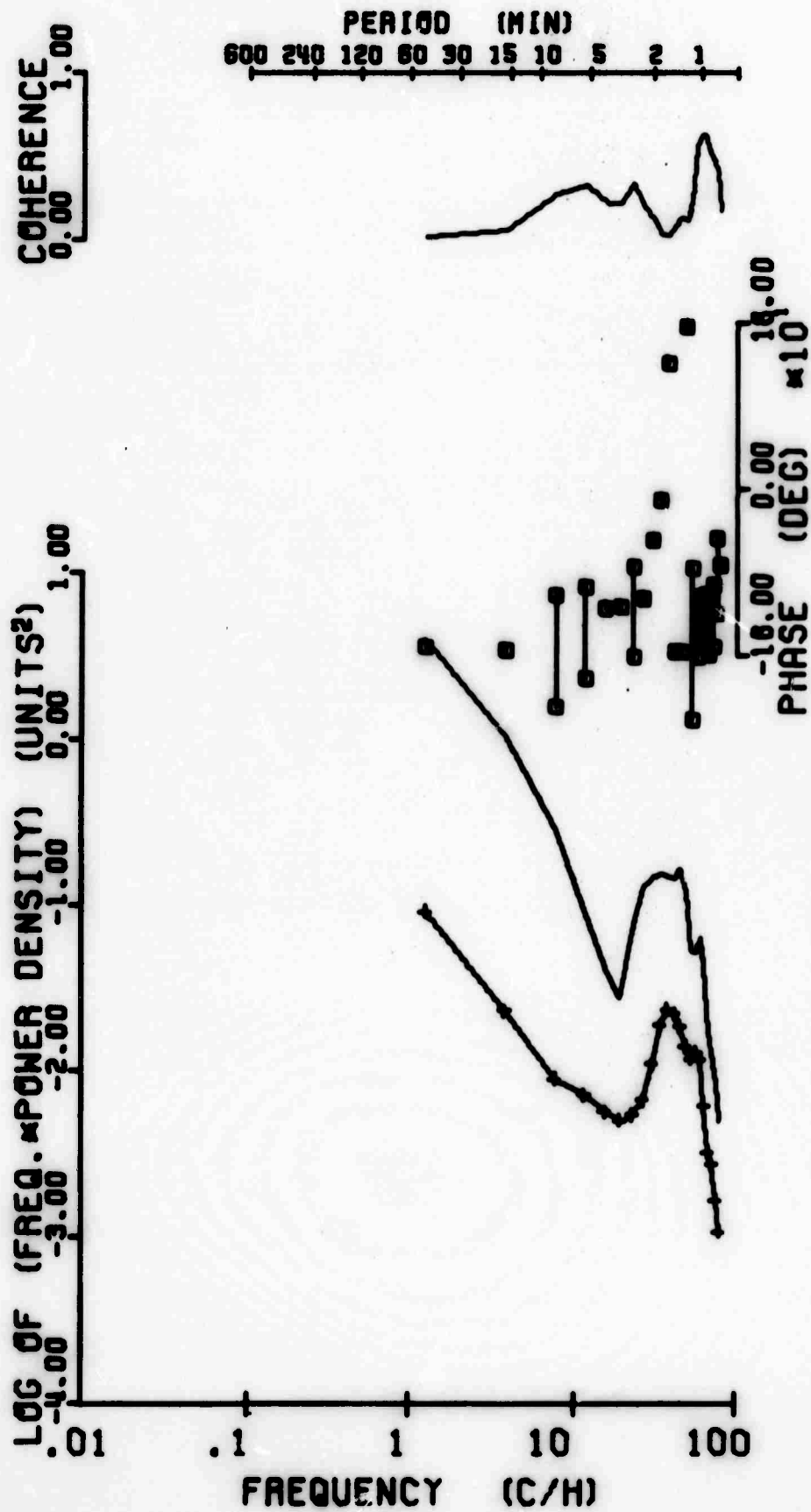


FIG. 2.39 Cross-spectrum between EWCatskill and RB Catskill.



CH7 EW CH15 X CH6 EW LEB.

680921042000 TO 690921054000 GMT

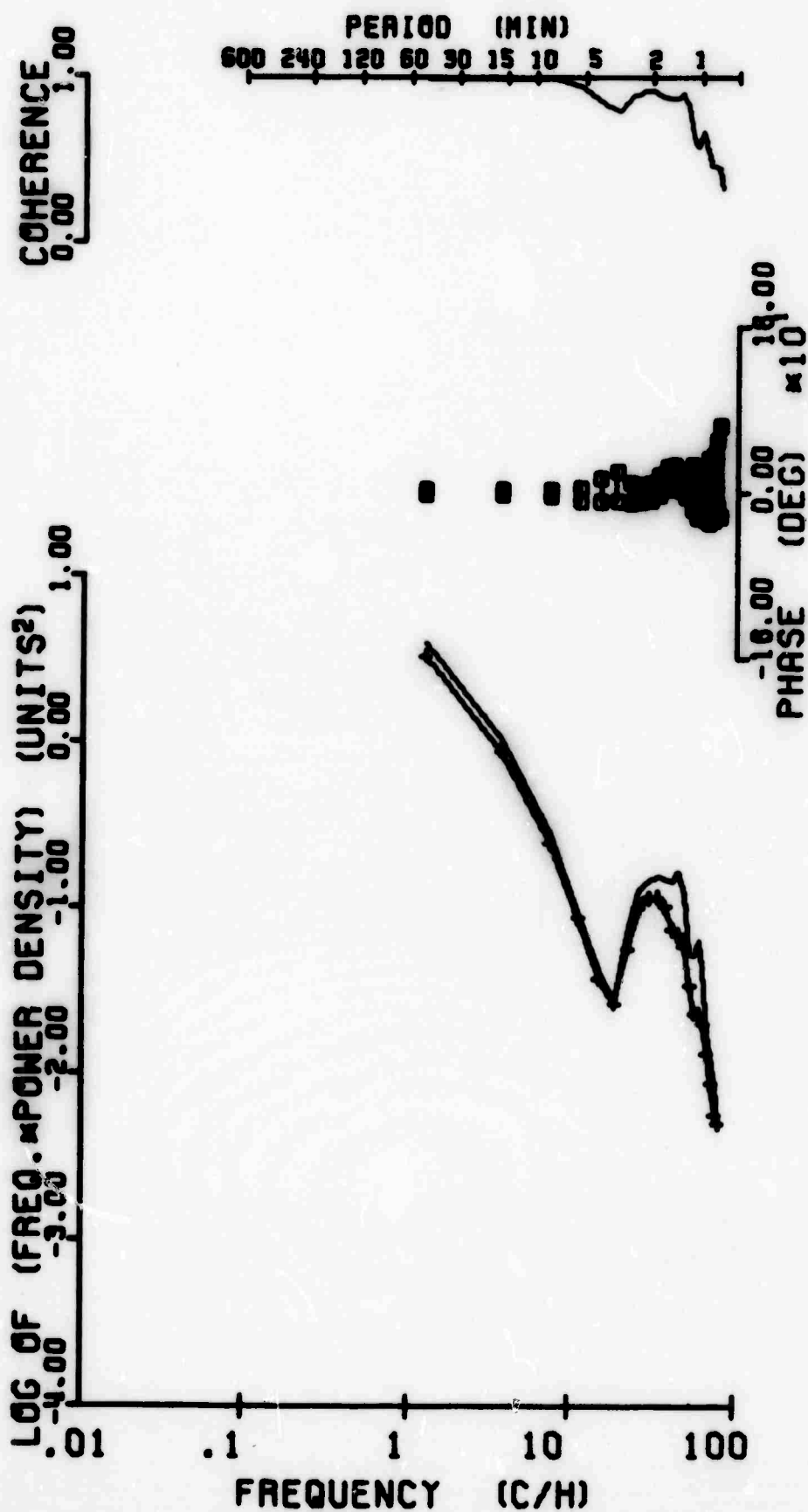


FIG. 2.40 Cross-spectrum between EW Catskill and EW Lebanon.



Interpretation of Results. The impulsive character, the frequency constant, and the times of occurrence of the events indicate that the micropulsations associated with the phase-path fluctuations belong to the Pi2 type (Jacobs et al., 1965; Christoffel and Linford, 1966; Saito and Matsushita, 1968).

The lack of infrasonic activity associated with the events and the high values of the phase velocities indicate the hydromagnetic character of this type of micropulsations in agreement with recent theoretical work (Kostoker, 1967; Saito and Matsushita, 1968).

The coherence results show that the disturbance is made up by the superposition of several modes of hydromagnetic waves. For example the event of September 21 has one mode centered at a frequency corresponding to a period of 1 minute which involves all three magnetic components; the other modes correspond to periods greater than 1 minute and affect only the NS and Rb components. On the other hand the event of September 18 showed modes centered at 1.14 minutes and 2.0 minutes respectively, in which the three magnetic components are affected; and one mode centered at 1.6 minutes affecting only the NS and Rb components. The magnitude of the coherence between different wave components is representative of the degree of polarization of the wave in the plane containing the pair of components (Born and Wolf, 1965); thus the mode centered at 1 minute is 50% polarized in the EW - NS plane and 98% polarized in the NS - Rb plane; similarly the modes centered at 1.14 minute and 2.0 minutes are 50% polarized in the EW - NS plane and about 70% in the NS - Rb plane. The modes not affecting the EW have degrees of polarization of about 80%.



## Teledyne Isotopes

The amplitudes of the Rb fluctuations in both events are smaller than those of the EW and NS components. This fact together with the high coherence between the NS and Rb signals suggest that the Rb disturbance is produced mostly by induction of the NS signal on the ground. If this interpretation is granted, one can postulate that the magnetic perturbations are due to transverse hydromagnetic modes, of waves propagating along the field lines.

A simple quantitative interpretation can be obtained from the equations relating the fluid velocity and the magnetic field disturbance of a transverse wave in an incompressible fluid of infinite conductivity. Following Alfvén and Fälthammar (1963), consider the geometry of Figure 2.41 and the MKS equations

$$\frac{\partial v_x}{\partial t} = \frac{B_o}{\mu \rho} \frac{\partial b_x}{\partial z} \quad (2.16)$$

and

$$\frac{\partial^2 b_x}{\partial t^2} = \frac{B_o^2}{\mu \rho} \frac{\partial^2 b_x}{\partial z^2} \quad (2.17)$$

where

- $v_x$  = velocity of the fluid
- $b_x$  = magnetic vector of the wave
- $B_o$  = Earth's magnetic field
- $\mu$  = magnetic permeability
- $\rho$  = plasma density



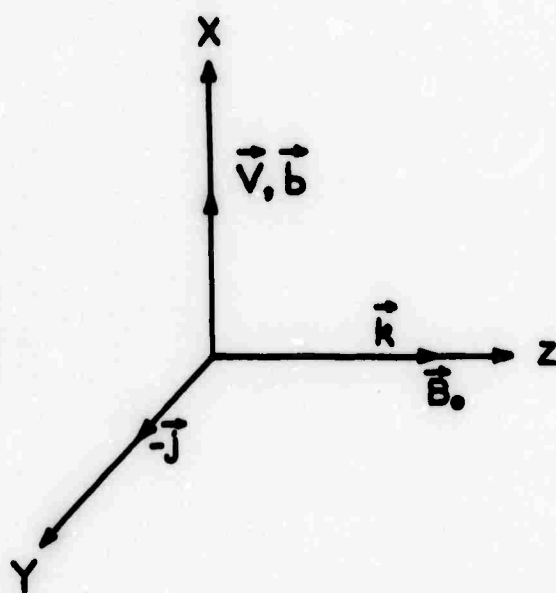


FIG. 2.41 Geometry for hydromagnetic transverse wave.



## Teledyne Isotopes

The solution of equation (2.17) has the form

$$b_x = b_o \sin \omega(t - z/V_a) \quad (2.18)$$

where

$b_o$  = magnitude of the magnetic vector

$V_a = B_o(\mu\rho)^{-1/2}$  is the phase velocity of the wave.

Substitution of equation (2.18) into equation (2.20) gives

$$v_x = -(\mu\rho)^{-1/2} b_o \sin \omega(t - z/V_a) \quad (2.19)$$

and

$$v_x = -b_x(\mu\rho)^{-1/2} \quad (2.20)$$

Rishbeth and Garriot (1964) have pointed out that at F region heights the ion neutral collision frequency is large enough to modify the phase velocity of the wave and suggested the use of a complex dispersion equation which modifies equation (2.20) to give

$$v_x = b_x \omega^{1/2} (\mu\rho v_{in})^{-1/2} e^{-j3\pi/4} \quad (2.21)$$

The inclusion of the collision frequency is the same as taking into account the conductivity of the medium. Dungey (1967) suggested that the density  $\rho$  can be replaced by the electron density  $N_e$  multiplied by the mass of the dominant ion  $M_i$ . In the F region of the ionosphere the dominant ions are  $O^+$ , and the electron density can be taken from the plasma frequency corresponding to the sounding frequency. Typical values for the parameters entering equation (2.21) are



# Teledyne Isotopes

$$\mu_0 = 4\pi \times 10^{-7} \text{ MKS}$$

$$m_i = 1.33 \times 10^{-26} \text{ MKS}$$

$$N_i = 2.85 \times 10^{11} \text{ electrons/m}^3$$

$$V_{in} = 1$$

and equation (2.21) projected on the vertical direction becomes

$$V_{ht} = V_x \cos I = 4.0 \times 10^{10} b_x T^{-1/2} e^{-j^{3\pi/4}} \cos I \quad (2.22)$$

taking  $T = 60 \text{ sec}$  and  $|b_x| \approx 2 \times 10^{-9}$  equation (2.22) gives

$$|V_{ht}| \approx 3 \text{ m/sec}$$

The velocity as observed on the phase path sounder data is given by

$$|V_{obs}| \approx \frac{c}{2f} \Delta f \quad (2.23)$$

using  $f = 5.0 \text{ MHz}$  and  $\Delta f \approx 0.5 \text{ Hz}$  one obtains  $|V_{obs}| \approx 15 \text{ m/sec}$ .

Equation (2.22) predicts a phase shift of 135 degrees between the velocity  $V_{ht}$  and the magnetic disturbance. The observed phase shift between the doppler and the NS, as was pointed out earlier, is of about 140 degrees, at a period of 1 minute, decreasing as the period increases. Alfven and Falthammar (1963) have showed that for simple transverse waves when the conductivity is taken into account the phase shift  $\phi$  is proportional to the inverse of the period

$$\phi \propto \frac{1}{T} \quad (2.24)$$



## Teledyne Isotopes

Using this relation one could explain the decrease in phase between the phase-path fluctuations and the NS component as the period of the disturbance increases.

The difference between predicted and observed amplitudes is probably due to attenuation of the magnetic disturbance when traversing the ionosphere at E region levels where the conductivity is higher.

Jacobs and Watanbe (1966) have pointed out that the association between phase-path variations and geomagnetic micropulsations cannot be due to ionospheric currents if the magnetic disturbance and the doppler shift have the same order of magnitude and periods of the order of 100 sec. This theoretical result favors our interpretation that the waves are of hydromagnetic origin. Boyd and Duffus (1969) suggested two general mechanisms for the association: i) hydromagnetic waves, ii) neutral gas waves; however they have not proposed any coupling mechanism which can explain the amplitude, phase and coherence between the parameters measured.

We can conclude then that:

- 1) The association between geomagnetic micropulsations and phase-path variations of the type investigated in this work can be explained by a superposition of various modes of transverse hydromagnetic waves, at least within an order of magnitude.
- 2) At least a significant portion of the ionospheric motions in this part of the spectrum have a hydromagnetic origin since this association is not a rare phenomenon.



Teledyne Isotopes

Multiple-frequency phase-path doppler observations

Observations using three sounding frequencies simultaneously, at one location, were carried out during the months of May and June, 1969.

A test for the coherence and frequency responses of the three systems was run by recording simultaneously in the three systems the same ionospheric reflected signal at the same location. Cross spectral analyses of the records indicated that for all practical purposes the instruments were identical.

The CW radio transmitters were located at Sterling Forest, N. Y. and the signals were received at Westwood, N.J. The distance from the transmitters to receivers was 30 km, and for practical purposes vertical incidence could be assumed. The transmitting and receiving antennas consisted of simple horizontally polarized half-wave dipoles. The frequencies used were 2.412 MHz, 4.824 MHz and 6.030 MHz; the average reflection heights for these frequencies were of the order of 130, 170 and 230 km respectively. The variations of the received frequencies as a function of time were recorded in digital form on an incremental digital magnetic tape. Since the periods of interest were of the order of minutes, a sampling rate of 10 seconds was considered convenient. As before, a low pass electronic filter was used to minimize aliasing effects. Data were recorded mainly during part of the month of June, although some data using two frequencies were collected in May. In some nights the critical frequency of the ionosphere, that is, the maximum plasma frequency, was smaller than 6 MHz for several hours, and consequently there were no reflections from 6.03 MHz during these time intervals; the usable data for these nights consisted only of two frequencies.



Since in this experiment one important parameter was the reflection height, the heights for the three sounding frequencies were obtained from regular ionograms. The relationship between true height of reflection and virtual height as obtained from ionograms is described next.

Relationship between virtual height and true height

Ionospheric heights of reflection as a function of frequency are routinely obtained at a national network using ionosondes. The ionosonde data is in the form of ionograms which are records of "virtual height" versus sounding frequency. The virtual height  $h'$  is the height at which a radio pulse would be reflected if it would travel at the speed of light in free space, at all times during its way to the ionosphere and back.

$$h' = \frac{1}{2} ct \quad (2.25)$$

where  $c$  is the speed of light in free space and  $t$  the time it takes the pulse to go to the ionosphere and return after reflection. However since the velocity of the pulse is the group velocity  $U$

$$h' = c \int_0^{h_r} \frac{dh}{U} = \int_0^{h_r} \mu' dh \quad (2.26)$$

where  $h_r$  is the true reflection height, and  $\mu$  is the group refractive index. Equation (2.26) can be inverted analytically using Abel's integral equation, when certain assumptions such as the absence of magnetic field and electron collisions, are made about the properties of the media (Davies, 1969).

$$h(f_v) = \frac{2}{\pi} \int_0^{f_v} \frac{h'(f) df}{\sqrt{f_v^2 - f^2}} \quad (2.27)$$



For this work the magnetic field and electron collisions were taken into account and a numerical true height analyses (Titheridge, 1967) was used. The need for the true height analysis becomes apparent if one looks at Figure 2.42 which shows a typical ionogram and the corresponding true height analysis.

Ionograms for Hanover, N.H. were made available to us by Prof. M.G. Morgan of the Radio Physics Laboratory of Dartmouth College. The heights of reflection for each power spectrum were obtained by averaging the heights of hourly ionograms.

#### Computation of $N(z)$

The distribution of the Väisälä frequency  $N(z)$  with height was obtained from Tolstoy (1967). The temperature distribution was computed using the empirical formulas from the U.S. Standard Atmosphere Supplements, 1966.

$$T(z) = T_{\infty} - (T_{\infty} - T_{120}) \cdot \exp [-S(z - 120)] \quad (2.28)$$

where

$$S = 0.0291 \cdot \exp (-q^2/2) \quad (2.29)$$

and

$$q = (T_{\infty} - 800) [750 + 1.722 \times 10^{-4} \times (T_{\infty} - 800)^2]^{-1} \quad (2.30)$$

$T_{120}$  = temperature at 120 km

$T_{\infty}$  = temperature at the top of the ionosphere

The values used for  $T_{120}$  and  $T_{\infty}$  were 327°K and 200°K respectively which are the suggested values for Summer time.



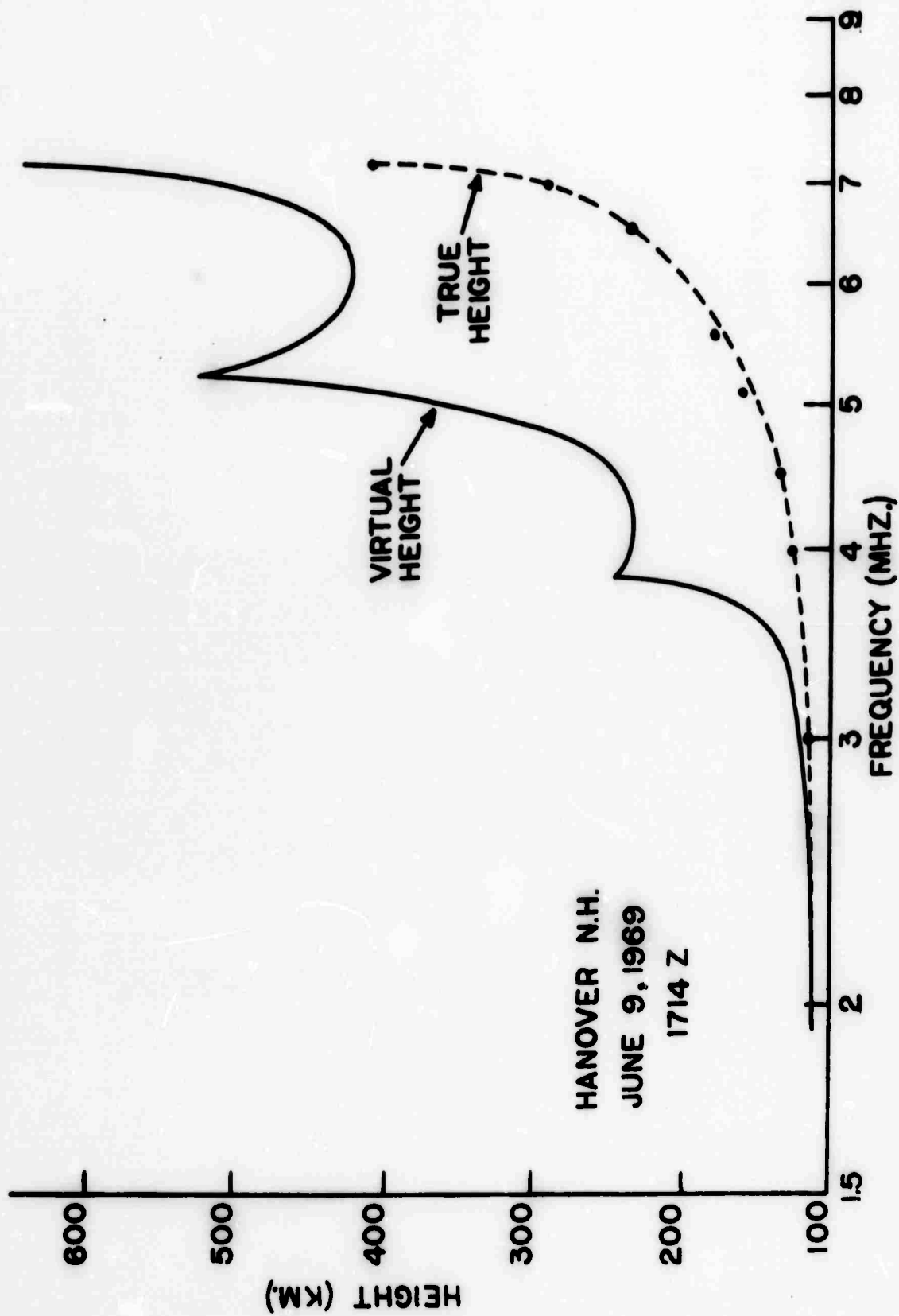


FIG. 2.42 Typical ionogram showing the true height analysis.



### Preliminary Results

Power spectra of the phase-path sounder records showed systematic peaks and slope breaks, which appear to shift towards longer periods for greater reflection heights (larger sounding frequencies). Examples of this kind of behavior are illustrated in Figures 2.43 and 2.44).

The distribution of the period corresponding to the main spectral peak with height (sounding frequency) shows a pattern that resembles the distribution of the Väisälä frequency for an adiabatic atmosphere (Fig. 2.45). This work is continuing in the present contract and new results will be reported at a later date.

### Conclusions

The main conclusions of this section are:

- 1) The geomagnetic micropulsations associated with phase-path variations in the period range 0.5 minutes to 3 minutes are of the Pi2 type and consist of the superposition of various modes of transverse hydro-magnetic waves. The estimated phase velocities are in agreement with values of the Alfvén velocity at ionospheric heights. These hydro-magnetic waves modulate the ionospheric plasma producing the observed phase-path variations.
- 2) The spectral peaks of phase-path doppler records occurring at periods greater than 5 minutes probably correspond to internal gravity wave activity.
- 3) Inclusion of viscosity into the theory of internal gravity wave propagation will allow a quantitative interpretation of the phase-path variation spectra, with the possibility of deriving the parameters of the neutral gas structure at ionospheric levels.



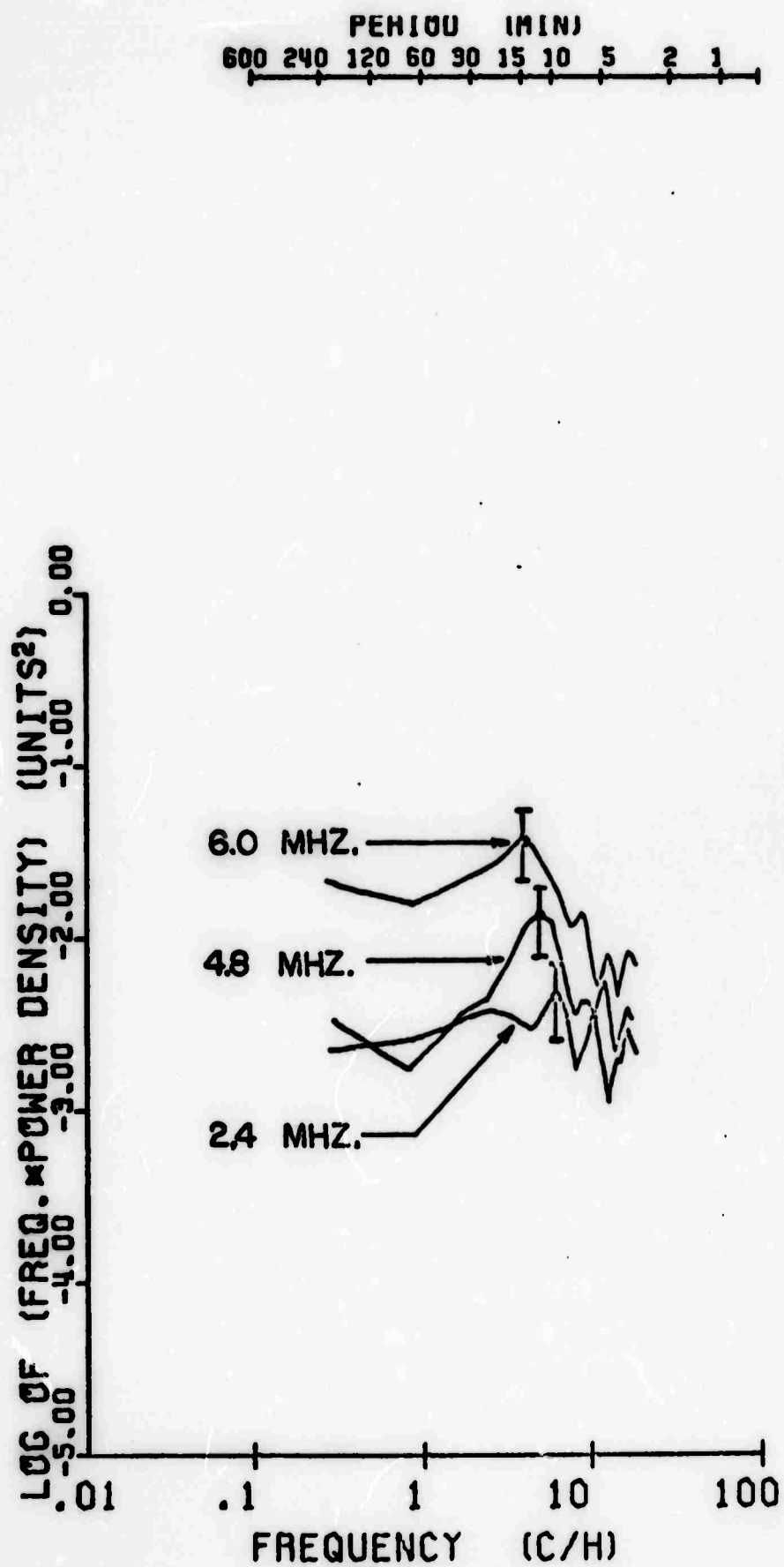


FIG. 2.43 Power spectra of phase-path doppler records for 6.030, 4.824 and 2.412 MHz corresponding to the time interval 1700 - 2300 G.M.T. on June 9, 1969.



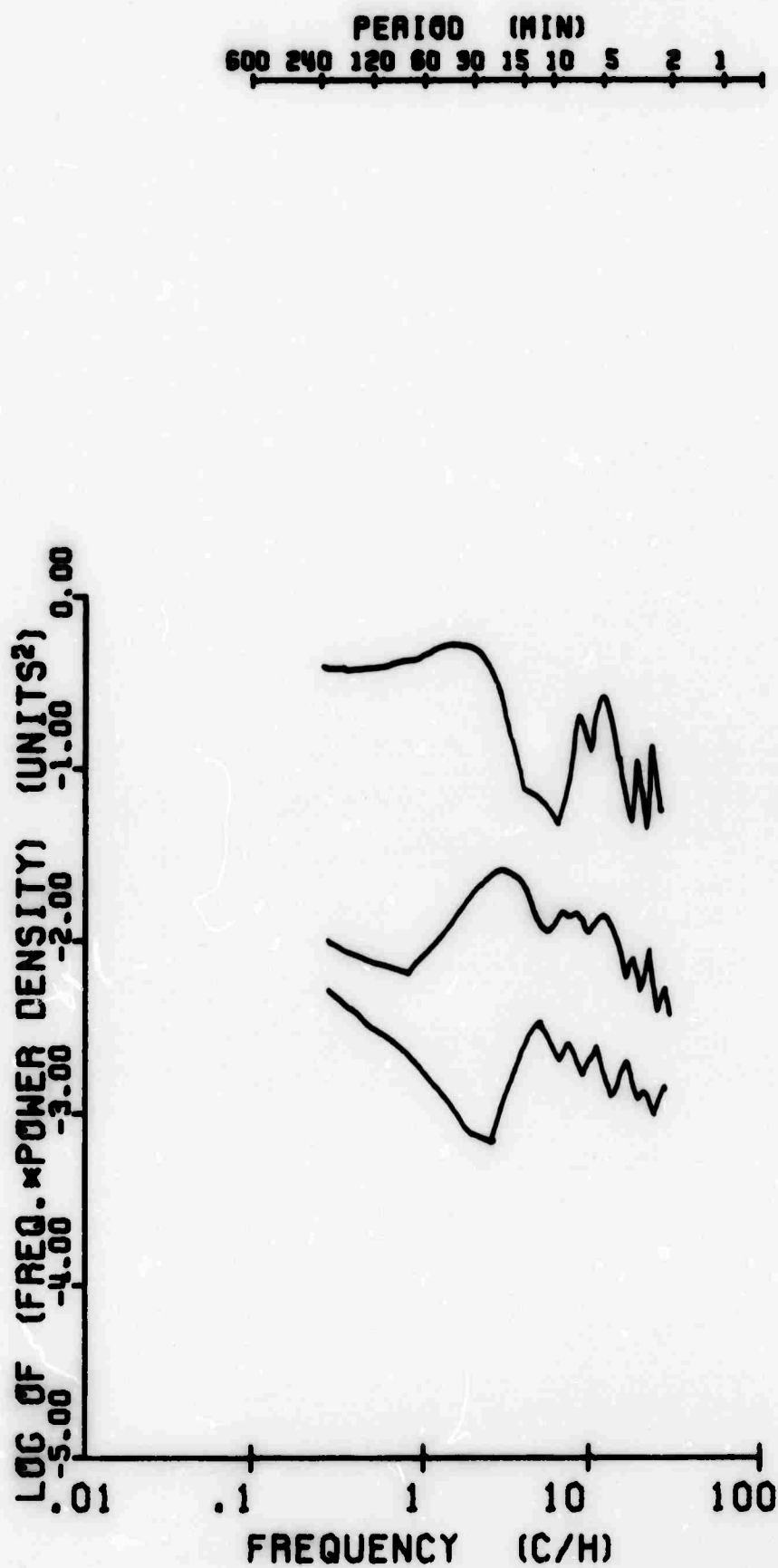


FIG. 2.44 Power spectra of phase-path doppler records for 6.030, 4.824 and 2.412 MHz corresponding to the time interval 1810 - 2410 G.M.T. on June 10, 1969.



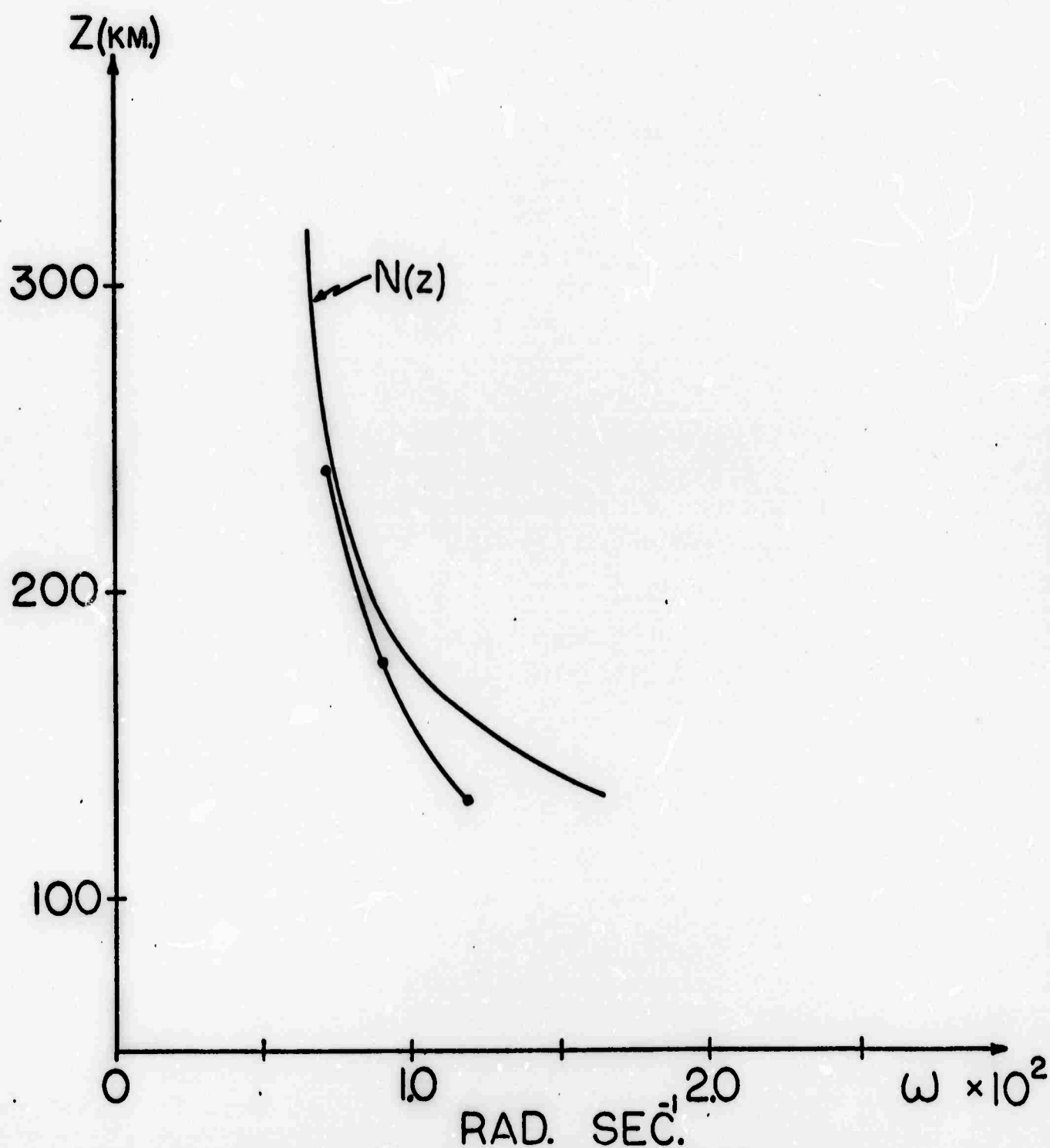


FIG. 2.45 Plot of peak period vs. height corresponding to power spectra of Fig. 2.43, together with  $N(z)$  curve from Tolstoy, 1967.



### 2.3.2 Microbarograph signal and noise fields

Acoustic-gravity waves generated in the atmosphere by nuclear explosions have been recorded and studied for many years. Many observational characteristics of these signals have been reported and various theoretical studies of source and propagation have been conducted. One property of the signals, however, that has not been quantitatively studied is the spatial coherence.

This section presents information regarding the similarity (i.e. coherence) of the signals and of atmospheric pressure background noise over distances of several kilometers to about 200 kilometers. Such information is required to design an array of microbarographs for the detection of the signals and is required in choosing a processing technique for the array data. The spatial coherence has not been previously studied due to a lack of adequate data, i.e. digitized data from a sufficiently large and dense array of microbarographs. The data is now available from the Hudson Laboratories' large aperture microbarograph array. The array was recording during the French thermonuclear test of 24 August 1968. The spatial coherencies of acoustic-gravity waves from that test have been determined by cross-spectral analyses of many pairs of stations of the array, at various separations. For comparison with the signal coherencies, an analysis of background noise coherencies has been performed.

#### Signal coherence

The 24 August 1968 French nuclear test was a megaton range explosion that generated acoustic-gravity waves clearly recorded on the Hudson Laboratories array. Various modes of propagation were recorded in the 1- to 5-minute period band. The separate modes were found by passing the data through successive  $1/2$



## Teledyne Isotopes

octave digital filters. The fundamental (3-5 minute period) and the first acoustic (2-3 minute) had the highest signal to noise ratios and were chosen for a study of their spatial coherence. Cross-spectral analyses were performed between almost all combinations of pairs of stations in the array giving coherencies for many station separations.

The signals from the French test site in the South Pacific crossed the array travelling into  $50^\circ$  azimuth. Coherencies for station pairs aligned  $\pm 25^\circ$  from the direction of signal travel (that is,  $50^\circ \pm 25^\circ$ ) are shown in Figure 2.46 for the first acoustic mode (2-3 minute period), as a function of station separation. Also shown are coherencies for pairs aligned  $\pm 25^\circ$  from the normal to the direction of travel. It is clear that the transverse coherencies are higher than the parallel coherencies at large separations, that is, the waves are long-crested. All coherencies (signal or noise), of course, approach unity at small separations.

A similar analysis was performed on the fundamental acoustic mode (3-5 minute period). Figure 2.47 shows that the transverse coherence is again greater than the parallel coherence. A study of the spatial coherence of higher acoustic modes and of the gravity modes is in progress and will be included in the final copy of this report.

### Noise coherence

The data for noise coherencies were chosen from two intervals of time. One interval (1 hour long) was chosen two hours prior to the signal arrival. This data gave the noise coherencies (2-3 minute band) at the larger station separations of Figure 2.48. The other interval of time was a one-hour sample several months before signal arrival, when the small array in the insert of Figure 2.1 was operating. The data from this small array



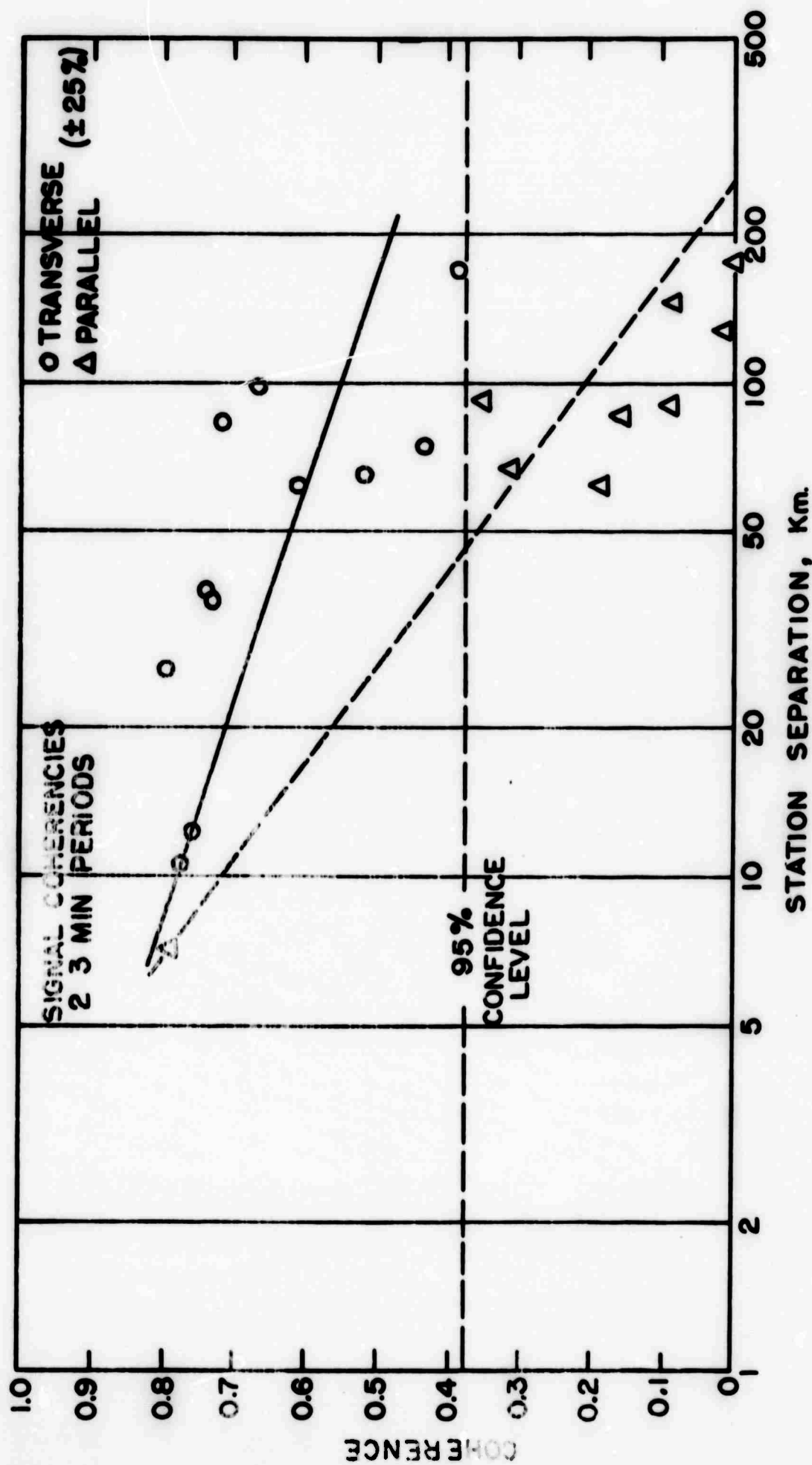


FIG. 2.46 Coherencies of the first acoustic mode, parallel and transverse to the direction of signal travel, from the French test of August 24, 1968. There is 95% confidence that coherencies above 0.38 are significant and not a statistical accident.



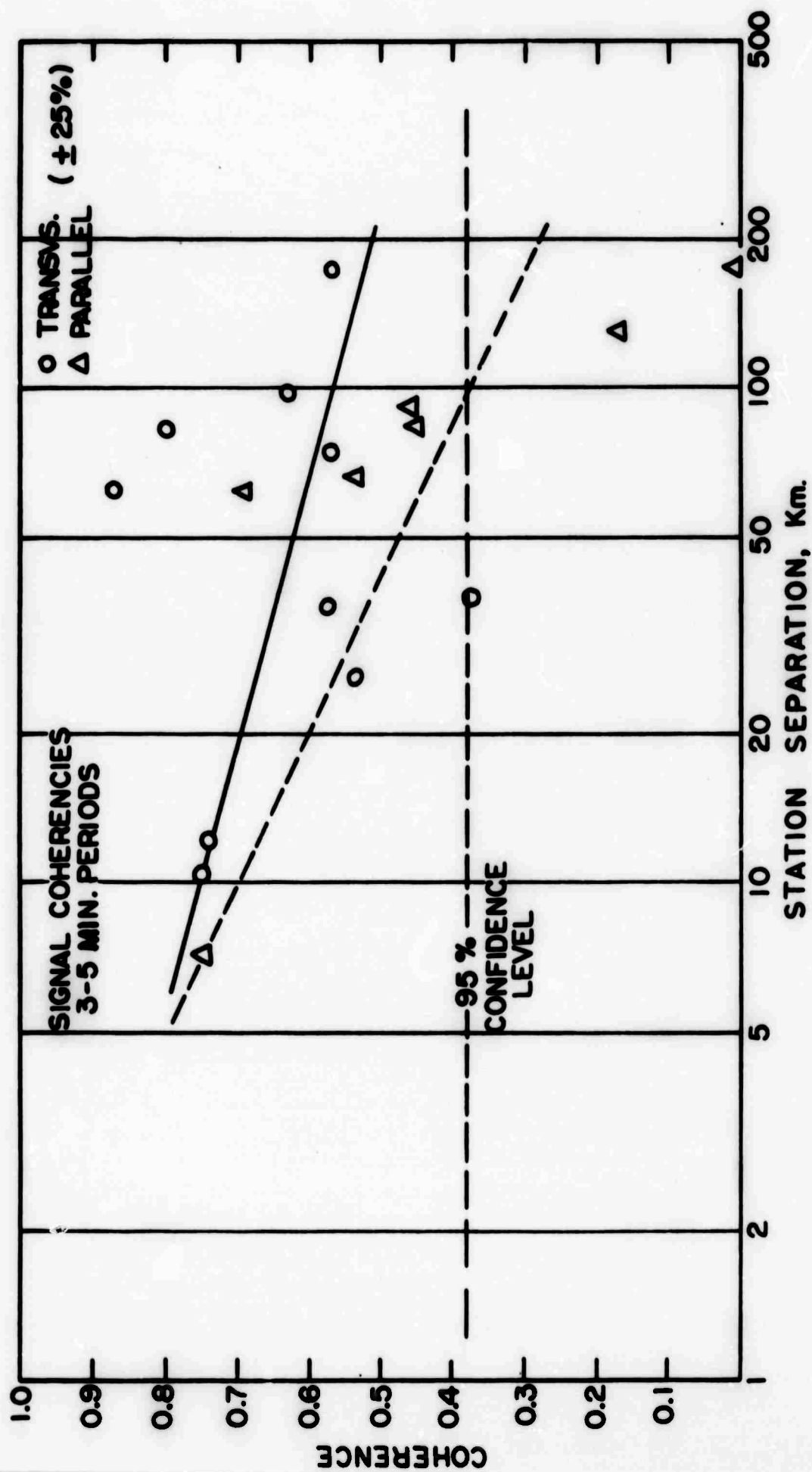


FIG. 2.47 Coherencies of the fundamental acoustic mode, parallel and transverse to the direction of travel, from the French test of August 24, 1968.



## Teledyne Isotopes

provided the coherency figures at the small separations (less than 14 km) of Figure 2.48. We see that over a wide range of separations the coherencies are almost all below the 95% confidence level.

In order to find the short period limit at which the noise becomes coherent, 24 cross-spectral measurements were performed between stations of the small array and mean coherencies were computed for separations of 1.4 to 14 km. Figure 2.49 shows mean coherencies at 12, 4, and 3-minute periods. At these periods the coherencies drop to a level of "random" coherence in several kilometers.

### Results

Figure 2.50 summarizes the results of the signal- and noise-coherence study. The coherence of acoustic signals is well above that of the background noise at separations greater than 3 or 4 kilometers. The signal coherence remains quite high out to separations of 50 km (or even more for the transverse coherencies).

It is apparent that even for arrays of many tens of kilometers aperture, the signal coherence is high enough to beamform with the entire array. Beamforming on 2-5 minute periods was, in fact, quite successful over the 200 km-aperture Hudson Laboratories array.

### Group velocity curves of long period atmospheric waves

Long period (10-15 minutes), high velocity (600 m/sec) atmospheric pressure waves have been observed on the Hudson Laboratories large aperture microbarograph array. Through beamforming techniques, the signals have been observed travelling both the short and the long great circle paths away from the sites of nuclear detonations. Group velocity curves of these signals



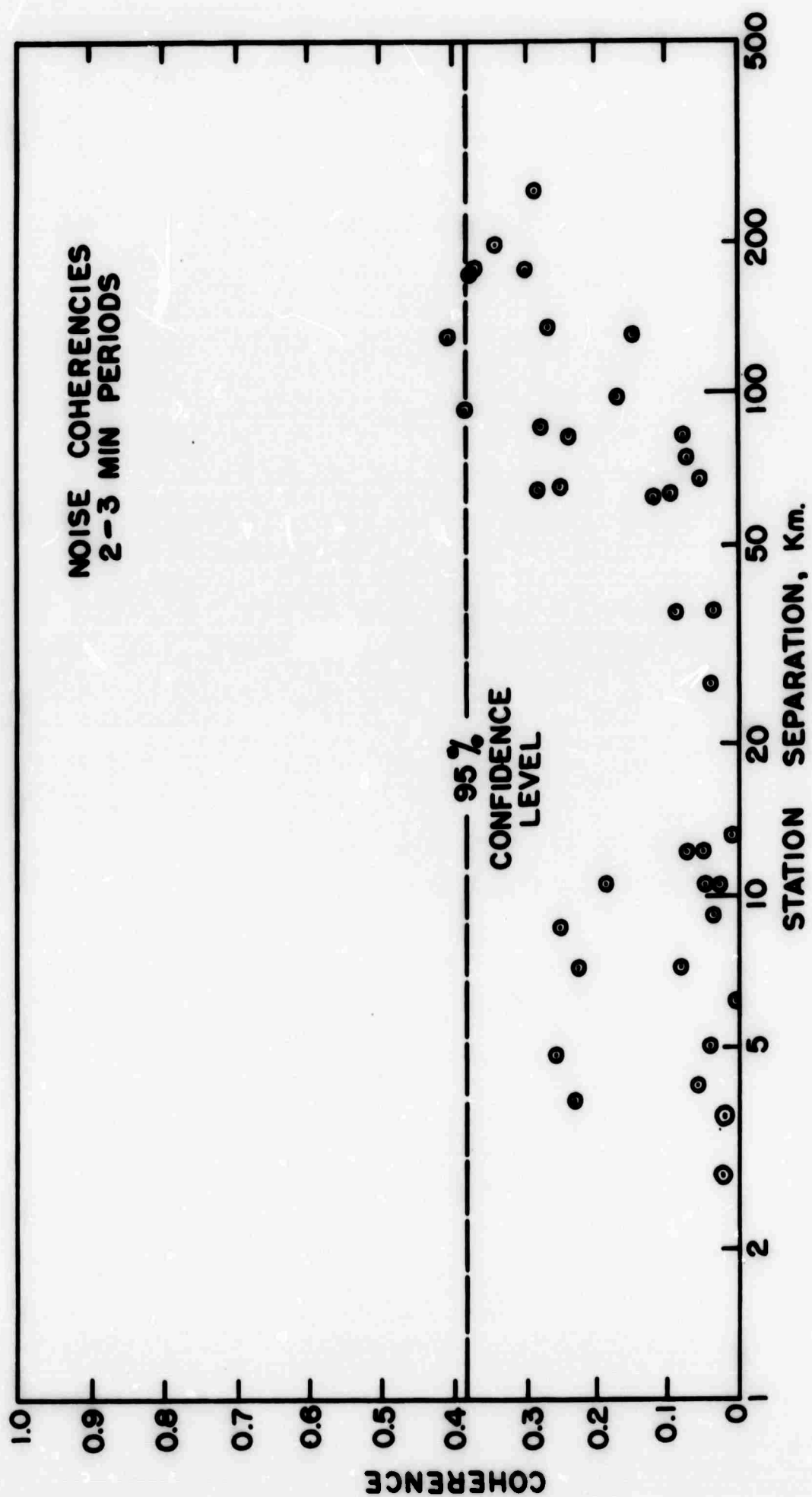


FIG. 2.48 Coherencies in the 2-3 minute period band of background noise , samples prior to signal arrival.



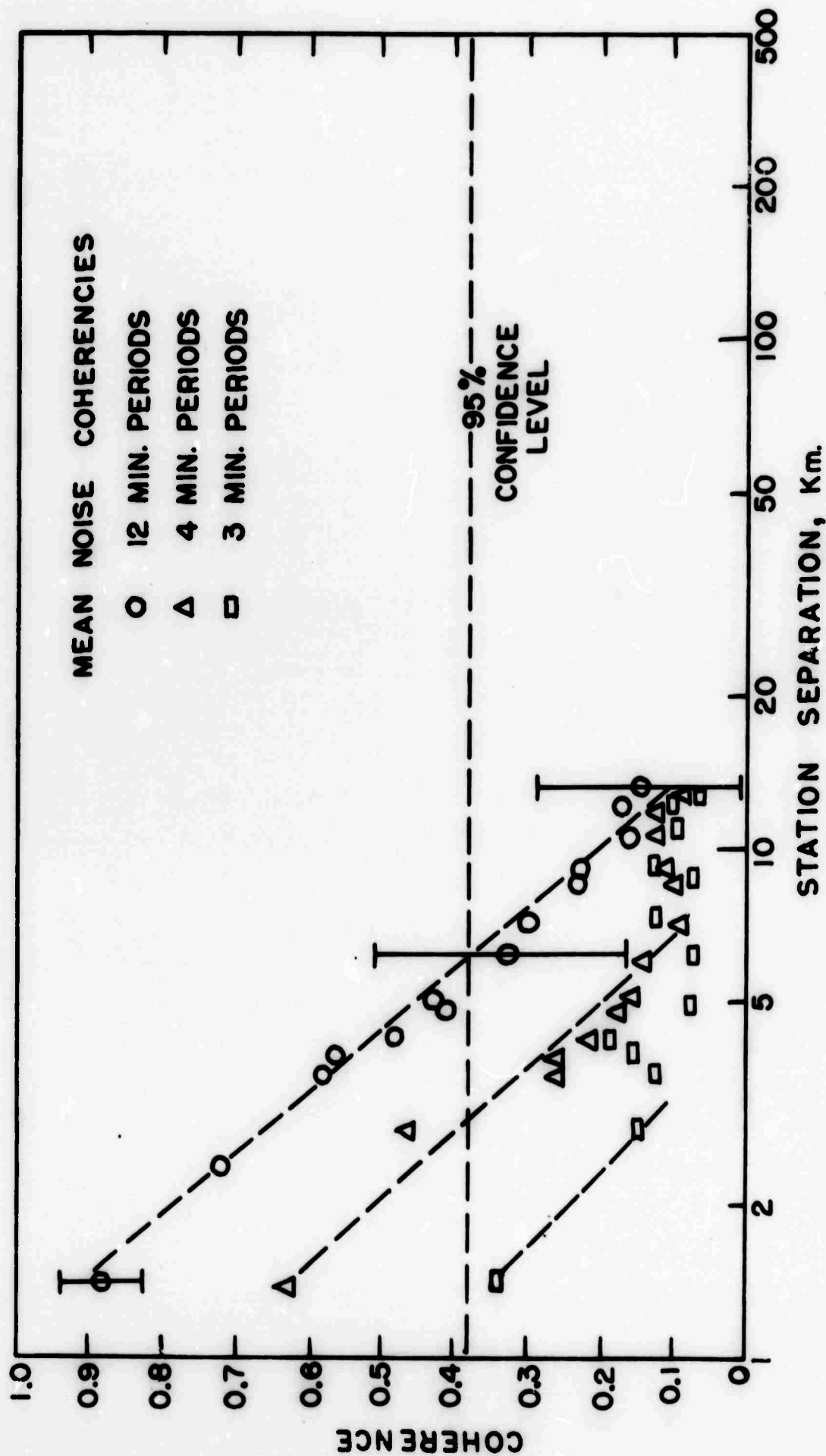


FIG. 2.49 Mean noise coherencies showing rapid decrease with distance. Each point is the mean of 24 coherencies. Standard deviation bars are shown.



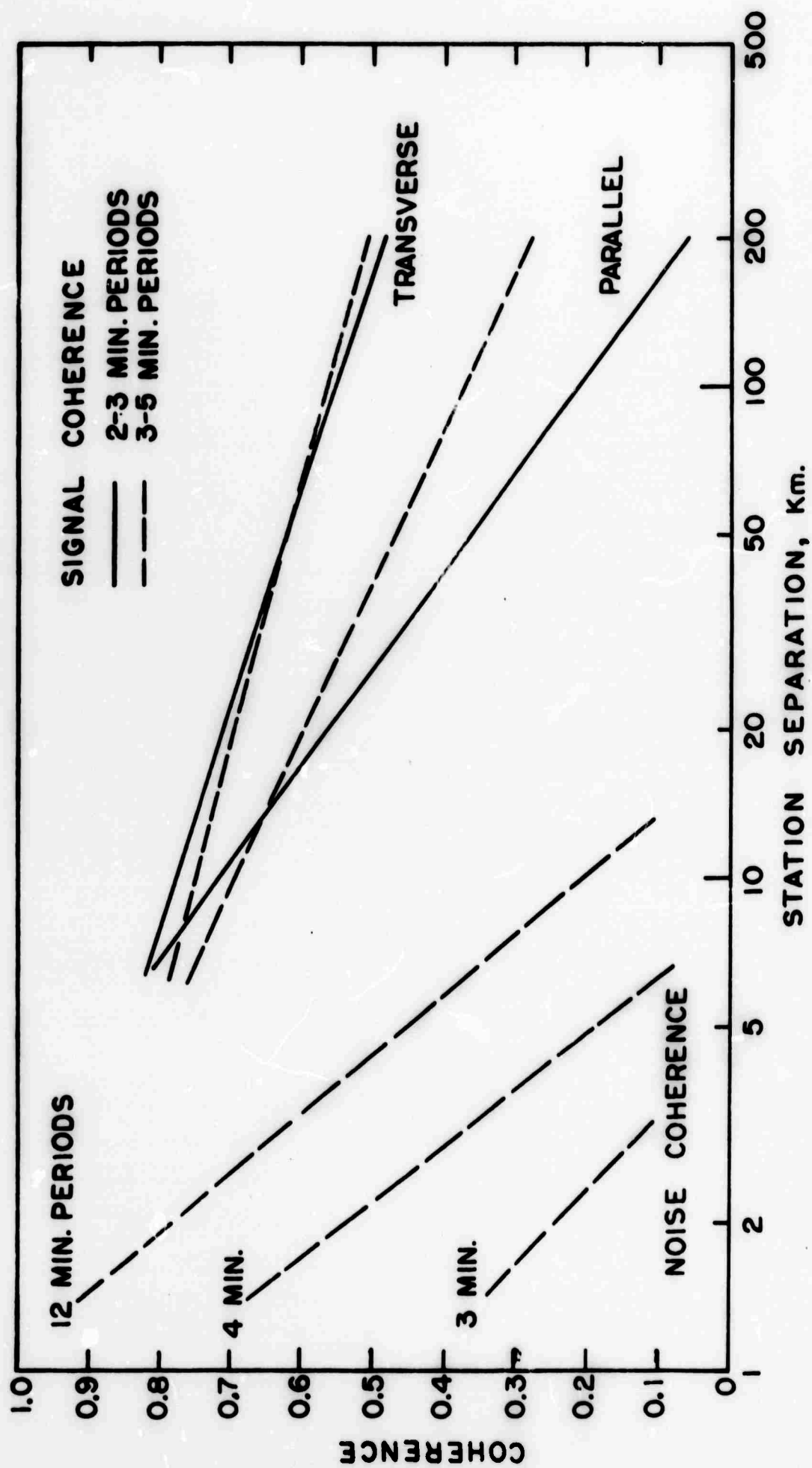


FIG. 2.50 Summary of the spatial coherence of signal and noise.



## Teledyne Isotopes

have been determined by the method of plotting arrival times of peaks and troughs of the wavetrain versus the peak or trough number. Figure 2.51 shows the dispersion curves from three nuclear detonations. The curves labeled D are obtained from the direct, short-path arrivals. The curves labeled A are from the antipodal, long-path arrivals.

As seen, the long periods travel with higher velocity. This type of dispersion is common to internal gravity waves, surface gravity waves and the long period branch of the fundamental acoustic mode.

It is interesting to note that the velocities are computed as higher for the antipodal arrival. The group velocities are computed as the total distance travelled divided by the total travel time. The higher antipodal velocity suggests that the travel times used were too high, that is, that these very long wavelength signals were not initiated at the instant of detonation. Rather, it took many tens of minutes to start the waves moving. Using overly-long travel times (from the moment of detonation) has the greatest depressing effect on the short path velocities. If the travel times are shortened to bring the short and long path velocities into coincidence, the group velocities lie in the 600-700 m/sec range.

Thus these results not only tell us the range of the group velocities and the sense of dispersion, but also indicate that the source mechanism requires many tens of minutes to initiate such long period, long wavelength waves.



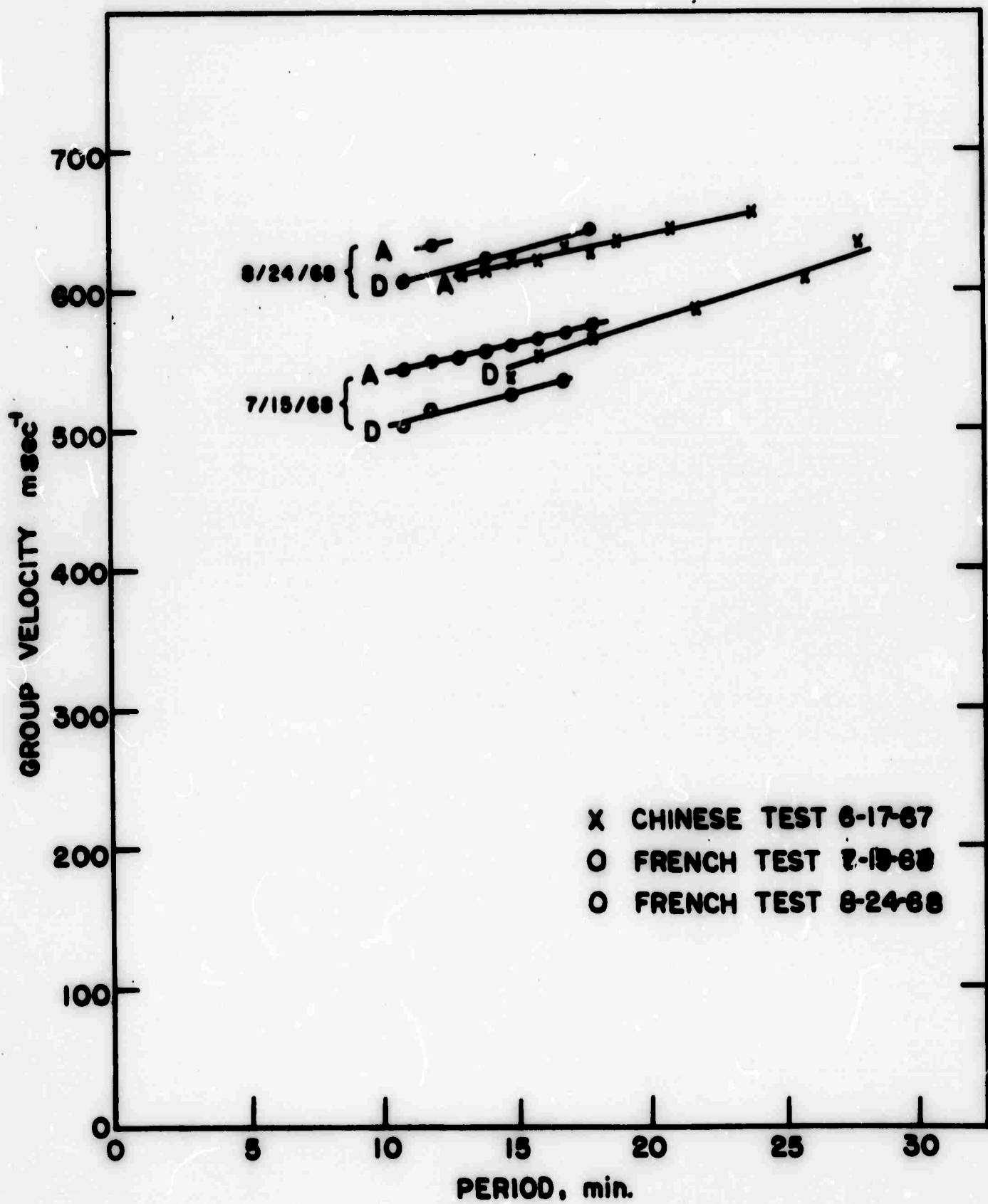


FIG. 2.51 Group velocity dispersion curves for nuclear detonations.



### 3. THEORETICAL ATMOSPHERIC PHYSICS

#### 3.1 Wave Propagation

It is known (Herron and Tolstoy, 1969) that internal gravity waves are associated with the jet stream. It has been hypothesized that these internal gravity waves are generated by a non-linear interaction of instability (Tollmien-Schlichting) waves. The instability waves are due to the unstable jet stream. It is therefore desirable to study the interaction of instability waves in the atmosphere (due to the existence of wind shear) and internal gravity waves (due to atmospheric stratification). In order to simplify the computation, compressibility will be neglected. Since the phenomena under study do not depend on the compressibility in any crucial way, this seems to be justified.

Let the x-z plane be horizontal, the y axis vertical (positive upwards). The equations of motion are:

$$\frac{\partial \rho}{\partial t} + \nabla \cdot (\rho \vec{V}) = 0, \quad (3.1)$$

$$\rho \left[ \frac{\partial \vec{V}}{\partial t} + (\vec{V} \cdot \nabla) \vec{V} \right] + \nabla P + \hat{\xi} \rho g = \mu \nabla^2 \vec{V}, \quad (3.2)$$

$$\frac{\partial \theta}{\partial t} + (\vec{V} \cdot \nabla) \theta = K \nabla^2 \theta. \quad (3.3)$$



Here  $\rho$  is the density,  $\vec{V}$  is the velocity,  $p$  is the pressure,  $g$  is the acceleration of gravity,  $\mu$  is the viscosity coefficient,  $\theta$  is the temperature,  $k$  is coefficient of thermal conductivity and

$$\hat{g} = (0, 1, 0). \quad (3.4)$$

Koppel (1964) has shown that both viscosity and thermal conductivity must be retained in order that the small disturbance equations be non-singular and thus be physically meaningful. It can be shown easily that these equations are equivalent to

$$\vec{\nabla} \cdot \vec{V} = 0, \quad (3.5)$$

$$\frac{\partial p}{\partial t} + (\vec{\nabla} \cdot \vec{\nabla})p = k \nabla^2 p, \quad (3.6)$$

$$\rho \left[ \frac{\partial \vec{V}}{\partial t} + (\vec{\nabla} \cdot \vec{\nabla})\vec{V} \right] + \vec{\nabla} p + \hat{g} \rho g = \mu \nabla^2 \vec{V}. \quad (3.7)$$

In deriving these equations it has been assumed that the temperature and density are related by

$$\rho/\rho_0 = 1 - a(\theta - \theta_0), \quad (3.8)$$

where  $a$  is the coefficient of thermal expansion,  $\theta_0$  is a reference temperature and  $\rho_0$  is the density at temperature  $\theta_0$ ; the Boussinesq approximation has also been made, that is, in the momentum conservation equation the variation of density is neglected in all terms except the one containing  $g$ .



Assume that the flow is two-dimensional, independent of  $z$ , and introduce a stream function  $\Psi$ , with  $u$  and  $v$ , the velocity components in the  $x$  and  $y$  directions given by

$$u = \frac{\partial \Psi}{\partial y}, \quad v = -\frac{\partial \Psi}{\partial x}. \quad (3.9)$$

Then the equations of motion reduce to

$$\frac{\partial \rho}{\partial t} + \frac{\partial \Psi}{\partial y} \frac{\partial \rho}{\partial x} - \frac{\partial \Psi}{\partial x} \frac{\partial \rho}{\partial y} = \kappa \nabla^2 \rho, \quad (3.10)$$

$$\rho \left[ \frac{\partial}{\partial t} + \frac{\partial \Psi}{\partial y} \frac{\partial}{\partial x} - \frac{\partial \Psi}{\partial x} \frac{\partial}{\partial y} \right] \nabla^2 \Psi = g \frac{\partial \rho}{\partial x} + \mu \nabla^4 \Psi. \quad (3.11)$$

Now the linearized equations can be derived by writing

$$\Psi = \Psi_0 + \epsilon \Psi_1 + O(\epsilon^2), \quad (3.12)$$

$$\rho = \rho_0 + \epsilon \rho_1 + O(\epsilon^2), \quad (3.13)$$

and substituting into (3.10) and (3.11). At this point the base flow, given by  $\rho_0$  and  $\Psi_0$ , is taken to be a steady flow with density stratification plus a wave (either a stability wave or an internal gravity wave).

Therefore assume that

$$\rho_0 = \rho_{00}(y) + \delta \rho_{01}(x, y, t), \quad (3.14)$$

$$\Psi_0 = \Psi_{00}(y) + \delta \Psi_{01}(x, y, t). \quad (3.15)$$



The undisturbed density is given by  $\rho_{00}(y)$  and  $\bar{u}_{00}(y) = \partial \psi_{00} / \partial y$  is the base shear flow. The terms  $\rho_{01}$  and  $\psi_{01}$  describe a wave, of amplitude  $\delta$ , propagating through the flow. In order to have a consistent description one must take

$$\rho_1 = \rho_{01}(x, y, t) + \delta \rho_{11}(x, y, t) + O(\delta^2), \quad (3.16)$$

$$\psi_1 = \psi_{01}(x, y, t) + \delta \psi_{11}(x, y, t) + O(\delta^2). \quad (3.17)$$

It is assumed that

$$\epsilon \ll \delta \ll 1, \quad (3.18)$$

so that the linearization is valid. Substitute into the basic equations, again using the Boussinesq approximation. The quantities  $\rho_{00}$  and  $\psi_{00}$  satisfy the equations identically. For the others it is found that

$$\left( \frac{\partial}{\partial t} + U_{00} \frac{\partial}{\partial x} \right) \rho_{01} - \frac{d\rho_{00}}{dy} \frac{\partial \psi_{01}}{\partial x} - \kappa \nabla^2 \rho_{01} = 0, \quad (3.19)$$

$$\begin{aligned} \left( \frac{\partial}{\partial t} + U_{00} \frac{\partial}{\partial x} \right) \nabla^2 \psi_{01} - \frac{d^2 U_{00}}{dy^2} \frac{\partial \psi_{01}}{\partial x} \\ - \frac{g}{\rho_{00}} \frac{\partial \rho_{01}}{\partial x} - \nu \nabla^4 \psi_{01} = 0. \end{aligned} \quad (3.20)$$

The equations satisfied by  $\rho_{10}$  and  $\psi_{10}$  are identical to (3.19) and (3.20).



And for the  $\rho_{11}$  and  $\psi_{11}$  the governing equations are

$$\begin{aligned}
 D \nabla^2 \psi_{11} - \frac{d^2 U_{00}}{dy^2} \frac{\partial \psi_{11}}{\partial x} - \frac{g}{\rho_{00}} \frac{\partial \rho_{11}}{\partial x} - \nu \nabla^4 \psi_{11} = & \quad (3.21) \\
 & \left[ \rho_{10} \frac{d^2 U_{00}}{dy^2} + \frac{\partial \rho_{10}}{\partial y} \frac{d U_{00}}{dy} \right] \frac{\partial \psi_{01}}{\partial x} - \left[ \rho_{10} D \nabla^2 + \frac{\partial \rho_{10}}{\partial y} D \frac{\partial}{\partial y} \right] \psi_{01} \\
 & + \left[ \rho_{01} \frac{d^2 U_{00}}{dy^2} + \frac{\partial \rho_{01}}{\partial y} \frac{d U_{00}}{dy} \right] \frac{\partial \psi_{10}}{\partial x} - \left[ \rho_{01} D \nabla^2 + \frac{\partial \rho_{01}}{\partial y} D \frac{\partial}{\partial y} \right] \psi_{10} \\
 & - \left[ \frac{\partial \psi_{10}}{\partial y} \frac{\partial}{\partial x} - \frac{\partial \psi_{00}}{\partial x} \frac{\partial}{\partial y} \right] \nabla^2 \psi_{01} \\
 & - \left[ \frac{\partial \psi_{01}}{\partial y} \frac{\partial}{\partial x} - \frac{\partial \psi_{01}}{\partial x} \frac{\partial}{\partial y} \right] \nabla^2 \psi_{10} \\
 & - \frac{\partial \rho_{10}}{\partial x} D \frac{\partial \psi_{01}}{\partial x} - \frac{\partial \rho_{01}}{\partial x} D \frac{\partial \psi_{10}}{\partial x},
 \end{aligned}$$

with

$$D \equiv \frac{\partial}{\partial t} + U_{00} \frac{\partial}{\partial x}, \quad (3.22)$$

$$\begin{aligned}
 D \rho_{11} - \frac{d \rho_{00}}{dy} \frac{\partial \psi_{11}}{\partial x} - \kappa \nabla^2 \rho_{11} = & \frac{\partial \rho_{01}}{\partial y} \frac{\partial \psi_{10}}{\partial x} + \frac{\partial \rho_{10}}{\partial y} \frac{\partial \psi_{01}}{\partial x} \\
 & - \frac{\partial \rho_{01}}{\partial x} \frac{\partial \psi_{10}}{\partial y} - \frac{\partial \rho_{10}}{\partial x} \frac{\partial \psi_{01}}{\partial y}.
 \end{aligned} \quad (3.23)$$



## Teledyne Isotopes

If wave solutions are sought, i.e.,  $\rho_{01}$  and  $\psi_{01}$  or  $\rho_{10}$  and  $\psi_{10}$  are taken to be

$$\rho_{01} = \eta(y) e^{i(\alpha x - \omega t)}, \quad (3.24)$$

$$\psi_{01} = \phi(y) e^{i(\alpha x - \omega t)}, \quad (3.25)$$

then it is found that

$$i(-\omega + \alpha U_{00})\eta + i\alpha\beta\phi - \kappa L\eta = 0, \quad (3.26)$$

$$i(-\omega + \alpha U_{00})L\phi - i\alpha \frac{d^2 U_{00}}{dy^2} \phi - i\alpha g\eta - \gamma L^2 \phi = 0, \quad (3.27)$$

where

$$\beta = - \frac{d\rho_{00}}{dy}, \quad (3.28)$$

and

$$L \equiv \frac{d^2}{dy^2} - \alpha^2. \quad (3.29)$$

Equations (3.26) and (3.27) govern (in the linear approximation) the propagation of waves in a stratified atmosphere with wind shear. In various limits some well known results are obtained. For example, if  $\beta = g = K = 0$ , there is a homogeneous atmosphere in the absence of gravity and thermal conduction and (3.27) becomes, with  $\omega = \alpha c$

$$(U_{00} - c)L\phi - \frac{d^2 U_{00}}{dy^2} \phi + \left(\frac{i\gamma}{\alpha}\right)L^2 \phi = 0, \quad (3.30)$$



which is just the Orr-Sommerfeld equation (Lin, 1955). This is well known in the theory of hydrodynamic stability and describes the propagation of stability waves in shear flows. If, on the other hand,  $\bar{U}_{00} = 0$  and  $v = K = 0$ , that is, an inviscid nonheat-conducting fluid is considered, with no wind, then equations (3.26) and (3.27) reduce to

$$\frac{d^2 \phi}{dy^2} + \alpha^2 \left( \frac{g\beta}{\omega^2} - 1 \right) \phi = 0. \quad (3.31)$$

This is just the equation governing the propagation of internal gravity waves in a stratified, incompressible inviscid fluid (Tolstoy, 1963). It can be noted here that the effect of the Boussinesq approximation is to drop a term  $\beta^2/4$ . That is, the exact equation, without making the Boussinesq approximation, would be

$$\frac{d^2 \phi}{dy^2} + \left[ \alpha^2 \left( \frac{g\beta}{\omega^2} - 1 \right) - \frac{1}{4} \beta^2 \right] \phi = 0. \quad (3.32)$$

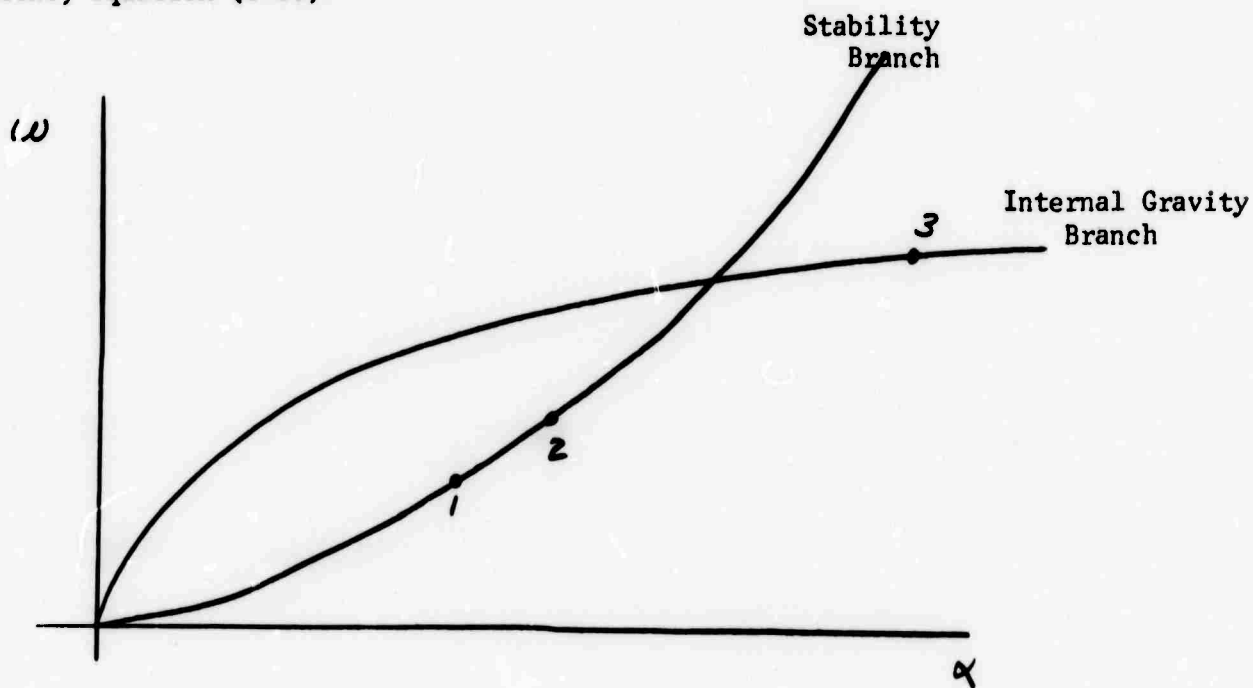
If the stratification is small, then  $\beta$  will be small and the neglect of  $\beta^2/4$  is reasonable.

The above discussion indicates that equations (3.26) and (3.27) should have two branches, a stability wave branch and an internal gravity wave branch. If  $\rho_{01}$  and  $\psi_{01}$  are proportional to  $\exp[i(\alpha_1 x - \omega_1 t)]$  and  $\rho_{10}$  and  $\psi_{10}$  are proportional to  $\exp[i(\alpha_2 x - \omega_2 t)]$  then equations (3.21) and (3.22) show that  $\rho_{11}$  and  $\psi_{11}$  will have solutions proportional to  $\exp[i(\alpha_3 x - \omega_3 t)]$  where

$$\alpha_3 = \alpha_1 \pm \alpha_2, \quad \omega_3 = \omega_1 \pm \omega_2. \quad (3.33)$$



The sketch below shows schematically the dispersion relation for stability waves and internal gravity waves. It is clear that there can be a resonance between various waves. For example, the two stability waves marked 1 and 2, and the internal gravity wave marked 3, will satisfy the resonance conditions, equation (3.33).



In order to proceed any further with the calculation a model must be chosen for the density variation and velocity field in the undisturbed flow. A particularly simple model has been chosen so as to minimize the computation. The model consists of a duct bounded by rigid planes; the Väisälä frequency is assumed to be constant; that is, we assume

$$\beta = - \frac{d\rho_0}{dy} \quad (3.34)$$

is constant; and finally it is assumed that the shear flow has a parabolic profile ( $\bar{U}_{00} = 1 - y^2$ ) since this is the simplest profile with varying shear.



## Teledyne Isotopes

In all that follows, dimensionless variables will be used. The height of the duct is  $\ell$ ; the scaling length will be  $\ell/2$ . The maximum velocity in the duct is  $\bar{U}_0$  and this will be used as the velocity scale. In terms of these variables, it can be shown that the linear equations (3.26) and (3.27) are

$$\sigma \eta = \left[ \frac{1}{R P} L - i \alpha \bar{U}_0 \right] \eta - i \alpha \varphi, \quad (3.35)$$

$$\sigma L \varphi = i \alpha \left[ \bar{U}_0'' - \bar{U}_0 L \right] \varphi + \frac{1}{R} L^2 \varphi + i \alpha J \eta, \quad (3.36)$$

where  $\sigma$  is the complex frequency,

$R$  is the Reynolds number,  $= \bar{U}_0 \ell / 2 \nu$

$P$  is the Prandtl number,  $= \nu / K$

$J$  is the Richardson number,  $= \beta g \ell^2 / 4 \bar{U}_0^2$

and  $L = d^2/dy^2 - \alpha^2$ .

The boundary conditions on  $\eta$  and  $\varphi$  are that

$$\eta(\pm 1) = \varphi(\pm 1) = \varphi'(\pm 1) = 0 \quad (3.37)$$

The method to be used to solve equations (3.35) and (3.36) with the boundary conditions (3.37) is to choose a suitable set of expansion functions and expand  $\eta$  and  $\varphi$  in a series of these functions. There is no necessity to use the same set of functions to expand  $\eta$  as is used for  $\varphi$  and, in fact, different sets of expansion functions will be used.

A suitable set of expansion functions for  $\varphi$  is the set of eigenfunctions of



$$L^2 C_n = -\lambda_n L C_n, \quad (3.38)$$

$$C_n(\pm 1) = C_n'(\pm 1) = 0. \quad (3.39)$$

Since equations (3.38) and (3.39) are symmetric, the eigenfunctions must be either symmetric or anti-symmetric. For the present calculation it is only necessary to consider the symmetric expansion functions.

The symmetric eigenfunctions are

$$C_n(y) = \bar{c}_n \left[ \frac{\cos(\gamma_n y)}{\cos(\gamma_n)} - \frac{\cosh(\alpha y)}{\cosh(\alpha)} \right], \quad (3.40)$$

where  $\gamma_n$  is the n'th root of

$$\gamma_n \tan(\gamma_n) + \alpha \tanh(\alpha) = 0, \quad (3.41)$$

$$\lambda_n = \gamma_n^2 + \alpha^2, \quad (3.42)$$

and  $\bar{c}_n$  is a normalization constant.

This approach, expansion in a series of orthogonal functions, although very powerful has only been used rarely in problems of this sort. These particular expansion functions, the  $C_n(y)$ , were first used by Dolph and Lewis (1958) in a study of hydrodynamic stability and were later suggested by Eckhaus (1965) as a suitable set of functions to use in non-linear stability calculations.



The  $\{C_n\}$  are a somewhat unusual set of functions. Equations (3.38) and (3.39) do not constitute the usual Sturm-Liouville (S.-L.) problem. The  $\{C_n\}$  have an unusual orthogonality property, which is, \*

$$\langle C_n, -L C_m \rangle = \delta_{nm}. \quad (3.43)$$

Further, the  $\{C_n\}$  do not have the usual completeness property of the S.-L. functions, (Courant-Hilbert, 1953). The S.-L. functions are complete with respect to the space of functions which are continuous and satisfy the same boundary conditions. If a function does not satisfy the boundary conditions, then the expansion converges non-uniformly in the interior and differs from the function by a constant at the boundary.

In contrast, it is easily shown that if one attempts to expand  $\cosh(\alpha y)$  or  $\sinh(\alpha y)$  in a series of the  $\{C_n\}$ , all of the expansion coefficients are identically zero. This implies that if one attempts to expand an arbitrary continuous symmetric function in terms of the  $\{C_n\}$ , then in the interior the expansion does not converge to the function but to the function minus a multiple of  $\cosh(\alpha y)$ . However, it can be shown that the  $\{C_n\}$  are complete with respect to the space of continuous functions which satisfy the boundary conditions (3.37).

A suitable set of expansion functions for  $\eta$  are the eigenfunctions of

$$L G_n = -\mu_n G_n, \quad (3.44)$$

$$G_n(\pm 1) = 0. \quad (3.45)$$

$$* \langle f, g \rangle \equiv \int_{-1}^1 f(y)g(y)dy$$



Again the eigenfunctions are either symmetric or anti-symmetric and only the symmetric functions are considered for the present. The symmetric eigenfunctions are

$$G_n(y) = \cos\left[\left(n - \frac{1}{2}\right)\pi y\right], \quad (3.46)$$

$$\mu_n = \left(n - \frac{1}{2}\right)^2 \pi^2 + \alpha^2. \quad (3.47)$$

Now set

$$\phi = \sum_{n=1}^{\infty} a_n C_n(y), \quad (3.48)$$

$$\eta = \sum_{n=1}^{\infty} b_n G_n(y), \quad (3.49)$$

and take the inner product of  $G_k(y)$  with equation (3.35) and  $C_k(y)$  with equation (3.36). After integrating by parts, using (3.48) and (3.49) and the orthogonality properties equation (3.43), it can be shown that equations (3.35) and (3.36) reduce to

$$\sigma a_k = -\left(\frac{\lambda_k}{PR} + i\alpha\right) a_k + i\alpha \sum_{n=1}^{\infty} F_{kn} a_n - i\alpha \int \sum_{n=1}^{\infty} V_{kn} b_n, \quad (3.50)$$

$$\sigma b_k = -\left(\frac{\mu_k}{PR}\right) b_k - i\alpha \sum_{n=1}^{\infty} G_{kn} b_k - i\alpha \sum_{n=1}^{\infty} V_{kn} a_n, \quad (3.51)$$

where, with

$$U_{c0} = 1 - y^2, \quad (3.52)$$



$$F_{kn} = \langle y^2 C_k, -LC_n \rangle + 2 \langle C_k, C_n \rangle, \quad (3.53)$$

$$G_{kn} = \langle G_k, G_n \rangle - \langle y^2 G_k, G_n \rangle, \quad (3.54)$$

and

$$V_{kn} = \langle G_k, C_n \rangle. \quad (3.55)$$

If the expansions in (3.48) and (3.49) are truncated at a finite number of terms, that is, if  $\eta$  and  $\varphi$  are approximated by a finite series, then (3.50) and (3.51) can be combined to give

$$\sigma \begin{pmatrix} A \\ B \end{pmatrix} = \begin{pmatrix} \mathcal{H} & \mathcal{K} \\ \mathcal{H} & \mathcal{G} \end{pmatrix} \begin{pmatrix} A \\ B \end{pmatrix}, \quad (3.56)$$

$$A = \begin{pmatrix} a_1 \\ a_2 \\ \vdots \\ a_n \end{pmatrix}, \quad B = \begin{pmatrix} b_1 \\ b_2 \\ \vdots \\ b_n \end{pmatrix}, \quad (3.57)$$

$$\mathcal{H}_{kn} = -\left(\frac{\lambda_k}{R} + i\alpha\right) \delta_{kn} + i\alpha F_{kn}, \quad (3.58)$$

$$\mathcal{G}_{kn} = -\left(\frac{\mu_k}{PR}\right) \delta_{kn} - i\alpha G_{kn},$$

$$\mathcal{H}_{kn} = -i\alpha \mathcal{J} V_{kn}, \quad (3.59)$$

$$\mathcal{K}_{kn} = -i\alpha V_{kn}. \quad (3.60)$$



Then  $\sigma$  is just an eigenvalue of the matrix in (3.56) and by calculating the eigenvalues of this  $(2N \times 2N)$  matrix one obtains approximations to the first  $2N$  complex frequencies. Once the eigenvalues are known the wave forms can be obtained from the set of homogeneous linear equations with zero secular determinant.

The results of the calculations can be checked in a number of special cases. For example, if  $J = 0$ , then  $N$  of the eigenvalues ought to be the eigenvalues of the stability modes of Poiseuille flow. This has been verified in a number of cases.

Numerical results are presented for a representative case. The values assigned to the various scales and dimensionless parameters are:

$$\bar{U}_0 = 50 \text{ m/sec.}$$

$$l = 2 \text{ km.}$$

$$T_0 = l / 2\bar{U}_0 = 20 \text{ sec.}$$

$$\nu = 5 \times 10^4 \text{ cm}^2/\text{sec.}^*$$

$$R = \bar{U}_0 l / 2\nu = 10^4$$

$$P = 0.72$$

$$J = 0.005$$

Since (eq. 3.25) the stream function  $\Psi$  is of the form

$$\Psi = \varphi(y) e^{i(\alpha x + \sigma t)},$$

then

$$-\text{Im}(\sigma) = \omega, \tag{3.61}$$

the circular frequency, in dimensionless units and

\* The kinematic viscosity is taken to be an eddy viscosity for which this numerical value is representative of atmospheric conditions.



$$- \operatorname{Re}(\sigma) = \delta, \quad (3.62)$$

the damping coefficient, again in dimensionless units.

Thus,

$$\psi = e^{-\delta t} \varphi(y) e^{i(\alpha x - \omega t)}. \quad (3.63)$$

In Figure 3.1 the variation of the frequency,  $\omega$ , with the wave number  $\alpha$  is shown and in Figure 3.2 the variation of the damping coefficient,  $\delta$ , with wave number is shown (note that in Figure 3.1  $\delta \times 10$  is plotted). Curves are plotted for the first five modes where the modes are ordered with respect to the magnitude of the damping coefficient for small  $\alpha$ . It is obvious that there are two general classes of modes:

- 1) Modes for which the phase velocity

$$c = \omega/\alpha \approx 1, \quad (3.64)$$

these may be called the "fast" modes and include modes 1, 3, 4 and 5.

- 2) Modes for which

$$\omega \rightarrow \text{constant as } \alpha \rightarrow \infty \quad (3.65)$$

and thus

$$c \rightarrow 0 \text{ as } \alpha \rightarrow \infty, \quad (3.66)$$

these may be called the "slow" modes. Mode 2 is a "slow" mode, and although they are not shown, other of the higher, i.e. more rapidly damped modes are also "slow" modes.

As discussed above internal-gravity waves can propagate in a stationary, stratified fluid and Tollmien-Schlichting or instability waves can propagate in a shear flow in a homogeneous fluid. Therefore it is to be expected that



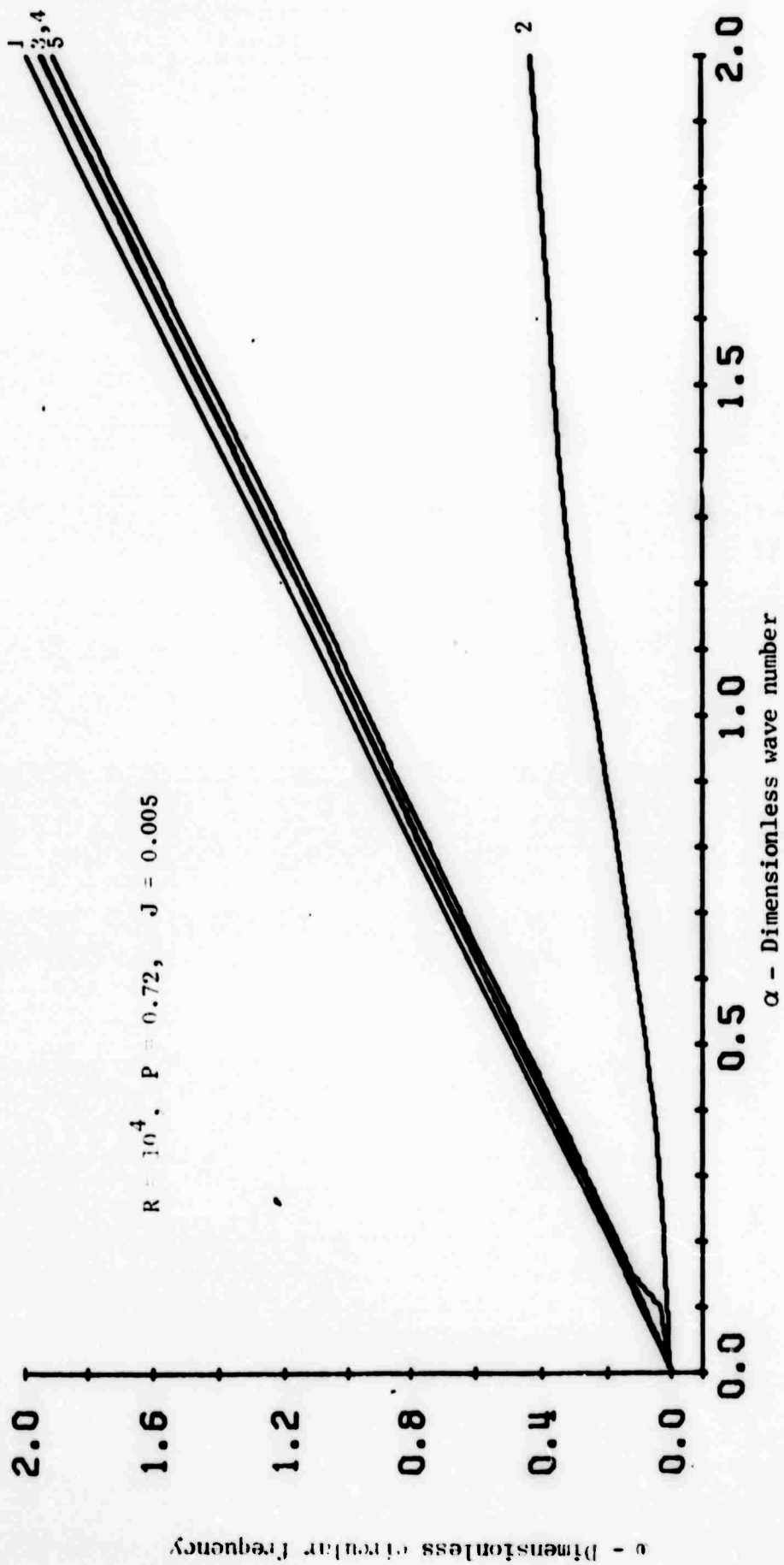


FIGURE 3.1



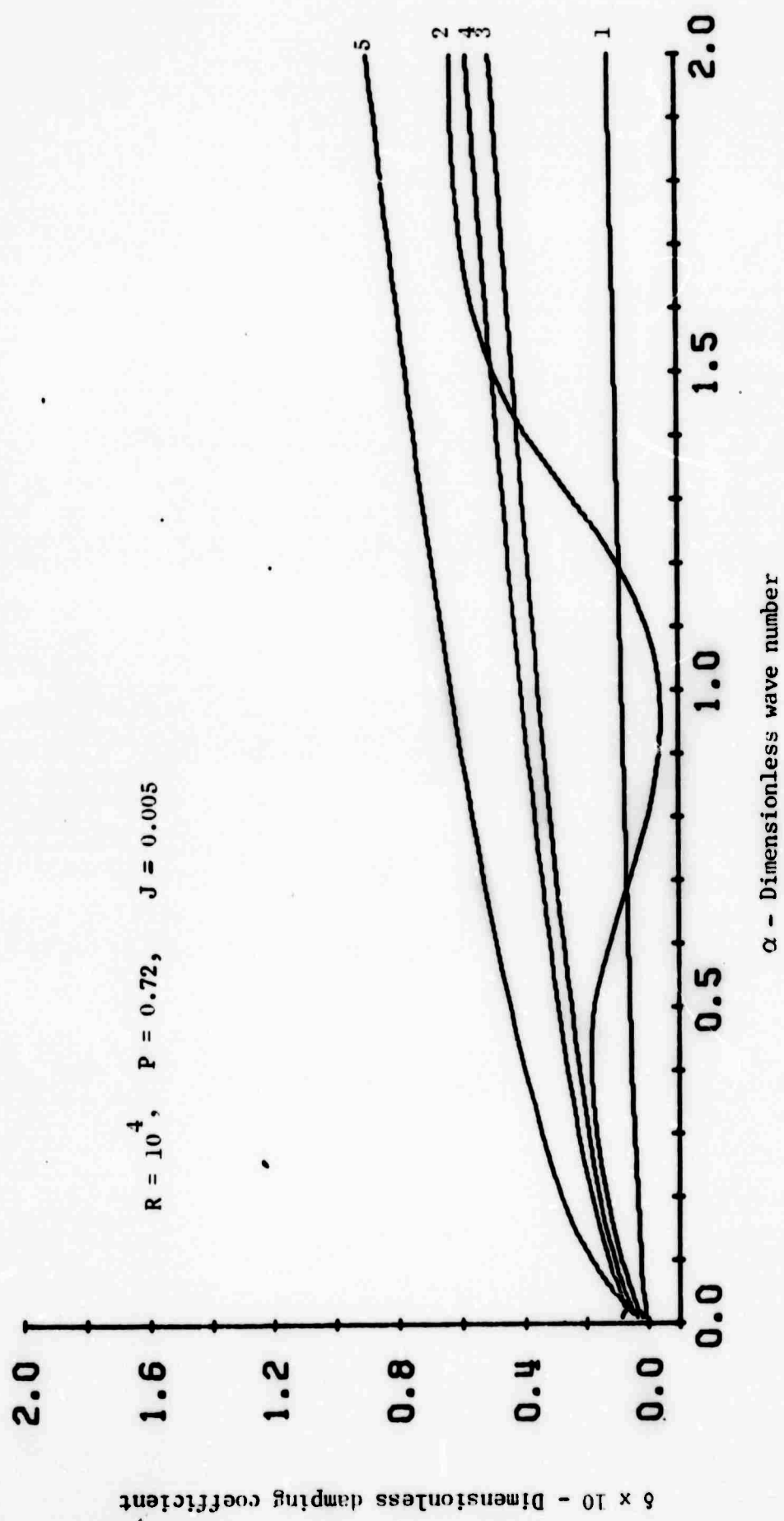


FIGURE 3.2



there will be both internal-gravity and Tollmien-Schlichting waves in a stratified shear flow. In Table 3.1,  $\omega$  and  $\delta$  have been listed for the first five modes for  $\alpha = 1.0$ , and also  $\omega$  and  $\delta$  for the corresponding case in the homogeneous shear flow with the same velocity profile. It is obvious that modes 1 and 4 are the internal gravity modes and modes 2, 3 and 5 are the Tollmien-Schlichting waves.

TABLE 3.1

FREQUENCY AND DAMPING COEFFICIENT

$\alpha = 1.0, \quad R = 10^4, \quad P = 0.72, \quad J = 0.005$

Mode Number	Stratified Shear Flow		Homogeneous Shear Flow	
	$\omega$	$\delta$	$\omega$	$\delta$
1	0.995	0.0084	-	-
2	0.237	-0.0039	0.237	-0.0032
3	0.964	0.0358	0.965	0.0352
4	0.959	0.0414	-	-
5	0.936	0.0636	0.936	0.0633



It can also be shown (see eqs. 3.35 and 3.36) as  $R \rightarrow \infty$  and assuming that  $\bar{U}_{\infty} = \text{constant} = 1$ , in dimensionless units, that

$$\omega = \alpha - O(J). \quad (3.67)$$

This shows that for small Richardson number ( $J$ ) the internal gravity modes are "fast" modes as shown in Figure 3.1 and Table 3.1.

It should also be noted that for  $0.8 \lesssim \alpha \lesssim 1.1$ , mode 2, the first T-S mode, is unstable as indicated by the fact that  $\delta$  is negative. This range of wave numbers is, to within the accuracy of the calculation, the same range of wave numbers for which the homogenous shear flow is unstable. The Richardson number is so small that the stability characteristics are not appreciably affected. For larger  $J$  the range of unstable wave numbers decreases and for sufficiently large  $J$  the flow is stable for all wave numbers.

Once the eigenvalues were obtained it was a simple matter to calculate the wave forms from the set of homogenous linear equations with zero secular determinant. These calculations have been carried for a number of cases and some sample results are shown in Figures 3.3 - 3.6. For all of these cases  $\alpha = 1.0$ . In Figure 3.3 the perturbation velocity field is shown for mode 1 at values of  $(\alpha x - \omega t) = 0, (\pi/4), 7\pi/4$  and Figure 3.4 shows the corresponding results for mode 2. The velocity scale in both figures is the same. The same information is presented in a somewhat different way in Figures 3.5 and 3.6. Figure 3.5 shows the streamlines for mode 1 and Figure 3.6 the streamlines for mode 2. The horizontal scale in Figures 3.5 and 3.6 has, however, been compressed in order to show a wavelength and a half, that is,  $0 \leq (\alpha x - \omega t) \leq 3\pi$  in Figures 3.5 and 3.6.



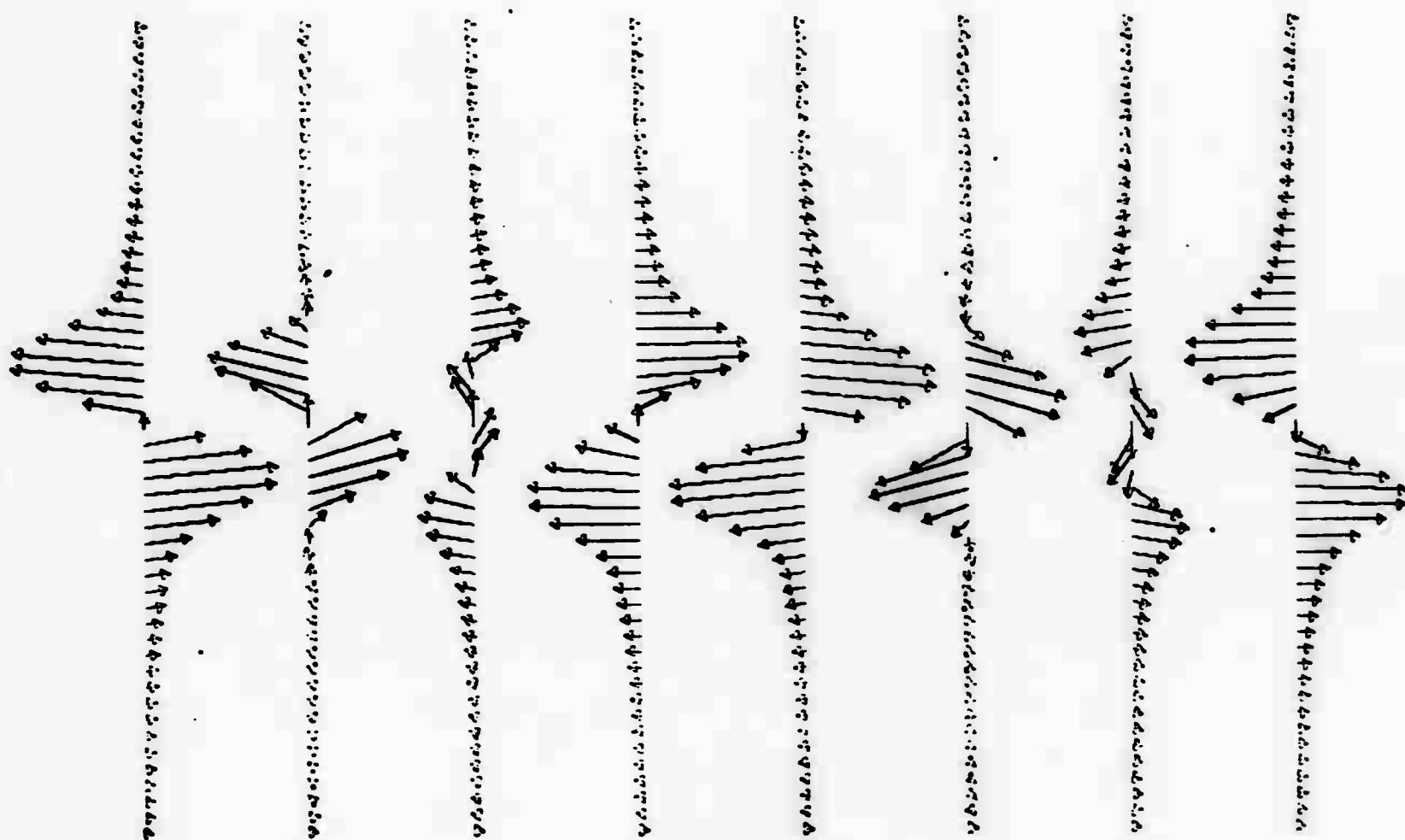


FIGURE 3.3 Velocity field for the first internal gravity wave mode  
 $\alpha = 1.0$ ,  $R = 10^4$ ,  $P = 0.72$ ,  $J = 0.005$ ,  $\omega = 0.995$ ,  $\delta = 0.0084$

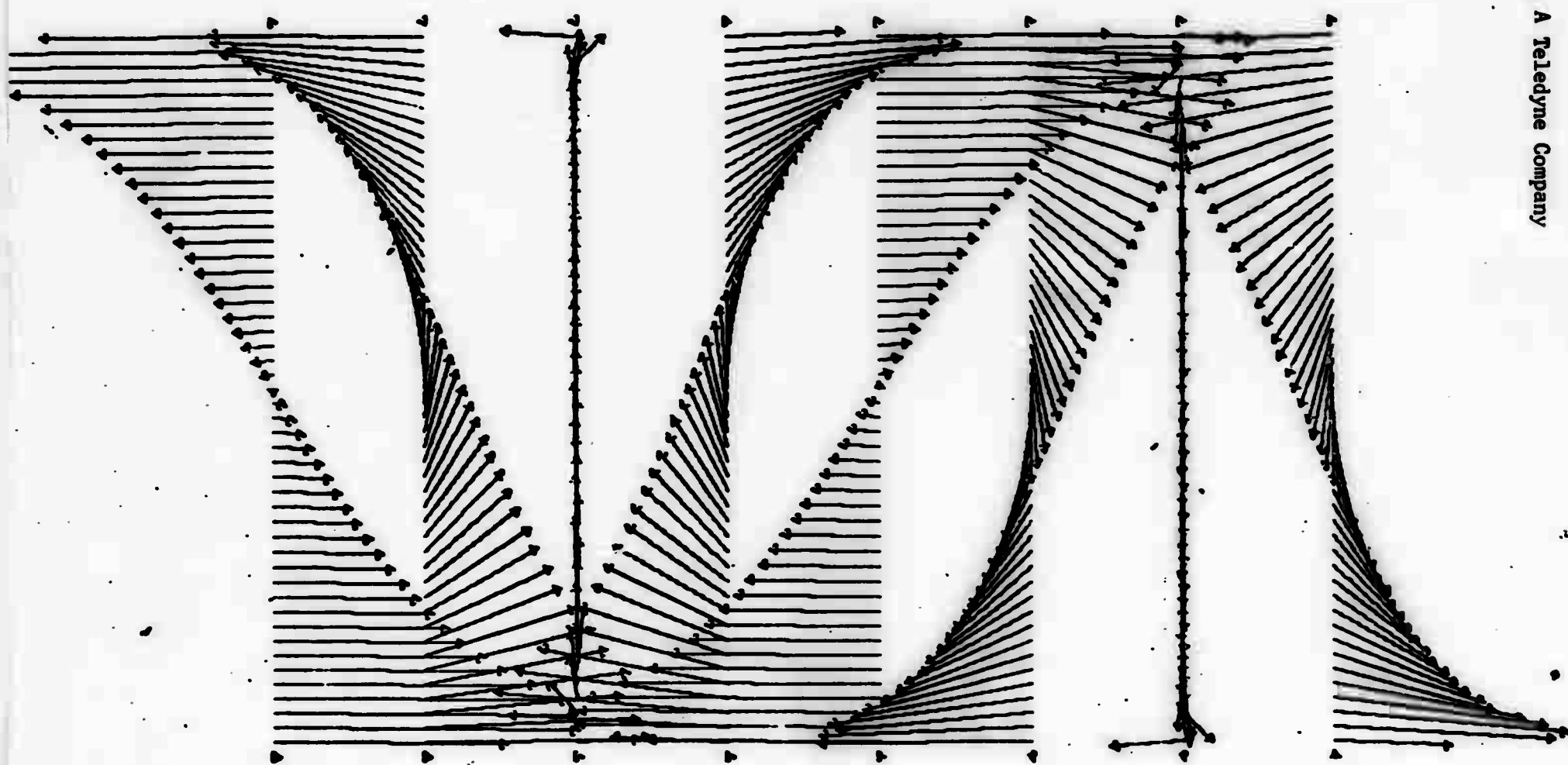


FIGURE 3.4 Velocity field for the first Tollmien-Schlichting wave mode  
 $\alpha = 1.0$ ,  $R = 10^4$ ,  $P = 0.72$ ,  $J = 0.005$ ,  $\omega = 0.237$ ,  $\delta = -0.0039$



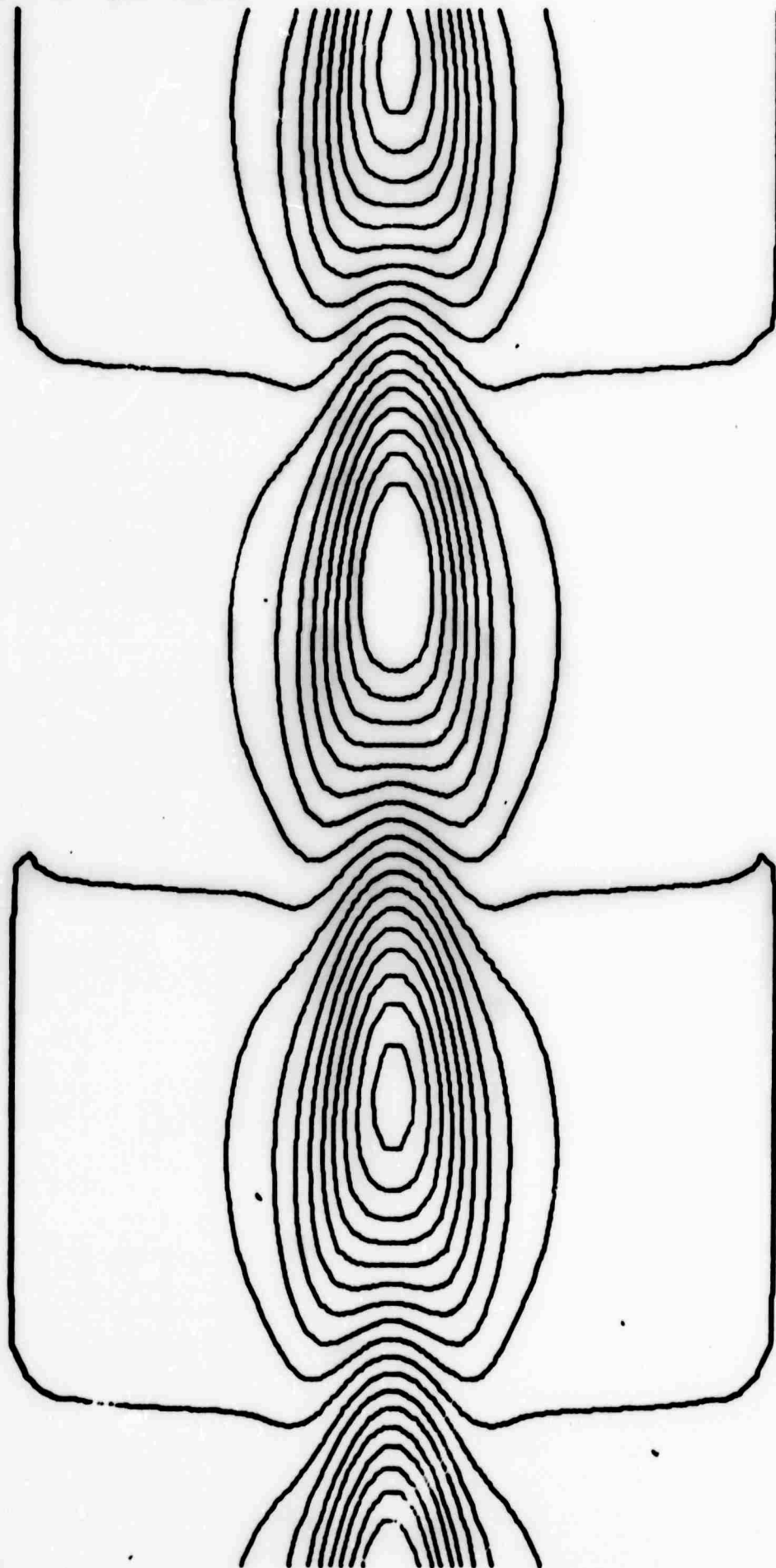


FIGURE 3.5 Streamlines for the first internal gravity wave mode

$\alpha = 1.0$ ,  $R = 10^4$ ,  $P = 0.72$ ,  $J = 0.005$ ,  $\omega = 0.995$ ,  $\delta = 0.0084$



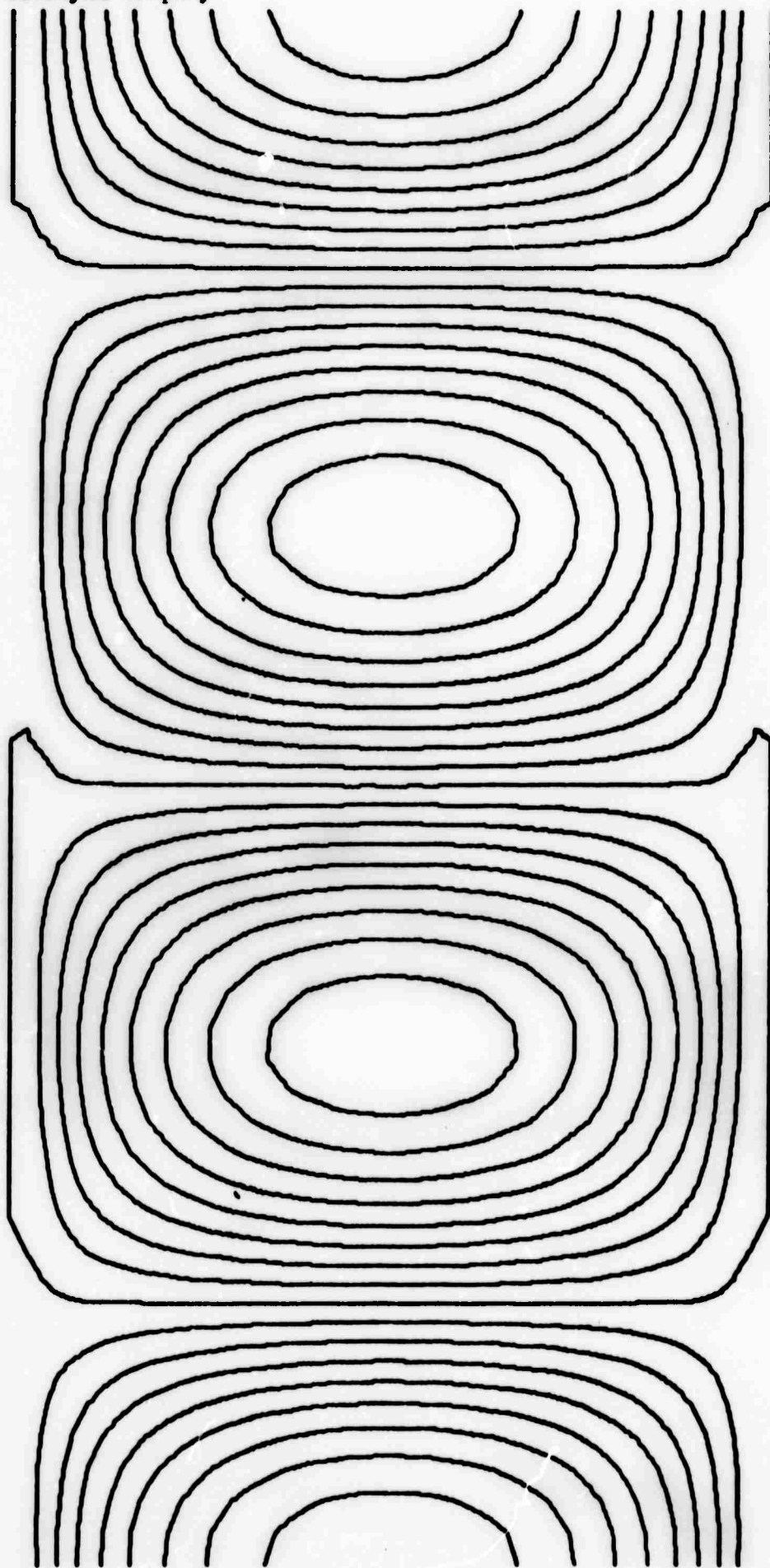


FIGURE 3.6 Streamlines for the first Tollmien-Schlichting wave mode

$\alpha = 1.0$ ,  $R = 10^4$ ,  $P = 0.72$ ,  $J = 0.005$ ,  $\omega = 0.237$ ,  $\delta = -0.0039$



It is clear that the internal gravity wave is largely trapped in the high velocity region at the center of the jet and propagates with a phase velocity very nearly equal to the maximum velocity of this shear flow. The T-S wave, on the other hand, is spread over the entire duct and propagates with a phase velocity less than one-quarter of the maximum shear flow velocity.

There has been a certain amount of controversy over the problem of internal gravity wave propagation in a shear flow. The crucial point is a simple one; in a non-viscous, non-heating conducting stratified fluid the first order perturbation equations are singular at the critical point (the point where the phase velocity of the wave equals the shear flow velocity). Although Drazin and Howard (1966) in their comprehensive review of the stability of parallel flows in inviscid fluid were careful to point out the existence of internal gravity waves and T-S waves in stratified shear flows and to emphasize that the relation of the solutions of the inviscid problem to the solutions of the viscous problem is both complicated and subtle, other authors have not been as careful. One difficulty is that if the fluid is stratified, the inclusion of viscosity does not remove the singularity as it does for a flow in a homogeneous fluid. However, as shown by Koppel (1964), the inclusion of a non-zero thermal conductivity does remove the singularity. This is reasonable since the density stratification is due to a temperature gradient. The equations used here (3.35 and 3.36) are equivalent (with a different notation) to Koppel's final result (Koppel, 1964, eq. 20). It can thus be seen that the amplitude of the motion does not become infinitely large at the critical layer. In the neighborhood of the critical layer the perturbation velocity does reach its maximum but remains finite.



## Teledyne Isotopes

The major results are that this stratified shear flow supports both internal gravity and Tollmien-Schlichting waves; that the internal gravity waves are, roughly, trapped within the layer where  $\bar{U}_{00} > c$ ; and that the phase velocity of the internal gravity modes is approximately equal to the maximum velocity of the shear flow.



#### 4. THEORETICAL SIGNAL PROCESSING

##### 4.1 Estimation and Detection of an Unknown Dispersive Signal Using a Two-Dimensional Array

###### 4.1.1 Introduction

Consider the problem of detecting and estimating an unknown transient signal which is propagating across an extremely large planar array immersed in a waveguide such as the ocean, atmosphere, or the earth's surface. The direction of the propagation and the phase velocity of the signal are unknown, and the noise field is assumed to be Gaussian. In a large system tremendous quantities of data are collected, most of which is noise. The transient signals have a relatively long time between arrivals (such as nuclear events). It is desirable to have a simple procedure for detecting the arrival of a signal, estimating the direction and phase velocities, and upgrading the data. Once the data has been segmented into periods of likely event, the optimal methods can be used to eliminate false alarms and improve the signal estimates.

One also has a reception problem that is not caused by noise. The transmission in the waveguide is dispersive and hence the phase and group velocities depend upon frequency. For signals having a wide bandwidth, it is well known that the usual methods of delay and sum are inadequate for array steering since the signal waveforms are systematically different at different receivers, Figure 4.1. The time alignment at  $t_1$  is incorrect at the time  $t_2$ .

If the signal is modeled as a section of a stationary stochastic process in time and space dimensions, the problem of optimal array processing for non-dispersive signals has been analyzed by several investigators (Faran



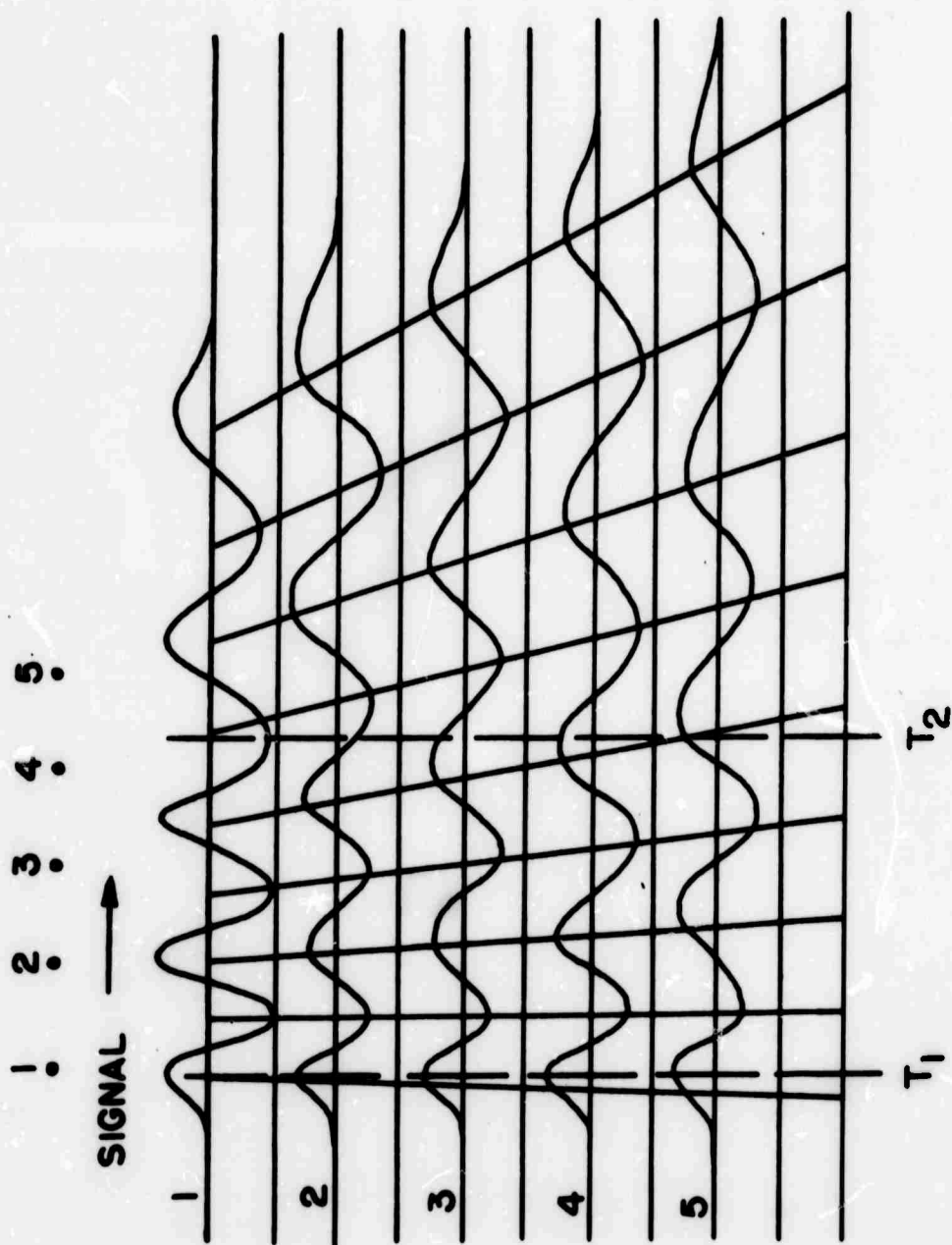


FIG. 4.1 Sketch of Signal Arrivals in a highly dispersive waveguide.



## Teledyne Isotopes

and Hills, 1952; Smith, 1956; Berman and Clay, 1957; Bryn, 1962; Good, 1963; Burg, 1964; and Laster and Linville, 1966). For a non-stochastic non-dispersive signal of unknown waveform, direction, and phase velocity, a type of least-squares estimator has been investigated by Levin (1965). If the phase velocity, direction, and the noise covariance function are known, the ordinary least-squares estimator of the signal is maximum likelihood, linear, unbiased, and minimum variance (Capon, et al., 1967; Graybill, 1961). Levin's estimator is non-linear since it is found by searching over a range of phase velocities and direction cosines. A large amount of computations are required and the optimal array steering and signal processing procedures have been more expensive than delay and sum techniques.

This section presents a relatively simple method for estimating the phase velocity and direction of an unknown plane wave signal. The finite Fourier transform is applied to the output of each sensor and phases of the smoothed frequency components are calculated. These phases are linearly regressed on sensor position to produce estimates of the wave numbers. By appropriate smoothing over frequency and transforming, estimates are obtained of the direction and phase velocity. The precision of estimates depends on the signal-to-noise ratio, the square-root of the number of sensors, and the number of wave lengths which fall in the array. Since the procedure involves Fourier decomposition of the signals, it is easy to include the effect of dispersion across the array.

### 4.1.2 Plane Wave Signal and Noise

Assume that the planar array has  $K$  sensors which are located at positions  $(x_k, y_k)$  with respect to the coordinate axis  $x$  and  $y$  (Figure 4.2). Let  $p_k(t)$  denote the sampled output from the  $k^{\text{th}}$  sensor for  $t = 0, \tau, \dots, (n-1)\tau$ .



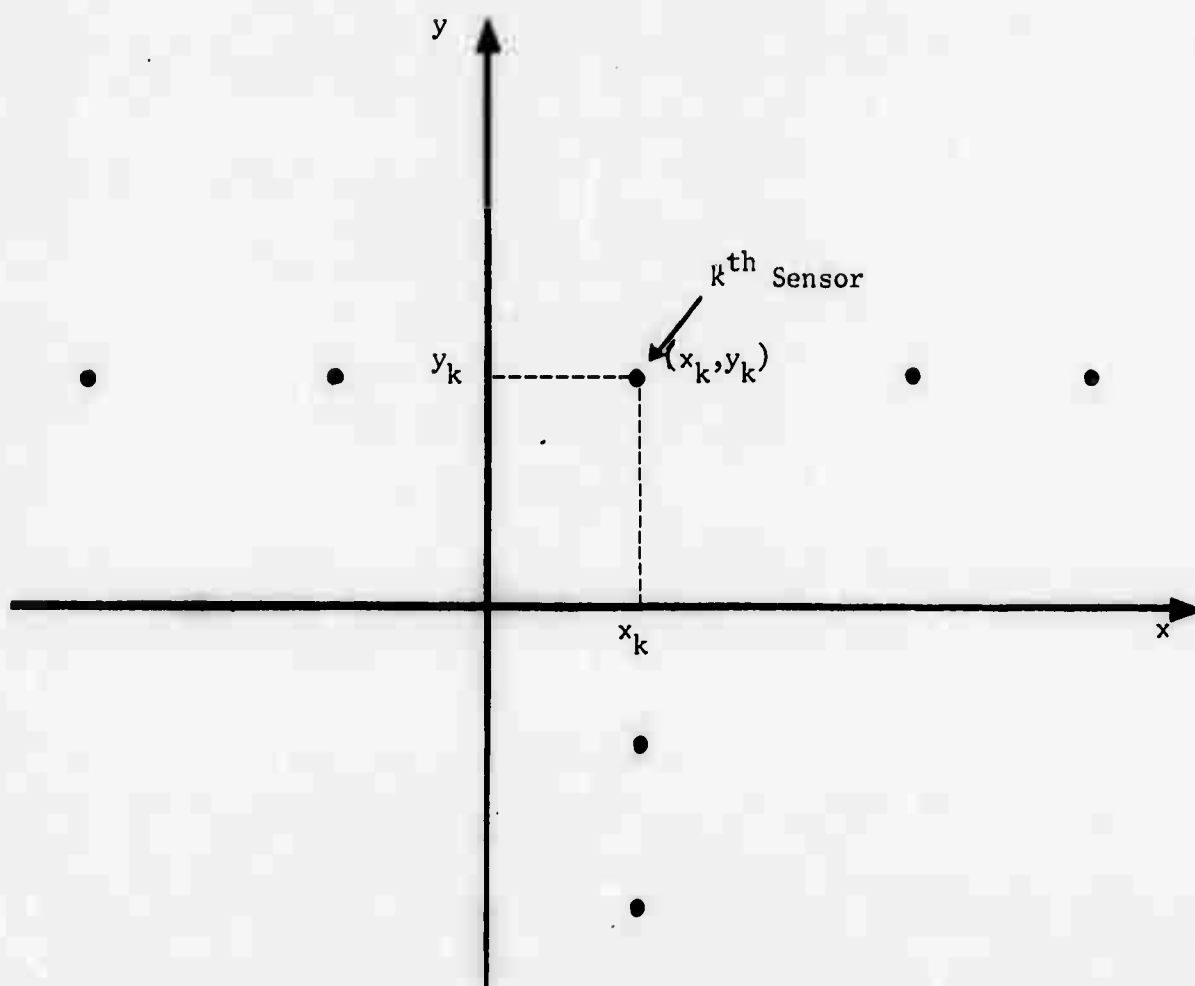


FIGURE 4.2 Coordinate system of array.



## Teledyne Isotopes

Given a sampling interval  $\tau$ , let  $T = n\tau$  denote the total observation period, which is the same for all sensors. When the signal is present, for  $t=0, \tau, \dots, T-\tau$

$$p_k(t) = s \left( t - \frac{x_k \cos \theta + y_k \sin \theta}{v} \right) + n_k(t) \quad (4.1)$$

where  $\theta$  is the direction of propagation and  $v$  is the phase velocity in the  $x$ - $y$  plane. The noise at the  $k^{\text{th}}$  sensor,  $n_k(t)$ , is assumed to be stationary, Gaussian, zero mean, and such that the expected value  $E[n_k(t)n_{k'}(t)] = 0$  for  $k \neq k'$ , i.e., the noise is incoherent.

If the duration of the signal is about the same as the observation period  $T$  seconds, then the signal can be modeled as a plane wave which has the following finite Fourier series representation at  $(x_k, y_k)$ : For  $t=0, \tau, \dots, T-\tau$

$$s(t - \alpha x_k - \beta y_k) = \sum_{j=0}^{n-1} S(\omega_j) e^{i\omega_j(t - \alpha x_k - \beta y_k)} \quad (4.2)$$

where  $\omega_j = \frac{2\pi j}{T}$ , and  $\alpha(\omega) = \frac{\cos \theta}{v(\omega)}$  and  $\beta(\omega) = \frac{\sin \theta}{v(\omega)}$  are the wave slowness components in the  $x$  and  $y$  directions. For a given  $j$ ,  $S(\omega_j)$  is the complex amplitude of the  $\omega_j^{\text{th}}$  frequency component of the signal measured at  $(0,0)$ , the origin of the coordinate system. Since  $s(t)$  is real,  $S(\omega_{n-j}) = S^*(\omega_j)$ , where the star denotes complex conjugate. The folding frequency is  $\frac{1}{2}\tau$  Hz.

Let  $P_k(\omega_j)$  be the  $j^{\text{th}}$  Fourier coefficient of  $P_k(t)$ , i.e., for  $n = T/\tau$

$$P_k(\omega_j) = \frac{1}{n} \sum_{m=0}^{n-1} p_k(m\tau) e^{i\omega_j m\tau} .$$



From (4.1) and (4.2) it follows that for each  $k = 1, \dots, K$  and  $J = 0, \dots, n/2-1$

$$P_k(\omega_j) = |S(\omega_j)| e^{i[\omega_j(\alpha_k + \beta y_k) + \psi(\omega_j)]} + N_k(\omega_j) = |P_k| e^{i\phi_k} \quad (4.3)$$

where  $\psi(\omega_j)$  is the phase of the  $j^{\text{th}}$  Fourier component of the signal at the origin, and  $N_k(\omega_j)$  is the  $j^{\text{th}}$  Fourier coefficient of  $n_k(t)$ . Letting  $\sigma_k^2(\omega)$  denote the power spectrum of  $n_k(t)$ , it can be shown that  $N_k(\omega)$  has a mean value of zero and

$$E(|N_k(\omega)|^2) \approx \frac{1}{T} \sigma_k^2(\omega) \quad (4.4)$$

for large  $T$ , i.e., the  $j^{\text{th}}$  coefficient in the discrete Fourier representation of a section of a stationary random process is a random variable whose mean value is zero and whose variance is the area under the power spectrum in a narrow band of bandwidth  $1/T$  Hz centered at the frequency  $j/T$  Hz (Hinich and Clay, 1968). Moreover,  $N_k(\omega_j)$  and  $N_k(\omega_{j'})$  are approximately uncorrelated for  $j \neq j'$ . The approximations are exact statements if the process is white.

The complex Fourier coefficients  $P_k(\omega_j)$  are obtained by taking the finite Fourier transform of the sections of the sensor outputs  $p_k(t)$ ,  $0 \leq t \leq T$ . The fast Fourier transform (Cooley, Lewis and Welch, 1967) is an algorithm which provides efficient computer calculation of the discrete Fourier coefficients. These complex coefficients will contain the phase characteristics of the signal.



## Teledyne Isotopes

### 4.1.3 Signal Processing

Compute the  $P_k(\omega_j)$  for frequencies  $\omega_j$  such that  $S(\omega_j) \gg 0$ .

For each sensor  $k$ , compute

$$\varphi_k(\omega_j) = \tan^{-1} \frac{\text{Im}P_k(\omega_j)}{\text{Re}P_k(\omega_j)} \quad (4.5a)$$

for  $0 \leq \omega_j < \pi/\tau$ , provided that the imaginary part of  $P_k$ ,  $\text{Im}P_k$ , is smaller in magnitude than  $\text{Re}P_k$ , the real part of  $P_k$ . If  $|\text{Re}P_k| < |\text{Im}P_k|$ , then let

$$\varphi_k(\omega_j) = \frac{\pi}{2} - \tan^{-1} \frac{\text{Re}P_k(\omega_j)}{\text{Im}P_k(\omega_j)} \quad (4.5b)$$

For large  $T$  it can be shown by Taylor series expansion of  $\varphi_k$  as a function of  $N_k$  (Brownlee, 1965) that the phase of  $P_k(\omega)$  can be written

$$\varphi_k(\omega) = \omega[\alpha(\omega)x_k + \beta(\omega)y_k] + \psi(\omega) + \epsilon_k(\omega) \quad (4.6)$$

where  $\epsilon_k(\omega)$  is a Gaussian random variable whose expected value is  $E[\epsilon_k(\omega)] = 0(T^{-1})$  and whose variance is

$$E[\epsilon_k^2(\omega)] = \frac{\sigma_k^2(\omega)}{2T|S(\omega)|^2} \quad (4.7)$$

since  $\text{Re}P_k$  and  $\text{Im}P_k$  are uncorrelated.



## Teledyne Isotopes

Since arctan is a multiple valued function,  $\varphi(\omega)$  is defined only up to an added factor of  $2\pi m$ . One can determine  $m$  by starting at low frequencies, that is if given  $\omega$ ,  $|(x_{k+1}-x_k)\cos \theta + (y_{k+1}-y_k)\sin \theta| < \frac{\lambda(\omega)}{2}$  where  $\lambda(\omega)$  is the wavelength of the  $\omega$ th frequency component, then

$$|\varphi_{k+1}-\varphi_k| < \pi + |\epsilon_{k+1}-\epsilon_k|$$

and thus there is no problem determining the proper integer multiple of  $2\pi$  for each  $k$  provided that  $\sigma_k(\omega)$  TS  $(\omega)$  is small. For an orthogonal array it is sufficient to have the minimum distance between sensors to be less than  $\lambda/2$ . For short wavelengths, it may be necessary to break the array into smaller subarrays and then the estimates of  $\theta$  and wave slowness derived from the subarrays can be averaged. These estimates can then be used to estimate the proper integer multiple of  $2\pi$  for each sensor phase. This procedure for determining the  $m$ 's requires more processing time and thus if it is necessary to use it, the least-squares search procedure for estimating direction and velocity will probably be at least as efficient as the method discussed in this section. However, our method can deal with dispersion whereas the least-squares method cannot unless the dispersion effect is known in detail.

Let  $\varphi(\omega)$  be the  $K$  dimensional vector defined by  $\varphi(\omega)' = [\varphi_1(\omega), \dots, \varphi_K(\omega)]$  and let  $\epsilon(\omega)$  be the vector  $\epsilon(\omega)' = [\epsilon_1(\omega), \dots, \epsilon_K(\omega)]$  where the prime denotes the transpose. Let  $\gamma(\omega)$  be the vector of parameters  $\gamma(\omega)' = (\omega\alpha, \omega\beta, \psi)$  and let  $A$  be the  $K \times 3$  matrix



$$A = \begin{pmatrix} x_1 & y_1 & 1 \\ \vdots & \vdots & \vdots \\ x_K & y_K & 1 \end{pmatrix} \quad (4.8)$$

Writing the system of equations defined by (4.6) in vector and matrix form,

$$\varphi(\omega) = A\gamma(\omega) + \epsilon(\omega) \quad (4.9)$$

Letting  $\Sigma$  denote the  $K \times K$  diagonal matrix whose  $k$ th diagonal element is  $\frac{1}{2T}\sigma_k^2(\omega)$ , the weighted least-squares estimator of  $\gamma$  is

$$\hat{\gamma}(\omega) = (A'\Sigma^{-1}A)^{-1}A'\Sigma^{-1}\varphi(\omega) \quad (4.10)$$

where  $\hat{\gamma}(\omega)' = (\hat{\omega}\alpha, \hat{\omega}\beta, \hat{\gamma})$  and  $\hat{\gamma}$  indicates the estimate of  $\gamma$ . Since  $E(\epsilon)$  is of the order of  $T^{-1}$ , it can be shown that

$$E(\hat{\gamma}) = \gamma + O\left(\frac{1}{KT}\right) \quad (4.11)$$

The linear estimator  $\hat{\gamma}$  is optimal for the system given by (4.9) (Deutch, 1965). In addition to the estimates of wave slowness and signal phase, it is possible to obtain an unbiased estimate of the signal energy  $|S(\omega)|^2$ . From (4.4) and the fact that the expected values of  $\text{Re}N_k$  and  $\text{Im}N_k$  are zero, by the law of large numbers it follows for large  $KT$  that

$$\frac{1}{K} \sum_{k=1}^K |p_k(\omega)|^2 \approx |S(\omega)|^2 + \frac{1}{KT} \sigma_k^2(\omega)$$



## Teledyne Isotopes

Thus

$$|\hat{S}(\omega)|^2 = \frac{1}{K} \sum_{k=1}^K [ |P_k(\omega)|^2 - \frac{1}{T} \sigma_k^2(\omega) ] \quad (4.12)$$

is an approximately unbiased and consistent estimator of  $|S(\omega)|^2$ .

The covariance matrix of  $\hat{\gamma}$  is given by

$$E[(\hat{\gamma} - \gamma)(\hat{\gamma} - \gamma)'] = |S(\omega)|^{-2} (A' \Sigma^{-1} A)^{-1} . \quad (4.13)$$

In order to simplify the above expressions, let us restrict ourselves to the case when the noise at the  $k$ th sensor is white over the band where there is appreciable signal energy, i.e., for each  $k=1, \dots, K$

$$\sigma_k^2(\omega) = \sigma_k^2 \quad \text{if} \quad S(\omega) \gg 0 . \quad (4.14)$$

Further, let us choose the origin of the coordinate system such that

$$\sum_{k=1}^K \frac{x_k}{\sigma_k^2} = \sum_{k=1}^K \frac{y_k}{\sigma_k^2} = 0 . \quad (4.15)$$

Then from (4.8), (4.10), (4.11), and (4.14), we have the following unbiased (of order  $\frac{1}{KT}$ ) estimators of  $\alpha$ ,  $\beta$ , and  $\Psi$ :



# Teledyne Isotopes

$$\hat{\alpha}(\omega) = (\omega D)^{-1} \left[ \left( \sum_{k=1}^K \sigma_k^{-2} y_k^2 \right) \left( \sum_{k=1}^K \sigma_k^{-2} x_k \varphi_k \right) - \left( \sum_{k=1}^K \sigma_k^{-2} x_k y_k \right) \left( \sum_{k=1}^K \sigma_k^{-2} y_k \varphi_k \right) \right] \quad (4.16a)$$

$$\hat{\beta}(\omega) = (\omega D)^{-1} \left[ \left( \sum_{k=1}^K \sigma_k^{-2} x_k^2 \right) \left( \sum_{k=1}^K \sigma_k^{-2} y_k \varphi_k \right) - \left( \sum_{k=1}^K \sigma_k^{-2} x_k y_k \right) \left( \sum_{k=1}^K \sigma_k^{-2} x_k \varphi_k \right) \right] \quad (4.16b)$$

where

$$D = \left( \sum_{k=1}^K \sigma_k^{-2} x_k^2 \right) \left( \sum_{k=1}^K \sigma_k^{-2} y_k^2 \right) - \left( \sum_{k=1}^K \sigma_k^{-2} x_k y_k \right)^2$$

and

$$\hat{\Psi}(\omega) = \left( \sum_{k=1}^K \sigma_k^{-2} \right)^{-1} \sum_{k=1}^K \sigma_k^{-2} \varphi_k \quad (4.17)$$

Note that these estimators are linear functions of the  $\varphi_k$  and that the linear coefficients do not depend on  $\omega$ .

The following expressions for the variances of  $\hat{\alpha}$  and  $\hat{\beta}$  and the covariances can be derived from (4.13):

$$V(\hat{\alpha}) = \frac{\sum_{k=1}^K \sigma_k^{-2} y_k^2}{2T\omega^2 |S(\omega)|^2 D} \quad (4.18a)$$

$$V(\hat{\beta}) = \frac{\sum_{k=1}^K \sigma_k^{-2} x_k^2}{2T\omega^2 |S(\omega)|^2 D} \quad (4.18b)$$



$$\text{COV } (\hat{\alpha}, \hat{\beta}) = - \frac{\sum_{k=1}^K \sigma_k^{-2} x_k y_k}{2T\omega^2 |S(\omega)|^2 D} \quad (4.18c)$$

and

$$\text{COV } (\hat{\alpha}, \hat{\psi}) = \text{COV } (\hat{\beta}, \hat{\psi}) = 0 \quad (4.18d)$$

The variance of  $\hat{\psi}$  is

$$V(\hat{\psi}) = \frac{\left( \sum_{k=1}^K \sigma_k^{-2} \right)^{-1}}{2T |S(\omega)|^2} \quad (4.19)$$

In order to better understand the above estimators and their properties, let us consider an example. Let  $\sigma_k^2 = \sigma^2$  for each  $k = 1, \dots, K$ . Let the array have a cross configuration with equal spacing of distance  $d$  between the sensors in each wing of the cross, and let there be exactly  $N$  sensors in each arm (Figure 4.3). Assuming there is no sensor in the middle,  $K = 2N$  and the distance across the array is  $Nd$ . Let the origin of the coordinate system be located at the middle and let the arms be the  $x$  and  $y$  axis. Then

$$\sum_{k=1}^K x_k = \sum_{k=1}^K y_k = \sum_{k=1}^K x_k y_k = 0 \quad (4.20)$$

and

$$\sum_{k=1}^K x_k^2 = \sum_{k=1}^K y_k^2 = 2 \sum_{j=1}^{N/2} j^2 d^2 = \frac{N(N+1)(N+2)}{12} d^2 \quad (4.21)$$



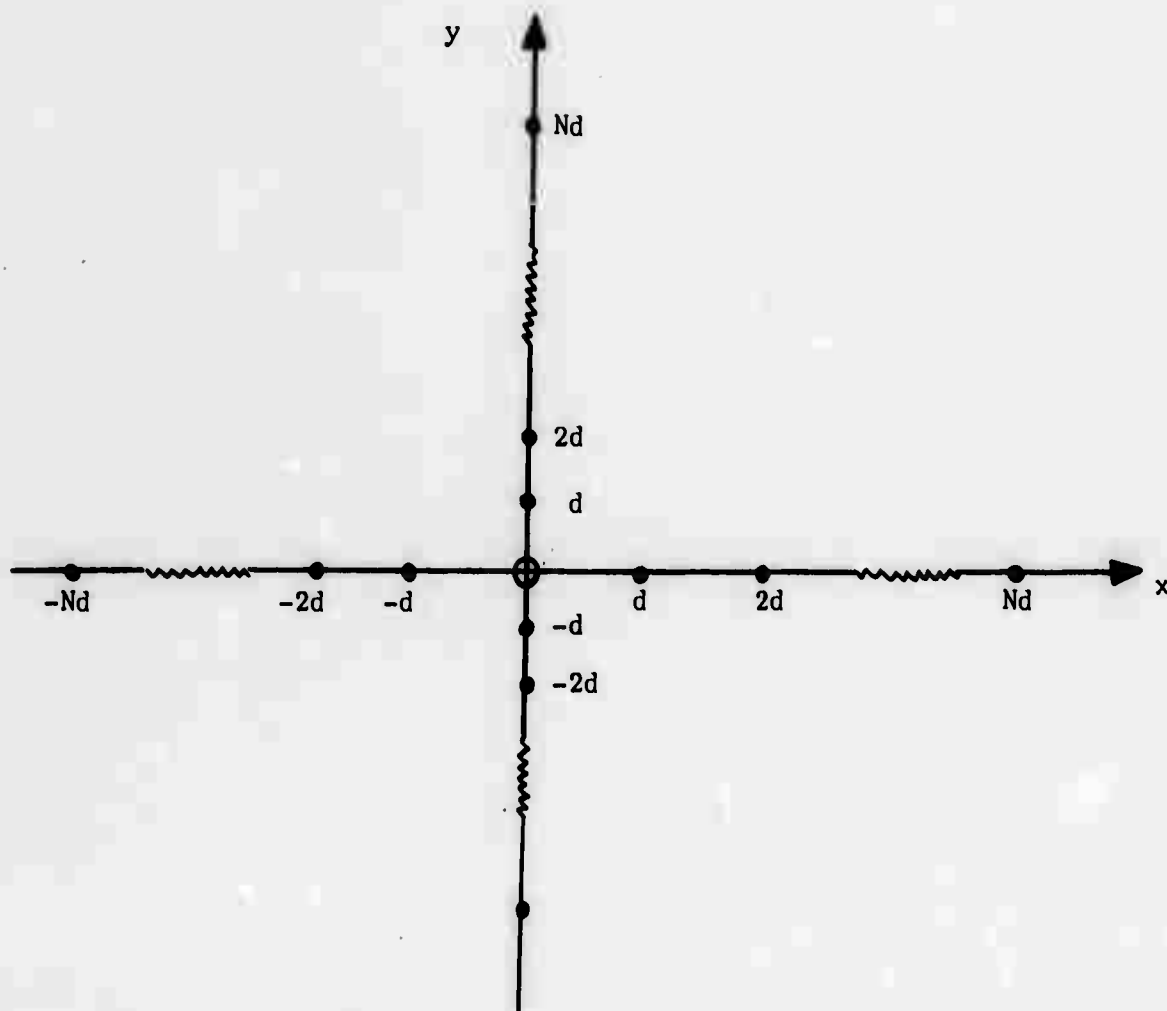


FIGURE 4.3 Cross array with sensors located on coordinate axis.



# Teledyne Isotopes

Since  $\sigma_k^2 = \sigma^2$  for each sensor, (4.20) implies that (4.15) is true, and thus

$$B = \sigma^{-4} \left( \sum_{k=1}^K x_k^2 \right) \left( \sum_{k=1}^K y_k^2 \right)$$

Thus from (4.16),

$$\hat{\alpha}(\omega) = \frac{\sum_{k=1}^K x_k \varphi_k}{\omega \sum_{k=1}^K x_k^2} = \frac{\sum_{j=-N/2}^{N/2} j \varphi_{xj}}{\omega dN (N+1) (N+2)} \quad (4.22a)$$

$$\hat{\beta}(\omega) = \frac{\sum_{k=1}^K y_k \varphi_k}{\omega \sum_{k=1}^K y_k^2} = \frac{\sum_{j=-N/2}^{N/2} j \varphi_{yj}}{\omega dN (N+1) (N+2)} \quad (4.22b)$$

where  $\varphi_{xj}$  is the phase measured at the  $j^{\text{th}}$  sensor on the x-axis arm and  $\varphi_{yj}$  is the phase at the  $j^{\text{th}}$  sensor on the y-axis arm. Moreover from (4.17), the estimator of the signal phase function is

$$\hat{\psi}(\omega) = \frac{1}{K} \sum_{k=1}^K \varphi_k = \frac{1}{2N} \sum_{j=-N/2}^{N/2} (\varphi_{xj} + \varphi_{yj}) \quad (4.23)$$



# Teledyne Isotopes

From (4.18) and (4.19) the variances and covariances of  $\hat{\alpha}$ ,  $\hat{\beta}$ , and  $\hat{\psi}$  are

$$v(\hat{\alpha}) = \frac{6 \sigma^2}{T \omega^2 |S(\omega)|^2 N (N+1) (N+2) d^2} = v(\hat{\beta}), \quad (4.24)$$

$$\text{COV}(\hat{\alpha}, \hat{\beta}) = \text{COV}(\hat{\alpha}, \hat{\psi}) = \text{COV}(\hat{\beta}, \hat{\psi}) = 0 \quad (4.25)$$

and

$$v(\hat{\psi}) = \frac{\sigma^2}{2KT |S(\omega)|^2} \quad (4.26)$$

Approximating  $N(N+1)(N+2)$  by  $N^3$  in equation (4.24), and since the wavelength of the  $\omega^{\text{th}}$  frequency is

$$\lambda(\omega) = \frac{2\pi v(\omega)}{\omega},$$

$$\lambda_x = \lambda / \cos \theta$$

$$\lambda_y = \lambda / \sin \theta$$

it follows that the proportional standard deviation of  $\hat{\alpha}$  is

$$\frac{SD(\hat{\alpha})}{\alpha} = \left( \sqrt{\frac{KT}{3}} \frac{\pi |S(\omega)|}{\sigma} \frac{x \cos \theta}{\lambda} \right)^{-1} \quad (4.27)$$

provided that  $\theta \neq \frac{\pi}{2}$  or  $\frac{3\pi}{2}$ . Thus the proportional standard deviation of the estimate of the x-axis component of wave slowness depends inversely on  $\sqrt{K}$ , the signal to noise ratio  $|S(\omega)|/\sigma$ , and  $Nd/\lambda_x$ , the number of wavelengths lying within the length of the x-axis arm of the array. Clearly



the proportional standard deviation is undefined for  $\theta = \frac{\pi}{2}$  or  $\frac{3\pi}{2}$  since  $\alpha = 0$ . A similar result holds for  $SD(\hat{\beta})/\beta$  with  $\lambda \sin \theta$  replacing  $\lambda \cos \theta$ . We have shown that the best estimate of the velocity is obtained from an array arm along the direction of propagation of the signal.

#### 4.1.4 Estimation of Direction and Dispersion

Let  $n_s$  denote the number of  $\omega_j > 0$  such that  $S(\omega_j) \gg 0$ , i.e., if the signal is narrow-band then  $n_s/T$  Hz is the bandwidth. Let the estimator of signal direction be defined by

$$\hat{\theta} = \tan^{-1} \frac{1}{n_s} \sum_{\omega_j} \frac{\hat{\beta}(\omega_j)}{\hat{\alpha}(\omega_j)}, \quad (4.28)$$

Where the sum is taken over the  $\omega_j$  which defines  $n_s$ , if the term in the bracket is less than one. If the term in the bracket, i.e., the average ratio of  $\hat{\beta}$  to  $\hat{\alpha}$ , is greater than one, define  $\hat{\theta}$  in terms of the arccot as in (4.5b).

By Taylor series expansion of (4.28), it follows from (4.11) and (4.18) that the expected value of  $\hat{\theta}$  is

$$E(\hat{\theta}) = \theta + O\left(\frac{1}{KT}\right) \quad (4.28a)$$

and the variance is

$$V(\hat{\theta}) = \frac{(\sin \theta \cos \theta)^2}{n_s^2} \sum_{\omega_j} \left[ \frac{V(\hat{\alpha})}{\alpha^2} + \frac{2\text{COV}(\hat{\alpha}, \hat{\beta})}{\alpha\beta} + \frac{V(\hat{\beta})}{\beta^2} \right] \quad (4.28b)$$



## Teledyne Isotopes

For the cross array example,

$$V(\hat{\theta}) = \frac{12\sigma^2}{KTn_s(Nd)^2} \sum_{\omega_j} \frac{\lambda^2(\omega)}{4\pi^2 |S(\omega)|^2} \quad (4.30)$$

If the signal is narrow-band with amplitude  $S$ , then the standard deviation of  $\hat{\theta}$  is

$$SD(\hat{\theta}) = \left( \sqrt{\frac{KT}{3}} \frac{\pi S}{\sigma} \frac{Nd}{\lambda_0} \right)^{-1} \quad (4.31)$$

where  $\lambda_0$  is the average wavelength of the band. These results are similar to the ones obtained by Levin for the least-squares processor (Levin, 1965).

In order to measure the signal dispersion, let us assume that the wave slowness  $\delta(\omega)$  is approximately linear in  $\omega$  for the frequency range of interest, i.e.,

$$\delta(\omega) = \sqrt{\alpha^2 + \beta^2} = \delta_0 + \delta_1 \omega \quad (4.32)$$

Further assume that  $\sum_k \sigma_k^{-2} x_k^2 = \sum_k \sigma_k^{-2} y_k^2$  and  $\sum_k \sigma_k^{-2} x_k y_k = 0$ , and thus from (4.18),  $V(\hat{\alpha}) = V(\hat{\beta})$  and  $COV(\hat{\alpha}, \hat{\beta}) = 0$ . Defining

$$\hat{\delta}(\omega) = \sqrt{\hat{\alpha}^2 + \hat{\beta}^2},$$

it then follows that the variance of  $\hat{\delta}$  is

$$V(\hat{\delta}) = \frac{1}{2T\omega^2 |S(\omega)|^2 \sum_k \sigma_k^{-2} x_k^2} \quad (4.33)$$

and  $E(\hat{\delta}) = \delta + O(T^{-1})$ .



# Teledyne Isotopes

For  $\omega_j$  such that  $S(\omega)_j \gg 0$ , let  $h(\omega) = \omega^2 |S(\omega)|^2$  and define

$$H_0 = \sum_j h(\omega_j) \quad H_1 = \sum_j \omega_j h(\omega_j)$$

$$H_2 = \sum_j \omega_j^2 h(\omega_j) = \sum_j \omega_j^4 |S(\omega_j)|^2.$$

Then from (4.33), the optimal weighted least-squares estimators of  $\delta_0$  and  $\delta_1$  are

$$\hat{\delta}_0 = \frac{H_2 \sum_j h(\omega_j) \hat{\delta}(\omega_j) - H_1 \sum_j \omega_j h(\omega_j) \hat{\delta}(\omega_j)}{H_0 H_2 - H_1^2}$$

and

$$\hat{\delta}_1 = \frac{H_0 \sum_j h(\omega_j) \hat{\delta}(\omega_j) - H_1 \sum_j \omega_j h(\omega_j) \hat{\delta}(\omega_j)}{H_0 H_2 - H_1^2}$$

where the variances and the covariance are

$$V(\hat{\delta}_0) = \frac{\pi H_2}{T(H_0 H_2 - H_1^2) \sum_k \sigma_k^{-2} x_k^2},$$

$$V(\hat{\delta}_1) = \frac{H_0}{H_2} V(\hat{\delta}_0),$$

and

$$\text{COV}(\hat{\delta}_0, \hat{\delta}_1) = -\frac{H_1}{H_2} V(\hat{\delta}_0).$$

Thus for the cross array given a narrow-band signal with center frequency  $\omega_0$ ,



$$\frac{SD(\hat{\delta}_0)}{\hat{\delta}_0} = \frac{\omega_0 SD(\hat{\delta}_1)}{\hat{\delta}_1} = \left( \sqrt{\frac{KT}{3}} \frac{\pi S}{\sigma} \frac{Nd}{\lambda_o} \right)^{-1} \quad (4.34)$$

Thus the proportional standard deviation of  $\hat{\delta}_1$  is  $\omega_0^{-2}$  times the proportional standard deviation of  $\hat{\delta}_0$ , which implies that the precision of the estimate of  $\delta_1$  is less for low frequency narrow-band signals.

#### 4.1.5 Signal Detection

The estimator  $\hat{\delta}_0$  can be used to detect the presence of a propagating signal. Given the estimate  $\hat{\delta}_0$  of  $\delta_0$ , the 95% confidence interval for  $\delta_0$  is

$$[\hat{\delta}_0 - 1.96 SD(\hat{\delta}_0), \hat{\delta}_0 + 1.96 SD(\hat{\delta}_0)] \quad (4.35)$$

where  $SD(\hat{\delta}_0)$  is given by (4.34). Since  $\delta_0 \geq 0$ , the signal is detected with "95% confidence" if  $\hat{\delta}_0 > 1.96 SD(\hat{\delta}_0)$ . If the computation required for the estimation of  $\delta_0$  is considered too lengthy, the estimator  $\hat{\delta}(\omega_0)$  can be used to detect the signal, where  $\omega_0$  is the frequency for which the signal to noise ratio is a maximum. The signal is detected with "95% confidence" if  $\hat{\delta}(\omega_0) > 1.96 SD(\hat{\delta})$  where  $SD(\hat{\delta}) = \sqrt{V(\hat{\delta})}$  is given by (4.33).

The estimate  $\hat{\delta}_1$  of  $\delta_1$ , the slope of  $\delta(\omega)$ , can be used to test whether or not there is dispersion in the signal. The 95% confidence interval for  $\delta_1$ , given  $\hat{\delta}_1$ , is

$$[\hat{\delta}_1 - 1.96 SD(\hat{\delta}_1), \hat{\delta}_1 + 1.96 SD(\hat{\delta}_1)] ,$$

and thus if zero lies in this interval, the data indicates that there is no dispersion.



## Teledyne Isotopes

### 4.2 Cophase: An Ad-Hoc Array Processor

#### 4.2.1 Introduction

"Cophase" is an ad hoc statistic characterizing signal strength as a function of velocity and direction, for data from an array of detectors receiving propagating signal(s) and uncorrelated noise. The definition of cophase is:

$$C(V, \theta) = \frac{\sum_{n=N_1}^{N_2} \sum_{j=k+1}^K \sum_{k=1}^{K-1} \left( A_j(\omega_n) + A_k(\omega_n) \right) \cos \left[ (\phi_j^F - \phi_k^F) - (\phi_j^V - \phi_k^V) \right]}{\sum_{n=N_1}^{N_2} \sum_{j=k+1}^K \sum_{k=1}^{K-1} \left( A_j(\omega_n) + A_k(\omega_n) \right)}$$

where:

$V$  is the assumed phase velocity;

$\theta$  is the assumed azimuth from which signal arrives;

$n$  is the index of frequency (frequencies in the band from the  $N_1$ th to the  $N_2$ th harmonic are used);

$j$  is the station number (there are  $K$  stations)

$\omega_n$  is the  $n$ 'th frequency

$A_j(\omega_n)$  is the  $n$ 'th Fourier amplitude at the  $j$ 'th detector

$\phi_j^F$  is the  $n$ 'th Fourier phase at the  $j$ 'th detector

$\phi_j^V$  is the phase of the  $n$ 'th frequency, arriving at the  $j$ 'th detector, based on the position of the detector and the assumed values of  $V$  and  $\theta$

Basically,  $C(V, \theta)$  calculates the normalized, weighted sum over all  $\frac{1}{2} K(K-1)$  detector pairs, and over all frequencies, of the cosines of the difference between the Fourier phase differences and the assumed phases differences.



Note that  $C(V, \theta)$  is a statistic with an expectation of 0 if the  $K$  records are non-correlated. It has an expectation of +1.0, if the  $K$  records represent a non-dispersive propagating signal, at the assumed value of  $V$  and  $\theta$  corresponding to the actual velocity and direction of the signal. Its expectation at other assumed  $(V, \theta)$ 's would approach 0 for a very-large-aperture array or for a broadband signal, but may in general have non-zero values (side lobes).

In applying this statistic to signal detection or velocity/direction estimation, the first step will be a Fourier analysis of the  $K$  records; then  $C(V, \theta)$  can be calculated for each point in a grid of velocities and directions. If the value of  $C(V, \theta)$  is sufficiently close to +1.0 for some  $(V, \theta)$ , then a signal has been detected. The point  $(V, \theta)$  at which  $C(V, \theta)$  is at its maximum is an estimate of the corresponding signal parameters. This "cophase" statistical method of detection and parameter estimation does not require a knowledge of the  $\pm 2\pi$  ambiguities in the Fourier phases, or of the origin time of the signal and its source distance.

#### 4.2.2 Distribution under the Null Hypothesis

If "sufficiently close to +1.0" is to be used as a criterion for signal detection, the word "sufficiently" will require a quantitative definition based on the statistical distribution of  $C(V, \theta)$  when the  $\phi_j^F$ 's are uniformly-distributed, independent, random variables (i.e., when the  $K$  records are non-correlated noise). This null hypothesis distribution, calculated numerically, is discussed below for the case in which  $A_j(\omega_n) = 1.0$  for all  $j$  and  $n$ . The extension of these results to  $A$ 's which vary with  $n$  should be trivial; but if the  $A$ 's as well as the  $\phi_j^F$ 's are allowed to vary randomly with  $j$ , the results will require some re-interpretation.



## Teledyne Isotopes

Since there are  $K$  detectors in the array, there will be  $K$  independent values of  $\phi_j^F(\omega_n)$  for each frequency. There are  $\frac{1}{2} K(K-1)$  different values of the term  $(\phi_j^F - \phi_k^F)$ , but only  $K-1$  of these are independent.

The  $K$ -independent  $\phi_j^F(\omega_n)$  are uniformly distributed from 0 to  $2\pi$ . The  $\frac{1}{2} K(K-1)$  differences,  $\phi_j^F - \phi_k^F$ , of which only  $K-1$  are independent, have a triangular probability density function; its maximum,  $1/2\pi$ , is at  $\phi_j^F - \phi_k^F = 0$ , and it decreases linearly to 0 at  $\phi_j^F - \phi_k^F = \pm 2\pi$ . From this distribution of  $\phi_j^F - \phi_k^F$ , it may be calculated that the probability density function for  $\cos(\phi_j^F - \phi_k^F)$  is

$$p \left[ \cos(\phi_j^F - \phi_k^F) \right] = \frac{1}{\pi \sqrt{1 - \cos^2(\phi_j^F - \phi_k^F)}}$$

between  $\pm 1$ , and 0 elsewhere. This function's second moment about its mean is the variance of  $\cos(\phi_j^F - \phi_k^F)$ , where  $\phi_j^F$  and  $\phi_k^F$  are independent random phases uniformly distributed from 0 to  $2\pi$ ; the variance may be shown to be equal to 0.5.

If  $C(\theta, V)$  were defined in such a way that the two inner summations were made over only  $(K-1)$  detector pairs with  $(K-1)$  independent phase differences, the expectation and variance of  $C(\theta, V)$  would be 0 and  $0.5/(K-1)$ , respectively, and  $C(\theta, V)$  would be distributed approximately normally for large  $K$ , under the null hypothesis.

However,  $C(\theta, V)$  is formed by a summation over all  $\frac{1}{2} K(K-1)$  detector pairs. If the  $\frac{1}{2} K(K-1)$  phase differences were independent (but they are not),  $C(\theta, V)$  would have an expectation and variance of 0 and  $0.5/\frac{1}{2} K(K-1)$ , respectively, and  $C(\theta, V)$  would be distributed approximately



normally for large  $K^2$ , under the null hypothesis. If the  $\frac{1}{2} K(K-1)$  phase differences were independent (but they are not),  $C(\theta, V)$  would therefore be a much more powerful statistic than the modified  $C(\theta, V)$  of the last paragraph, in which only  $K-1$  independent phase differences are used at each frequency. Since only  $K-1$  of the  $\frac{1}{2} K(K-1)$  phase differences are actually independent, there is no a priori reason to expect  $C(\theta, V)$  to have a smaller variance than  $0.5/(K-1)$ . As the numerically determined distribution of  $C(\theta, V)$  will show however, its variance is not only smaller than  $0.5/(K-1)$ ; it is actually equal to  $0.5/\frac{1}{2}K(K-1)$ .

Using 16,384 sets of 10 random phases each, the distribution of  $C(V, \theta)$  was computed numerically for  $K = 10$  (10 stations) and  $N_1 = N_2$  (one frequency only), assuming that each detector senses only uncorrelated noise. This null hypothesis distribution is shown in Figure 4.4 by the curve labelled 0.0. This distribution has a variance of 0.011 and a mean of -0.001. The variance is exactly equal to that which we would expect if the  $\frac{1}{2} K(K-1)$  terms in the summation were independent - i.e.,  $0.5/\frac{1}{2}(10)(10-1)$ . It is smaller (and the test is therefore more powerful) by a factor of 5, than if we had used only  $K-1$  independent phase difference from among the  $\frac{1}{2}K(K-1)$ . The distribution is strongly skewed; its cumulative frequency at  $C(V, \theta) = 0$  is 0.68, its maximum is between -0.05 and -0.10, and its mean is -0.001 (but numerical computation errors for the mean may be as large as 0.001).

#### 4.2.3 Distribution under the Alternative Hypothesis

The distribution was re-evaluated assuming that each detector senses signal in addition to the uncorrelated noise, for a number of signal-to-noise amplitude ratios. Several of these are shown in Figure 4.4 along



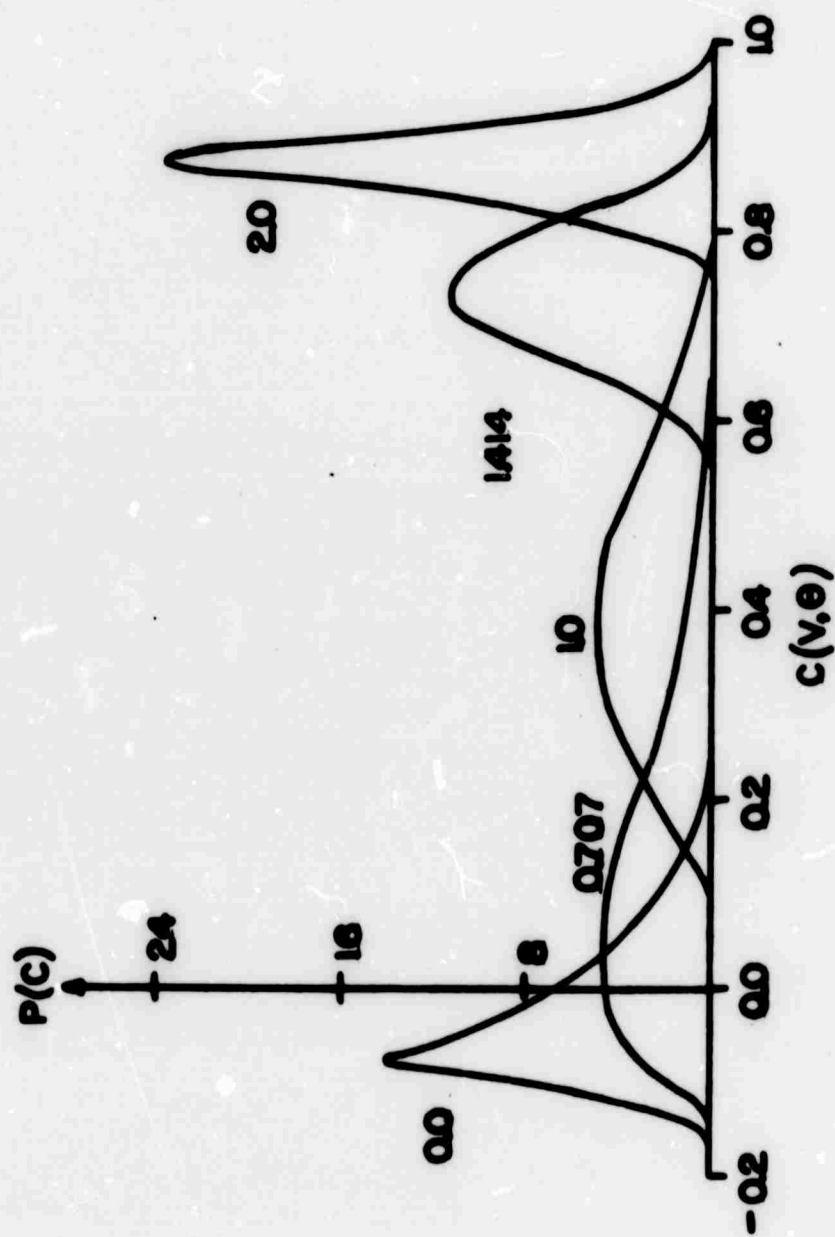


FIG. 4.4 The probability density function of  $C(V, \theta)$ , evaluated at the  $(V, \theta)$  of the signal, using a single frequency, for several signal-to-noise ratios.



with the null hypothesis curve (signal-to-noise ratio of 0.0). As the signal-to-noise ratio passes in excess of 1.0, there is a rapid transition in which the distribution's variance at first increases and then approaches zero, as its mean approaches 1.0.

The curves in Figure 4.4 can be used to estimate  $\alpha$  and  $\beta$ , the probabilities of Type I errors (false alarm) and Type II errors (undetected signal), respectively, and to determine if they are acceptably small. For example, the 97.5 percentile of the 0.0 curve and the 75 percentile of the 1.0 curve are both 0.5. This means that for an  $\alpha$  of 2.5% (acceptably small),  $\beta$  would be 75% (unacceptably risky) if the signal-to-noise ratio is 1.0; but  $\beta$  decreases rapidly to 0.2% as the signal-to-noise ratio increases only slightly to 1.414. Furthermore, if more than one frequency is available for summation, an acceptable value of  $\beta$  is possible for signal-to-noise ratios of less than 1.0. For example, if 16 frequencies are used in the summation ( $N_2 - N_1 = 15$ ), an  $\alpha$  of 2.5% would correspond to a  $\beta$  of 1.0% if the signal-to-noise amplitude were only .707.

#### 4.2.4 Evaluation of the Cophase Technique: Numerical Experiments

To evaluate the cophase technique, numerical experiments were performed using synthesized "signals" and "noise" recorded by a hypothetical array. The array consisted of six elements: three at the midpoints of the 358 km legs of an equilateral triangle, and three at points one-fourth of the distance from each vertex to the next (going anti-clockwise). This configuration was studied by Haubrich (1968), and found to have certain optimum characteristics.

The "signals" were synthesized by assuming that a source generated a Dirac delta-function signal at a distance of 10,000 km due North of the array. The signal propagated dispersively with a phase velocity

$$V(\text{mps}) = 320 - 0.5 \sinh \left( \frac{736f (\text{cycles/min}) - 232}{32} \right)$$



## Teledyne Isotopes

The corresponding group velocity exhibits a maximum at  $f = 232/736$  cycles/min, or a period of slightly more than three minutes. The resultant synthetic signals (Fig. 4.5) are reasonable facsimiles of actual microbarograph records of acoustic-gravity waves from nuclear explosions (Donn and Shaw, 1967).

The 4-hour synthetic signals at the six hypothetical array points were next Fourier analyzed; then their cophase function was calculated using various parts of the signals' spectra, for velocities between 250 and 400 mps, and for  $360^\circ$  of azimuth.

Using only  $N = 97$  (ninety-seventh harmonic - 2.4 minute period) in the frequency summation, the cophase (Fig. 4.6) has a peak at  $(V, \theta) = (320, 0^\circ)$ , corresponding to the actual signal. The peak's amplitude is 0.994 - almost perfect cophase (but not quite; since the signal is dispersive). However, there are several closely-spaced side lobes, the highest of which are 0.976 at  $(V, \theta) = (310, \pm 100^\circ)$ . Since the wavelength at this frequency is one-half the detector spacing, the  $2\pi$  phase errors in the Fourier analysis produces closely spaced side lobes in the cophase function. This phenomenon may also be regarded as a "ringing" in velocity-direction, due to the extreme narrowness of the filter (only one frequency was used). By summing over frequency from  $N = 95$  to  $N = 100$ , the largest side lobe drops in amplitude only to 0.868, since the frequency filter is still extremely narrow. Thus, summing over adjacent frequencies within a very narrow band is not useful in the noise-free case.

Using only  $N = 33$  (7.2 minute period) in the summation (Fig. 4.7) the side lobe reaches a height of 0.997 - the same as the main peak - at  $(V, \theta) = (400, \pm 180^\circ)$ . The large spacing of the lobe from the main peak is consistent with the much larger wavelength.



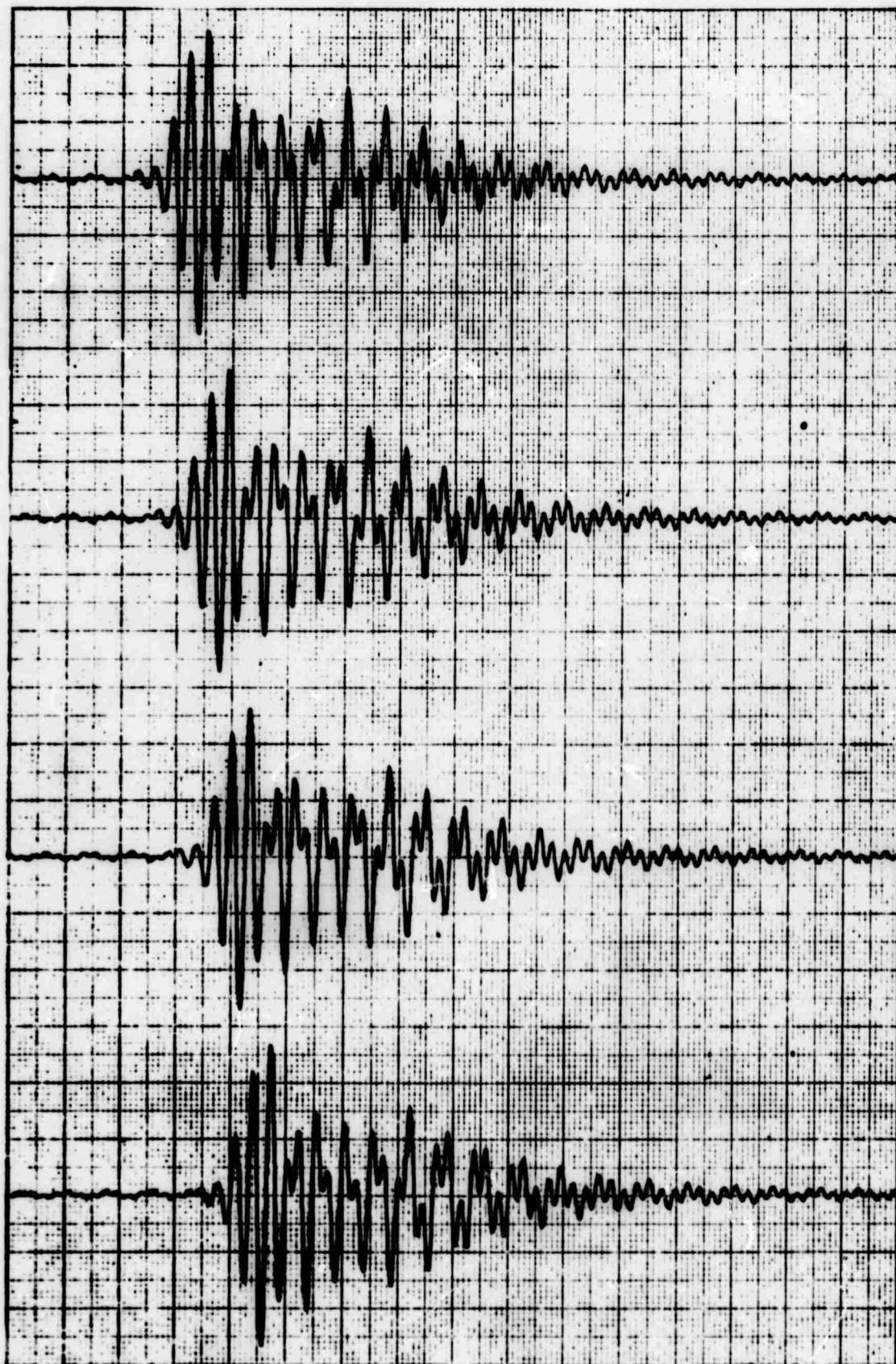


**FIG. 4.5** The four synthetic signals at the six detectors (two pairs of detectors are equidistant from the source and detect identical signals).



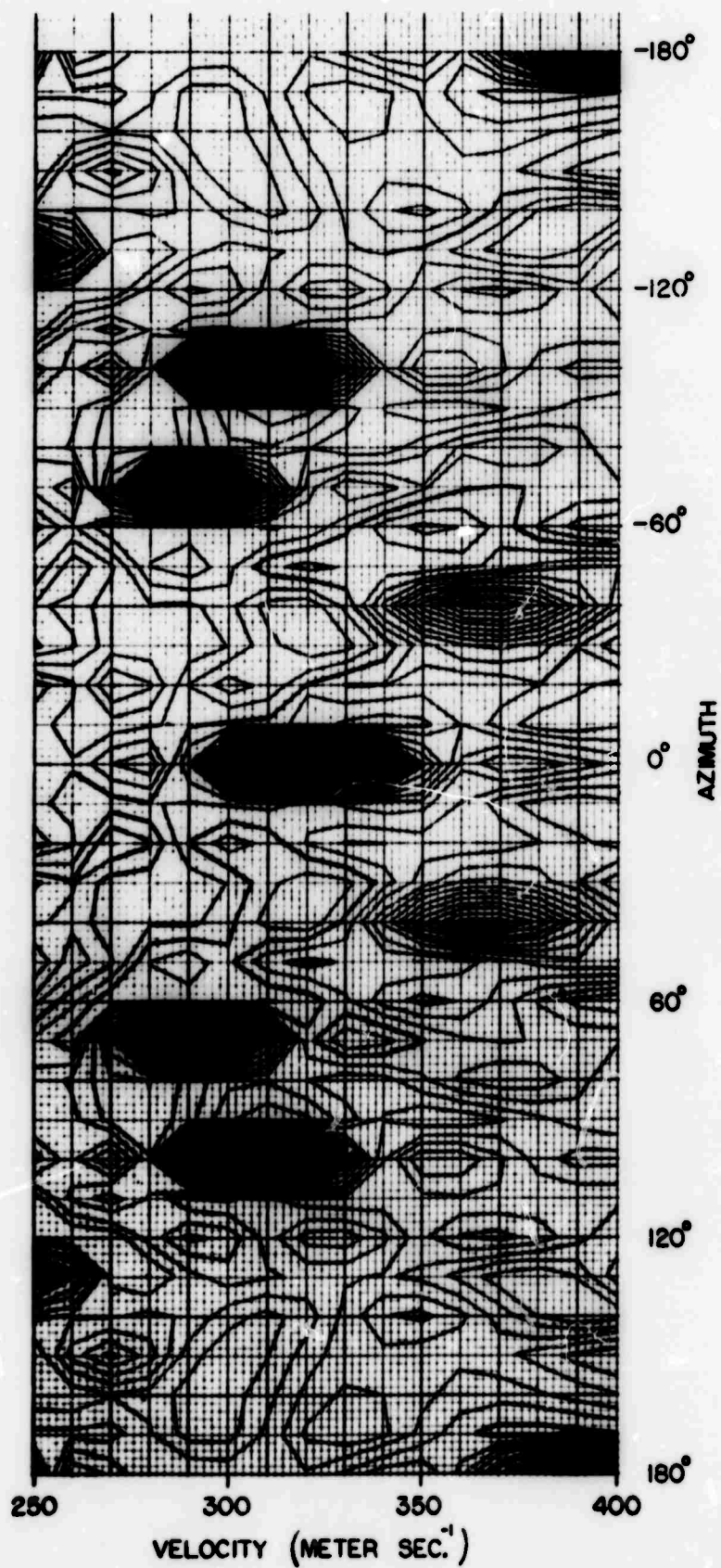


**FIG. 4.6** Cophase of the 2.4 min. component of the synthetic signal detected by the 6-element array.



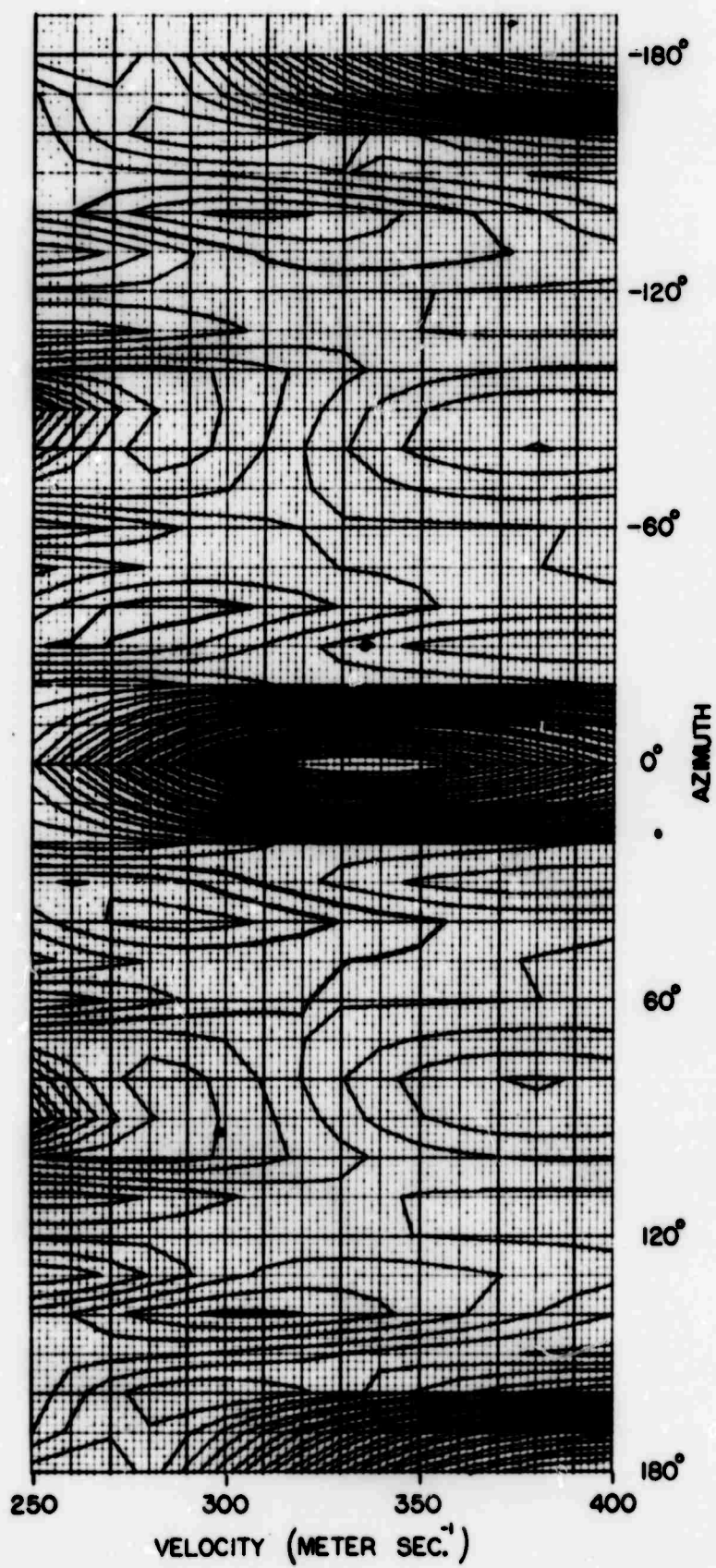


FIG. 4.7 Cophase of the 7.2 min. component of the synthetic signal detected by the 6-element array.



## Teledyne Isotopes

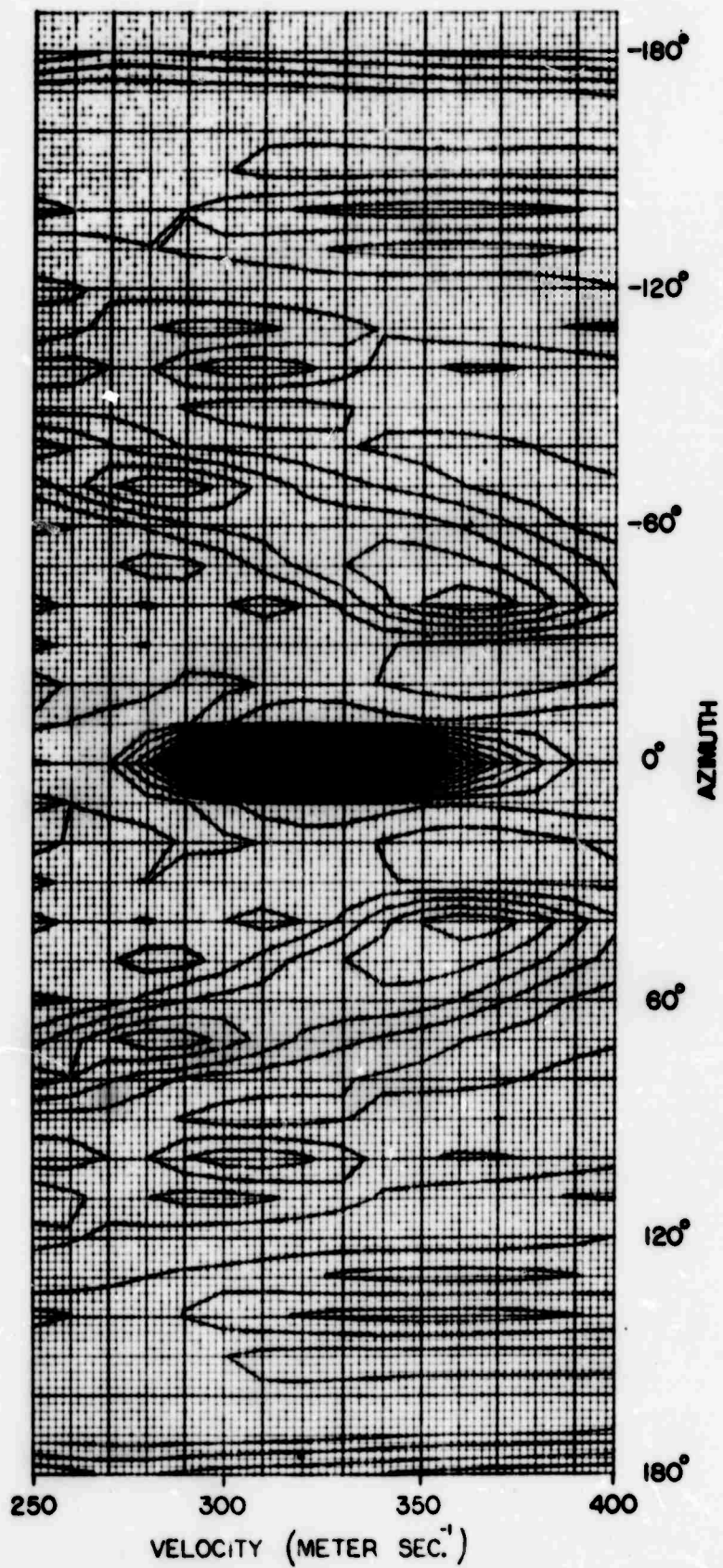
Using  $N = 30$  through  $N = 100$  (Fig. 4.8), the main peak of 0.993 clearly dominates over the region. The highest side lobes are only 0.133, at  $(V, \theta) = 350, \pm 50^\circ$ . The broad band of frequencies integrated provides effective cancellation of the side lobes appearing at different positions in the cophase functions of individual frequencies. The result of using a wide band of frequencies is the high resolution of the high frequencies (Fig. 4.8) combined with even less ambiguity than the low frequencies alone (Fig. 4.7).

When computer-generated noise is added to the set of six synthetic signals, the cophase function begins to degenerate. Figure 4.9 shows the cophase calculated with one frequency ( $N = 50$ ), and a signal-to-noise amplitude ratio of about 0.7. There is no peak at  $(V, \theta) = 320, 0^\circ$ , where the signal should be. There are seven peaks with cophase exceeding 0.4, the highest of which is 0.548. These represent random noise reinforcement, and coincide with neither the signal nor its side lobes.

However, if cophase is recalculated summing over frequency from  $N = 30$  through  $N = 100$ , a peak of 0.402 appears at  $(V, \theta) = 320, 0^\circ$ , corresponding exactly to the signal (Fig. 4.10). In this case, however, the noise is sufficiently cancelled by the summation over 71 frequencies, so the highest peaks beside the signal itself has a cophase of only 0.106 at  $(V, \theta) = 360, -40^\circ$ . The result may be unambiguously interpreted as representing a signal from due north with a phase velocity of 320 mps.

A final pair of numerical experiments were performed to evaluate the use of the cophase method in conjunction with the actual Teledyne-Isotopes array. First, the same signal described above was synthesized for each point in the array. A two-hour sample was analyzed using  $N = 15$  (8 minute period) through  $N = 50$  (2.4 minute period). The result (Fig. 4.11) shows a well-





NOT REPRODUCIBLE

**FIG. 4.8** Cophase of the 2.4 - 8.0 min. band of the synthetic signal detected by the 6-element array.



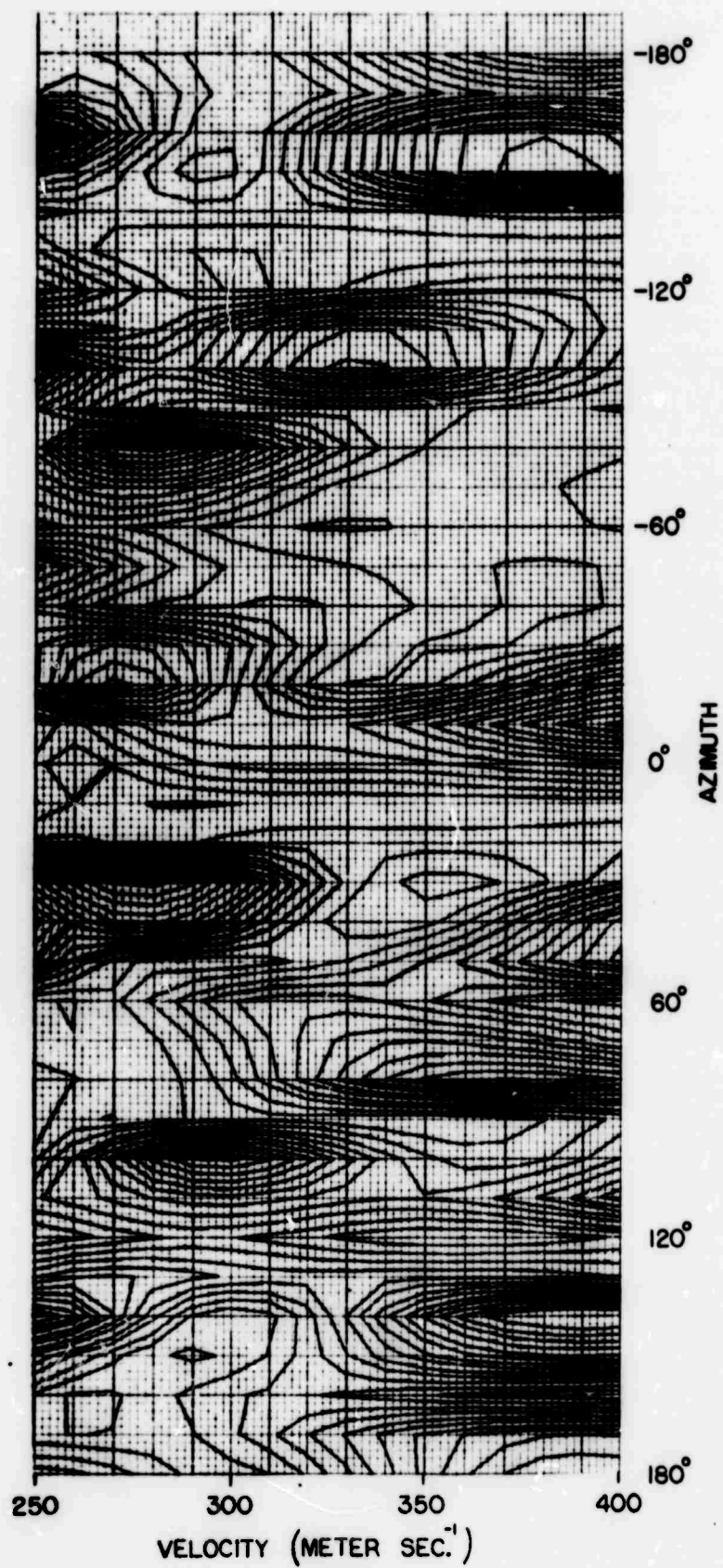
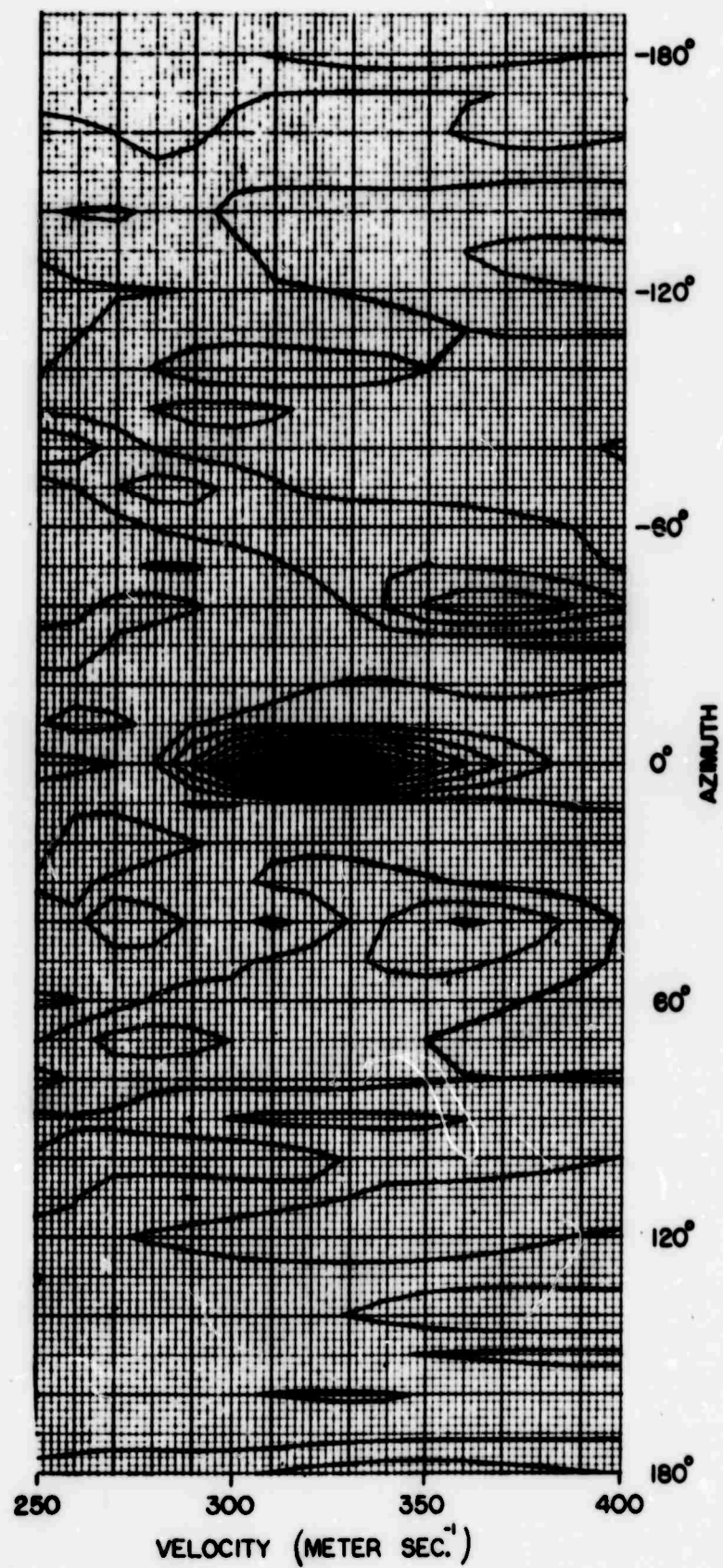


FIG. 4.9 Cophase of the 4.8 min. component of mixed synthetic signal and noise.





**FIG. 4.10** Cophase of the 2.4 - 8.0 min. band of mixed synthetic signal and noise.

NOT REPRODUCIBLE



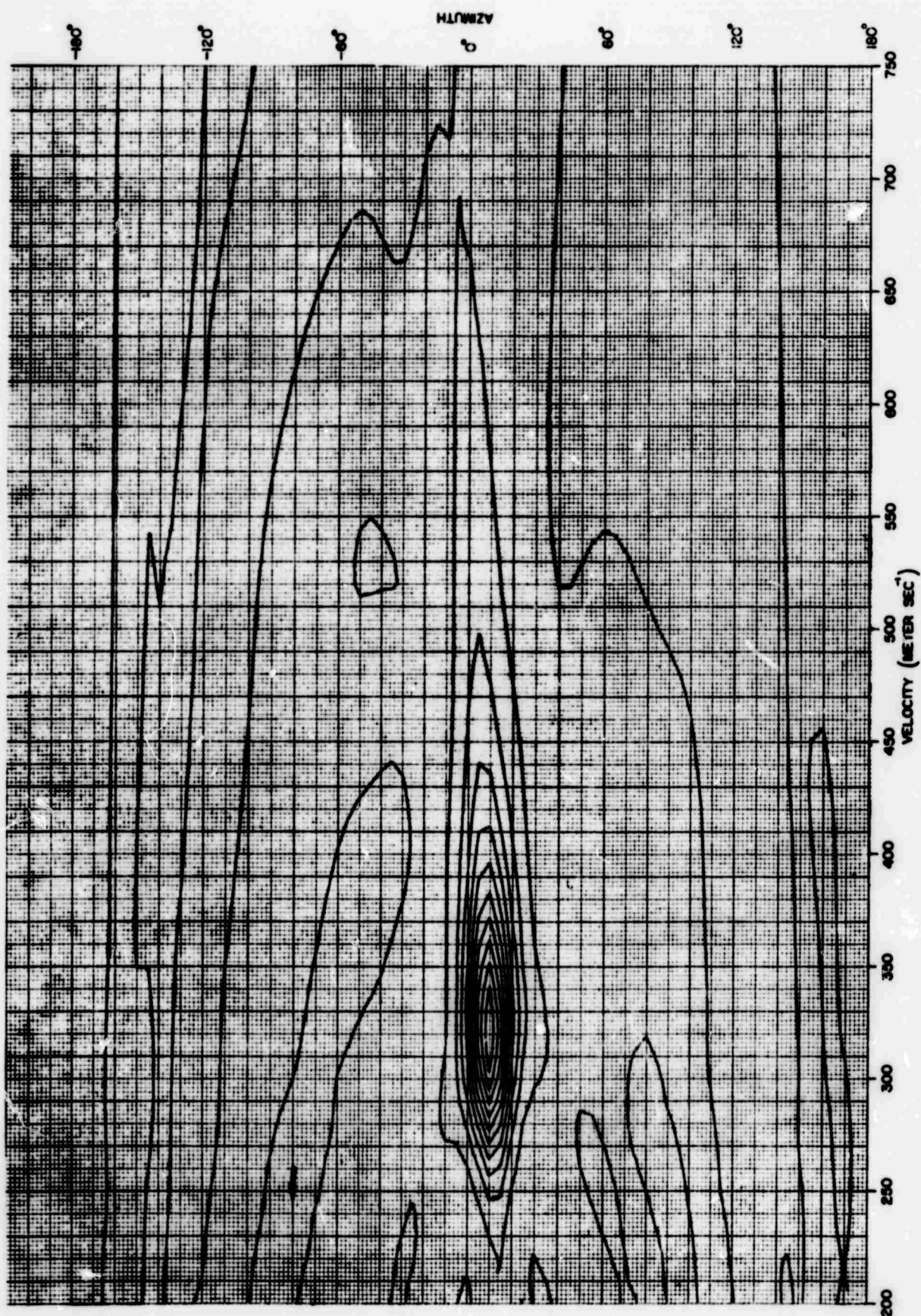


FIGURE 4.11 Cophase of the 2.4 - 8.0 min. band of a  $320 \text{ m. sec}^{-1}$  synthetic signal "detected" by the Taledyne Isotopes array.

NOT REPRODUCIBLE



## Teledyne Isotopes

defined peak of cophase 0.998 at  $N, \theta = (320, 0^\circ)$ . There are no side lobes exceeding 0.10 cophase in the range of velocities from 200 - 800 mps.

The second of this last pair of numerical experiments began with the synthesis of signals similar to those used above, but with a mean phase velocity of 640 mps at a period of 12 minutes. The analysis of the resulting two-hour record, based on frequencies from  $N = 8$  (15-minute period) to  $N = 12$  (10-minute period), is shown in Figure 4.12. Because the wavelengths are larger than the entire array, and only six frequencies are used in the summation, the 1.00 peak, which corresponds to the signal, affords poor velocity resolution, but the half-power points are at less than  $\pm 10^\circ$  of azimuth from the main peak. The relatively poor velocity resolution is an intrinsic property of the array at these large wavelengths.

### 4.2.5 Conclusions

The cophase method is a fast method of detecting signals of down to one-half the noise amplitude, and of estimating the velocity and direction. The most important limitations are the intrinsic limitations of the array size and pattern, and of the signal duration and bandwidth, but not of this statistical procedure, per se.

The method is presently used routinely in the analysis of Teledyne Isotopes microbarograph and doppler array data. Several interesting preliminary results not obtainable by older, simpler, more intuitive techniques, have already been arrived at by the use of the cophase method. These will appear in future project reports.



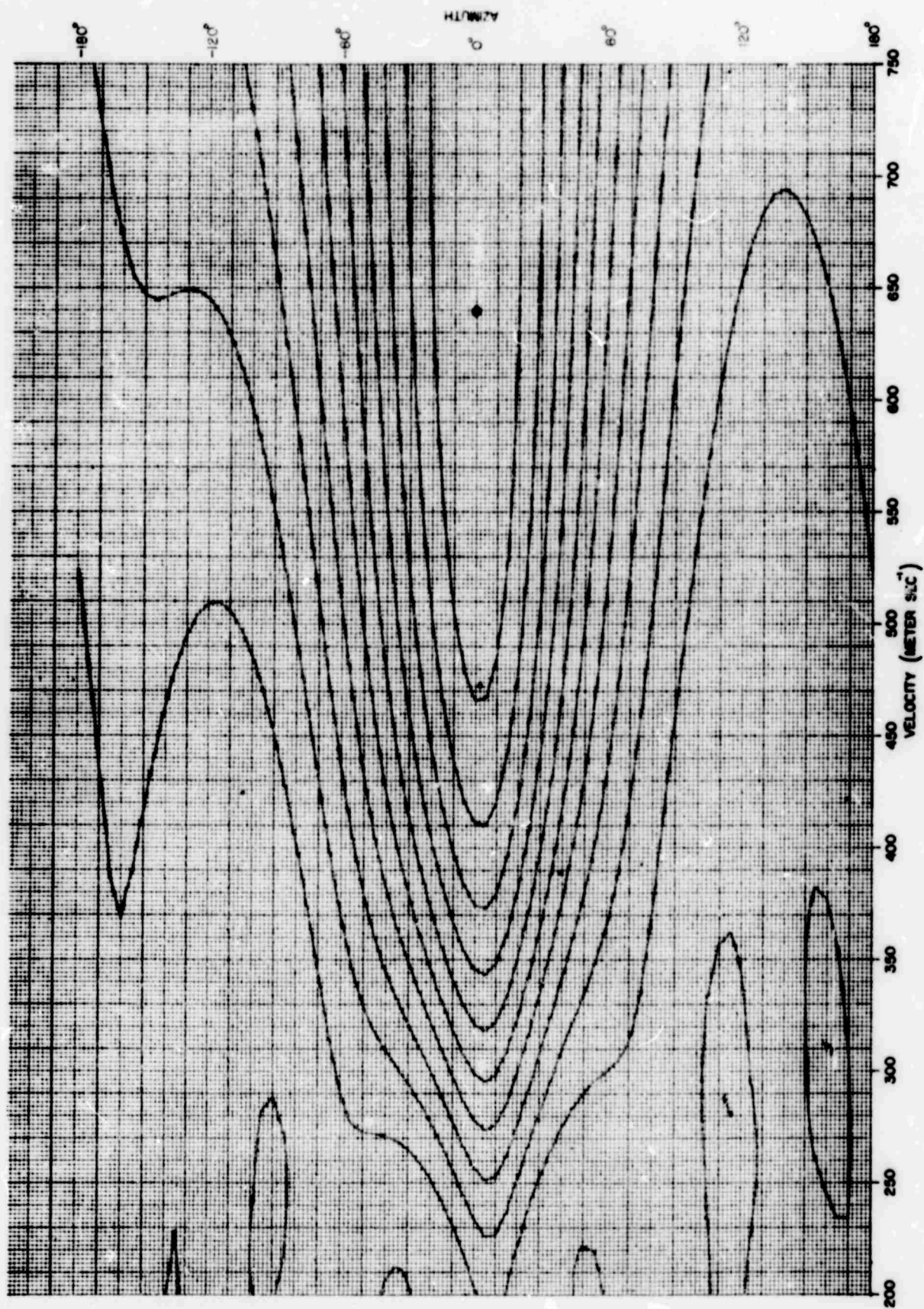


FIG. 4.12 Cophase of the 10 - 15 min. band of a  $640 \text{ m. sec}^{-1}$  synthetic signal "detected" by the Teledyne Isotopes array.

NOT REPRODUCIBLE



## 5. SUMMARY AND CONCLUSIONS

The accomplishments of the research effort during the period 1 September 1968 to 30 September 1969 can be summarized as follows.

1. A program to adjust and recalibrate all the microbarographs and obtain their phase response and coherence with respect to a "standard" instrument was carried out when the system became operational.
2. Three new phase-path sounder systems were built, which added to the one in existence made it possible to set up a 4-element array which, although rudimentary, would permit phase velocity and direction estimates of ionospheric disturbances to be obtained. The sounding frequency used in this doppler array was 4.824 MHz; the average reflection heights corresponding to this frequency are about 170 km during daytime and 200 km during nighttime. The doppler instruments were built after Davies (1962) with some modifications introduced to meet our specifications and mode of operation. Since automatic digitizing equipment was already available at four stations of the microbarograph array, (Catskill, Thornhurst, Lebanon and Westwood), it was decided to locate the doppler receivers at these stations and the transmitter at Sterling Forest, N.Y. This configuration gave an average separation between ionospheric reflection points of about 80 kilometers. The data from the doppler array were fed into spare channels of the data acquisition system and recorded together with the geomagnetic and pressure data on incremental digital magnetic tape.



## Teledyne Isotopes

3. Numerous calculations were undertaken to compare the theoretical response of the Teledyne Isotopes' microbarograph array with those of a number of other arrays; a 10-element isometric array, a 15-element isometric array, a 21-element isometric array and the LAMA array. These calculations showed that for wavelengths between 60 and 300 kilometers the response of the Teledyne Isotopes' array (10 elements) is very similar to that of the LAMA array (20 elements) and that of a 21-element isometric array. It therefore follows that not much improvement in array response could be expected by adding new instruments or changing the spatial arrangement of the present array.
4. Atmospheric disturbances generated by the Chinese thermonuclear explosion of 29 September 1969 were detected by the microbarograph array. These effects showed up in two frequency ranges corresponding to periods of 2-5 minutes and 12-18 minutes respectively. In the shorter period range the arrival corresponding to the short great-circle path was recorded, while in the longer period range the arrival corresponding to the long great-circle path was recorded. The group velocities of these arrivals were of the order of  $300 \text{ m sec}^{-1}$  and  $550 \text{ m sec}^{-1}$  respectively. Some conclusions can be drawn from the comparison of these observations and those of Tolstoy (1967, 1968).
  - a) short period waves. These waves arrive with group velocities of the order of  $300 \text{ m sec}^{-1}$ . The center frequency of the events compared takes different values in each case ranging from 0.002 Hz (8 minutes) to 0.0067 Hz (2.5 minutes); that is, the bandwidth of



## Teledyne Isotopes

these arrivals is of the order of 0.00167 Hz - 0.0167 Hz (2 minutes - 10 minutes). The average phase velocities are  $300 \pm 10 \text{ m sec}^{-1}$  and the wavelengths range from 36 km to 180 km. The arrival corresponding to the long great-circle path cannot in general be recognized.

- b) long period waves. The group velocities of these waves are of the order of  $550 \text{ m sec}^{-1}$  and the phase velocities of the order of  $570 \pm 30 \text{ m sec}^{-1}$ . The center frequencies also vary from event to event as in the short period case. For the events compared the center frequencies were: 3.64 CPH (16.5 minutes), 4.62 CPH (13 minutes), and 4.0 CPH (15 minutes) respectively, that is, the bandwidth extends from 0.000925 Hz to 0.00138 Hz (18 minutes - 12 minutes). In general, both the short and the long great-circle path arrivals can be identified, however, the short great-circle path arrival corresponding to the 29 September 1969 explosion could not be extracted from the background while the long path arrival was identified with very little filtering.
- c) It is probable that results in a) and b) above are an indication of the effects of the seasonal variation of the neutral-temperature structure on the propagation of these waves since the events compared took place in different seasons, i.e., during late spring, mid-summer and fall.



5. Analyses of the phase-path doppler records corresponding to the French test of 24 August 1968 showed that at the time at which the  $600 \text{ m sec}^{-1}$  pressure signal was identified, there was a group of doppler oscillations with an amplitude of 1 Hz and periods of 10 - 15 minutes. The signal-to-noise ratio was 3:1. Since only one doppler sounder was in operation at that time, no information could be obtained concerning the speed and direction of travel of this signal. This finding was a very important factor in redirecting the emphasis of the project towards ionospheric studies. Unfortunately, during the time corresponding to the arrival of infrasonic signals in the September 1969 test a magnetic storm was in progress and the doppler background level was very high. It is possible that the doppler signals have been masked by the large phase-path fluctuations induced by the storm.
6. Observations of phase-path variations during the Saturn-Apollo IX launch suggest that some acoustic energy in the period range 0.5 - 5.0 minutes, generated by the rocket engine, is channeled at ionospheric levels as evidenced by the phase-path doppler records. Analyses of microbarograph records for this event did not show any signal in this period range.
7. A preliminary study of ionospheric background motions was carried out using doppler and magnetometer records. Power and cross spectral analyses of these records indicated that the background activity could be broadly separated into two period ranges: periods longer and shorter than 5 minutes. The shorter periods correlate often with magnetic micropulsations. The analyses of these events showed high coherence



between the NS magnetic component and the phase-path variations, suggesting that the ionospheric motions producing the phase-path changes are due to the modulation of the ionospheric plasma by transverse hydromagnetic waves. Analyses of microbarograph records corresponding to these time intervals of high correlation did not show any unusual infrasonic activity. In the longer period range the power spectra of phase-path sounder records obtained simultaneously at three sounding frequencies (corresponding to three ionospheric heights) showed systematic peaks and slope breaks which appear to shift towards longer periods for greater reflection heights (higher sounding frequencies). The frequencies corresponding to these spectral peaks had values of the same order of the local value of the Väisälä frequency for an adiabatic atmosphere. These findings lead to the conclusion that a large portion of the ionospheric motion background for periods shorter than 5 minutes has a hydromagnetic origin while periods longer than 5 minutes are probably due to internal gravity wave activity.

8. Investigation of the spatial coherency of the signal and noise fields for the array of microbarographs was carried out using the signals of the French test of 24 August 1968 (2-5 minute period range) and comparable data samples of background. The results indicated that:
  - a) Acoustic signals have coherencies well above the background noise at separations greater than 3 or 4 kilometers.
  - b) The signal coherence remains high out to separations of 50 kilometers.
  - c) Transverse signal coherencies are higher than parallel signal coherencies, that is, the waves are long-crested.



9. A theoretical study of the interaction of instability waves in the atmosphere (due to existence of wind shear) and internal gravity waves (due to atmospheric stratification) was carried out by Dr. C.E. Grosch. The model, which neglects compressibility, consists of a duct bounded by rigid planes, the Väisälä frequency is assumed to be constant, and the shear flow has a parabolic profile,  $(\bar{u}_{00} = 1 - y^2)$ . The major results are that this stratified shear flow supports both internal gravity and instability waves; that the internal gravity waves are, roughly, trapped within the layer where  $\bar{u}_{00} > c$ ; and that the phase velocity of the internal gravity modes is approximately equal to the maximum velocity of the shear flow.
10. In the theoretical aspect of signal processing two methods have been developed.
  - a) The first one deals with the estimation and detection of an unknown dispersive signal using a two-dimensional array and represents the effort by a member of our group (Dr. M. Hinich), to find a simple method for estimating the phase velocity and direction of a plane wave signal, buried in noise, propagating across a two-dimensional array. The method uses a linear regression on sensor position, of the Fourier phases of the sensor outputs, in order to produce estimates of the wave number. By appropriate smoothing over frequency, estimates of the direction and phase velocity are obtained. The precision of the estimates depends on the signal-to-noise ratio, the square root of the number of sensors, and the number of wavelengths which fall in the array.



- b) The second method represents the effort of another member of the group (Dr. E. Posmentier) and consists of an ad hoc array processor that characterizes signal strength as a function of phase velocity and direction. This statistical procedure which is called Cophase Analysis throughout this work, basically calculates the normalized, weighted sum over all  $1/2 K (K-1)$  detector pairs, and over all frequencies, of the cosines of the difference between the Fourier phase differences and the assumed phase differences. Several tests of this program with synthetic and real data have shown that the cophase method is a fast method of detecting signals of down to one-half the noise amplitude, and of estimating the velocity and direction. The most important limitations are the intrinsic limitations of the array size and pattern, and of the signal duration and bandwidth, but not of this statistical procedure per se.

To conclude, the authors wish to recommend that, since the acoustic energy generated by nuclear explosions in the atmosphere is distributed with height according to various propagating modes, observations with both microbarograph and phase-path sounders be continued and that an effort be made to expand the existing phase-path sounder array to operate at two sounding frequencies.



REFERENCES

- |                                     |      |   |
|-------------------------------------|------|---|
| Alfvén, H. and Falthammar, C.G.     | 1963 | Cosmical Electrodynamics, Oxford at the Clarendon Press                       |
| Berman, A. and Clay, C.S.           | 1957 | J. Acoust. Soc. Am. <u>29</u> , 805   |
| Blackman, R.B. and Tukey, J.W.      | 1959 | The Measurements of Power Spectra, Dover Publications (N.Y.)                  |
| Bolgiano, R.                        | 1959 | J. Geophys. Res. <u>64</u> , 2037   |
| Born, M. and Wolf, E.               | 1965 | Principles of Optics, Pergamon Press, (N.Y.)                                  |
| Boyd, G.M. and Duffus, H.J.         | 1969 | Can. J. Phys. <u>47</u> , 1585  |
| Brownlee, K.A.                      | 1965 | Statistical Theory and Methodology in Science & Engineering, John Wiley, N.Y. |
| Bryn, F.                            | 1962 | J. Acoust. Soc. Am. <u>34</u> , 289   |
| Burg, J.                            | 1964 | Geophysics, <u>29</u> , 693   |
| Capon, J., et al.                   | 1967 | Proc. IEEE <u>55</u> , 192  |
| Chan, K.L. et al.                   | 1962 | J. Geophys. Res. <u>67</u> , 2066   |
| Christoffel, D.A. and Linford, J.G. | 1966 | J. Geophys. Res. <u>71</u> , 891  |
| Clay, C.S. and Kraft, D.W.          | 1967 | Hudson Laboratories of Columbia Univ. Tech Report #135                        |
| Cooley, J. et al.                   | 1967 | IEEE Trans. Audio ElectroAcoust. <u>15</u> , #2, 79                           |
| Courant, R., Hilbert, D.            | 1953 | Methods of Mathematical Physics, Vol II, Interscience, N.Y.                   |
| Davies, K.                          | 1962 | Proc. IRE <u>50</u> , 94 and correction 1544                                  |
| Davies, K. and Baker, D.M.          | 1965 | J. Geophys. Res. <u>70</u> , 2251   |
| Davies, K.                          | 1969 | Ionospheric Radio Waves, Blaisdell Publishing Co., Waltham, Mass.             |
| Deutsch, R.                         | 1965 | Estimation Theory, Prentice-Hall, N.J.  |
| Dieminger, W. and Kohl, H.          | 1962 | Nature <u>193</u> , 963   |



# Teledyne Isotopes

Dolph, C.L. and Lewis, D.C.	1958	Quart. Appl. Math. <u>16</u> , 97
Donn, W.L. and Shaw, D.M.	1967	Rev. Geophys. <u>5</u> , 53
Drazin, P.G. and Howard, L.N.	1966	Advan. Appl. Mech. <u>9</u> , 1
Dungey, J.W.	1955	J. Atmosph. Terrest. Phys. <u>8</u> , 39
Dungey, J.W.	1967	Physics of Geomagnetic Phenomena, Academic Press, N.Y., London
Eckhaus, W.	1965	Studies in Non-Linear Stability Theory, Springer, Berlin
Faran, J.J., Jr. and Hills, R., Jr.	1952	Acoustics Res. Lab., Harvard Univ. Tech Memo #28
Georges, T.M.	1967	J. Geophys. Res. <u>72</u> , 422
Good, I.J.	1963	Time Series Analysis, John Wiley, N.Y.
Goodman, N.R.	1957	Ph.D. Thesis, Princeton Univ.
Graybill, I.F.	1961	An Introduction to Linear Statistical Models, Vol I, McGraw-Hill, N.Y.
Greenhow, J.S. and Neufeld, E.L.	1959	J. Geophys. Res. <u>64</u> , 2129
Haubrich, R.A.	1968	Bull. Seis. Soc. Amer., <u>58</u> , 977
Herron, T.J., et al.	1969	J. Geophys. Res. <u>74</u> , 1321
Herron, T.J. and Tolstoy, I.	1969	J. Atmos. Sci. <u>26</u> , 266
Herron, T.J. and Montes, H.A.	1970	J. Atmos. Sci. <u>27</u> , 51
Hines, C.O.	1960	Can. J. Phys. <u>38</u> , 1441
Hines, C.O.	1964	Research in Geophysics I, 299, MIT Press
Hinich, M.J. and Clay, C.S.	1968	Review of Geophysics, <u>6</u> , 347
Jacobs, J.A., et al.	1965	Nature, <u>205</u> , 61
Jacobs, J.A. and Watanabe, T.	1966	Radio Sci. <u>1</u> , 357
Klostermeyer, J.	1969	J. Atmosph. Terr. Phys. <u>31</u> , 25
Koppel, E.	1964	J. Mathematical Physics <u>7</u> , 963
Laster, S.J. and Linville, A.F.	1966	J. Geophys. Res. <u>71</u> , 1669



## Teledyne Isotopes

Levin, M.J.	1965	Radio Electron. Eng. <u>April</u> , 213
Liller, W. and Whipple, F.L.	1954	Spec. Supp. J. Atmos. Terr. Phys. I, 112
Lin, C.C.	1955	The Theory of Hydrodynamic Stability, Cambridge Univ. Press
Martyn, D.F.	1950	Proc. Roy. Soc. <u>A201</u> , 216
Martyn, D.F.	1955	The Physics of the Ionosphere, 163, The Physical Society, London
Munro, G.H.	1950	Proc. Roy. Soc. <u>202</u> , 208
Munro, G.H.	1958	Aust. J. Phys. <u>11</u> , 91
Rishbeth, H. and Garriot, O.K.	1964	Radio Science J. Res. NBS <u>68D</u> , 339
Rostoker, G.	1967	Can. J. Phys. <u>45</u> , 1319
Row, R.V.	1967	J. Geophys. Res. <u>72</u> , 1599
Saito, T. and Matsushita, S.	1968	J. Geophys. Res. <u>73</u> , 267
Smith, M.K.	1956	Geophysics, <u>21</u> , 337
Thome, G.D. and Rao, P.B.	1969	Raytheon Final Report for ARPA, May
Titheridge, J.E.	1967	Radio Science, <u>2</u> , 1165
Titheridge, J.E.	1968	J. Geophys. Res. <u>73</u> , 343
Tolstoy, I.	1963	Rev. Mod. Phys. <u>35</u> , 207
Tolstoy, I.	1967	J. Geophys. Res. <u>72</u> , 4605
Tolstoy, I. and Herron, T.J.	1968	Hudson Laboratories of Columbia Univ. Tech Reports 139 and 163
Tolstoy, I. and Herron, T.J.	1970	J. Atmos. Sci. <u>27</u> , 55
Wickersham, A.F., Jr.	1965	J. Geophys. Res. <u>70</u> , 4875



UNCLASSIFIED

Security Classification

## DOCUMENT CONTROL DATA - R &amp; D

(Security classification of title, body of abstract and indexing annotation must be entered when the overall report is classified)

## 1. ORIGINATING ACTIVITY (Corporate name)

TELEDYNE ISOTOPES  
50 Van Buren Avenue  
Westwood, New Jersey 07675

## 2a. REPORT SECURITY CLASSIFICATION

UNCLASSIFIED

## 2b. GROUP

## 3. REPORT TITLE

SUMMARY REPORT - ATMOSPHERIC PROPAGATION STUDIES UP TO 30 SEPTEMBER 1969

## 4. DESCRIPTIVE NOTES (Type of report and inclusive dates)

Scientific..... Interim

## 5. AUTHOR(S) (First name, middle initial, last name)

Hernan A. Montes  
Chester E. Grosch

Melvin J. Hinich  
Eric S. Posmentier

## 6. REPORT DATE

July 1970

## 7a. TOTAL NO. OF PAGES

175

## 7b. NO. OF REFS

64

## 8a. CONTRACT OR GRANT NO.

F 44620-69-C-0038

## 8b. PROJECT NO.

9544

## c.

62701D

## d.

## 9a. ORIGINATOR'S REPORT NUMBER(S)

IWL-7556-175

## 9b. OTHER REPORT NO(S) (Any other numbers that may be assigned this report)

AFOSR 70-2734TR

## 10. DISTRIBUTION STATEMENT

1. This document has been approved for public release and sale; its distribution is unlimited.

## 11. SUPPLEMENTARY NOTES

TECH, OTHER

## 12. SPONSORING/MONITORING AGENCY NAME(S) AND ADDRESS(ES)

AF Office of Scientific Research (NFG)  
1400 Wilson Boulevard  
Arlington, VA 22209

## 13. ABSTRACT

A summary is given of significant results obtained during the research effort corresponding to the period 1 September 1968 - 30 September 1969. Particular emphasis was given to the construction of a phase-path doppler sounder array. Signals detected by the microbarograph array on the occasion of the Chinese nuclear test of 29 September 1969 are compared with signals from previous tests. There appears to be a seasonal effect on the propagation and/or bandwidth of these signals. Preliminary work on ionospheric motion background using phase-path sounder data indicates that the background activity can be broadly separated into two period ranges: periods longer and shorter than 5 minutes. The shorter periods appear to have a hydromagnetic origin while the longer periods are probably due to internal gravity wave activity. A study of the spatial coherency of the signal and noise field for the array of microbarographs indicated that acoustic signals have coherencies well above the background noise at separations greater than 3 or 4 km. The signal coherency remains high up to separations of 50 km and transverse signal coherencies are larger than parallel signal coherencies as would be expected from long-crested waves. A theoretical investigation of the interaction between instability waves and internal gravity waves in the atmosphere showed that internal gravity waves are trapped within a layer where the shear flow velocity is greater than the speed of sound and that the phase velocity of the internal gravity waves is approximately equal to the maximum velocity of the shear flow. As part of the theoretical aspect of signal processing two array processing techniques have been developed.